REPORT DOCUMENTATION PAGE

Form Approved OMB No. 0704-0188

Public reporting burden for this collection of information is estimated to average 1 hour per response, including the time for reviewing instructions, searching existing data sources, gathering and maintaining the data needed, and completing and reviewing the collection of information. Send comments regarding this burden estimate or any other aspect of this collection of information, including suggestions for reducing the burden, to Department of Defense, Washington Headquarters Services, Directorate for Information Operations and Reports (0704-0188), 1215 Jefferson Davis Highway, Suite 1204, Arlington, VA 22202-4302. Respondents should be aware that notwithstanding any other provision of law, no person shall be subject to any penalty for failing to comply with a collection of information if it does not display a currently valid OMB control number.
PLEASE DO NOT RETURN YOUR FORM TO THE ABOVE ADDRESS.

1. REPORT DATE (DD-MM-YYYY)	2. REPORT TYPE	3. DATES COVERED (From – To)
24-06-2004	Final Report	1 October 2003 - 6 March 04

4. TITLE AND SUBTITLE

Research of Morphing Wing Efficiency

5a. CONTRACT NUMBER
FA8655-03-D-0001, Delivery Order 0010

5b. GRANT NUMBER

5c. PROGRAM ELEMENT NUMBER

6. AUTHOR(S)

Dr. Valery Komarov

5d. PROJECT NUMBER

5d. TASK NUMBER

5e. WORK UNIT NUMBER

7. PERFORMING ORGANIZATION NAME(S) AND ADDRESS(ES)
Samara State Aerospace University (SSAU)
Institute AVICON of SSAU, 10 Build., 34, Moskovskoe Shosse
Samara 443086
Russia

8. PERFORMING ORGANIZATION REPORT NUMBER

N/A

9. SPONSORING/MONITORING AGENCY NAME(S) AND ADDRESS(ES)

EOARD
PSC 802 BOX 14
FPO 09499-0014

10. SPONSOR/MONITOR'S ACRONYM(S)

11. SPONSOR/MONITOR'S REPORT NUMBER(S)
EOARD Task 03-9003

12. DISTRIBUTION/AVAILABILITY STATEMENT

Approved for public release; distribution is unlimited. (approval given by local Public Affairs Office)

13. SUPPLEMENTARY NOTES

14. ABSTRACT

This report results from a contract tasking Samara State Aerospace University (SSAU) as follows: The contractor will develop and investigate aerodynamic and structural weight theories associated with morphing wing technology. The contractor has proposed using a generic, telescoping wing design as the baseline configuration for analysis. Specific tasks to be accomplished include: 1. Development of a new weight analysis theory; 2. Creation of an analytical model of the telescoping wing design; 3. Calculation of Load-Carrying Factor for the uniform pressure distribution or for some prescribed spanwise circulation distribution; 4. Calculation of a new 'dimensionless Load-Carrying Factor', according to a special algorithm which will allow computing absolute weight and wing weight fracture for different specific wing loadings; 4. Calculation of a 'Construction Factor' from retrospective analysis of similar wings; 5. Wind tunnel tests of a model of the telescoping wing to assess impact on aerodynamic coefficients and drag polars; 6. Creation of the vortex-lattice computational model of the telescoping wing to obtain its aerodynamic coefficients; 7. Creation of the panel method computational model for detailed study of flow features in the region of the telescope wing joint; and 8. Analysis and comparison of experimental and computational results.

15. SUBJECT TERMS
EOARD, Aerodynamics, Morphing, Aeroelasticity

16. SECURITY CLASSIFICATION OF:			17. LIMITATION OF ABSTRACT	18. NUMBER OF PAGES	19a. NAME OF RESPONSIBLE PERSON WAYNE A. DONALDSON
a. REPORT UNCLAS	b. ABSTRACT UNCLAS	c. THIS PAGE UNCLAS	UL	113	19b. TELEPHONE NUMBER (Include area code) +44 (0)20 7514 4299

Standard Form 298 (Rev. 8/98)
Prescribed by ANSI Std. Z39-18

Samara State Aerospace University

Avikon Institute

Final Technical Report

RESEARCH OF MORPHING WING EFFICIENCY

Samara

June 2004

Contents

1 Nomenclature

$A = \dfrac{b^2}{S}$ - aspect ratio of the wing;

$b/2$ - semispan of the wing;

$\bar{c}_i$ - mean chord of the i-th part of the wing;

$\bar{c}_t = \dfrac{c_t}{c_1}$ - dimensionless chord of rectangular outer wing part (referenced to the tip chord of the main part of the wing);

$c_{\sec}$ - section chord;

c_A - mean aerodynamic chord;

c_m - mean chord;

c_t - tip chord;

c_r - root chord;

$\boldsymbol{l} = \dfrac{c_1}{c}$ - taper ratio of the main part of the wing (referenced to the root chord);

$C_{L_{\boldsymbol{a}}}$ - slope of the lift curve;

K - drag due to lift factor;

Λ_{le} - leading-edge sweepback angle, deg.;

C_{D_0} - zero lift drag coefficient;

C_f - flat-plate skin friction coefficient;

$C_{m_{\boldsymbol{a}}}$ - derivative of a pitching-moment coefficient;

L/D_{MAX} - maximum aerodynamic efficiency;

$\bar{\Gamma}(\bar{z}) = \dfrac{\Gamma(\bar{z})}{\Gamma}$ - dimensionless velocity circulation;

$\Gamma = 2\displaystyle\int_0^{b/2} \Gamma(z)\,dz$ - net velocity circulation;

z - spanwise coordinate;

$\bar{z} = \dfrac{z}{b/2}$ - dimensionless spanwise coordinate;

t - thickness of wing;

$\bar{t} = \dfrac{t}{c}$	-	dimensionless airfoil thickness;
S	-	reference wing area, sum of the outer (extendable) part area and main part area.
V	-	airspeed; volume of structure material;
M	-	Mach number;
$\mathrm{Re}_i = \dfrac{V\bar{c}_i}{n}$	-	Reynolds number based on the mean chord of each part of the wing;
H	-	flight altitude;
n	-	coefficient of kinematic viscosity, m^2/s;
m_z^a	-	derivative in angle atack of pitching moment coefficient;
$\bar{x}_F$	-	relative mean aerodynamic center of wing.
s	-	stress;
N	-	internal force;
l	-	length;
R	-	equivalent force flow;
m	-	total number of vortexes on the wing;
n	-	element quantity;
N	-	number of strips on a semispan of the wing;
C_p	-	dimensionless pressure coefficient.
r	-	density of structural material;
P	-	characteristic (reference) load;
L	-	characteristic (reference) dimension (length);
m_o	-	take-off mass;
m_{st}	-	mass of structure;
m_{wing}	-	mass of wing structure;

New criteria and notations used on this report:

G	-	Load-Carrying Factor (LCF);
C_K	-	dimensionless coefficient of structure load-carrying perfection;
j	-	dimensionless full mass coefficient;

Abbreviatures:

FEM	-	Finite Element Method;
LCF	-	Load-Carrying Factor;
TW	-	Telescope Wing;
MW	-	Morphing Wing;
MDV	-	Method of Descrete Vortexes;

Indices:

i	-	element number;
eqv	-	equivalent;
st	-	structure;
T	-	theoretical;

2 Summary

The present report contains a description of the research results about weight and aerodynamic efficiency of telescope wings.

Telescope wings (TW) are sufficiently novel. There are no available statistical data for such wings. Besides the efficiency of TW should obviously depend upon a number of design variables: ratios of areas and lengths, arrangement of stationary and movable parts and etc. Known weight formulas are not able to account for these features.

That is why in the present work a vital new approach for calculation of unconventional aircraft structures is proposed. The main idea of this approach, when applied to TW, is the following.

1. Into the geometrical limits of the TW, including internal hollows, a three-dimensional elastic body is inscribed. This body consists of some hypothetical material with non-uniform density. We consider that local strength of this material and its local coefficient of elasticity depend linearly upon its local density.

2. Optimization for the density distribution in this material is performed according to a special algorithm. The objective function for this optimization if the load-carrying factor (LCF) G, which expresses both the internal loads within the structure and their action path lengths. In case of 3-D body it is calculated as

$$G = \int_V \boldsymbol{s}^{\,eqv} dV$$

The result of this optimization is a body with non-uniform density distribution (a structure), which has a minimal value of G for the given external loading, geometrical limits and the type of joint between stationary and movable parts of the TW. (This process is similar to biological optimization of animal bones, which have non-uniform density distribution; it is straightforward that the bones of birds have the highest weight perfection).

3. A new dimensionless parameter is introduced – load-carrying factor coefficient. It is determined as a ratio of LCF to the product of characteristic length and characteristic load of the structure. For things characteristic length corresponds to square root of area and characteristic load corresponds to lift. This new criteria allows for comparison of weight efficiency of different structures, and also allows to

calculate absolute and fraction mass of the structure for different geometry and loading. All the necessary equations are obtained.

Aerodynamic research play a significant role in the present work. They provide solution to two problems:

1. Identification of span load distribution for TW
2. Estimation of maximum lift-to-drag ratio.

Because the object of study is unconventional, three different numerical methods were used for aerodynamic research in order to increase assurance of the results:

1. Linear bound vortex method (steady inviscid incompressible flow)
2. Non-linear vortex lattice method (nonsteady inviscid incompressible flow)
3. Finite volume method (steady viscious incompressible flow).

Besides three different mockups were designed, built and tested in the wind tunnel. In order to provide validation and better understanding of the results all weight and aerodynamic research for TW were accompanied by the same kind of research for geometrically equivalent trapezoidal wings.

Academic versions of MSC NASTRAN (license was paid from financing of the present project RE0-1386) and STAR-CD (license was already available at aerohydrodynamics department) software were used during the research, together with the software developed in Samara State Aerospace University (SSAU).

The main results of the work are:

1. It was ascertained that telescope wings can have weight and aerodynamic efficiency nearly equal to equivalent trapezoidal wings of the same span (figures 9.18, 9.19 and tables 9.1, 9.2). With optimized geometry telescope wings can have even better performance than equivalent trapezoidal wings.

2. The fundamentals of a new efficient approach to weight analysis were developed for the purpose of solving the stated problem. This approach is based on 3D-modeling and can be highly useful for conceptual design of aircraft of unconventional shapes.

3. Project management and financing through CRDF allowed to acquire all the necessary hardware and software and to bring together an efficient team of experts capable to solve complex interdisciplinary problems.

The present report is arranged in such a way that each part of it can be read separatly. That is why some of the results appear several times in different parts.

3 Introduction

Morphing wing can provide sufficient improvement of weight and aerodynamic performance of aircraft and can fulfill various additional requirements, i.e. they can be adaptive. For example, they can be folding thus having variable specific wing load.

Morphing wing can has different applications at future-technology flighing vehicles. One can find many papers devoted to their study [21, 22].

Usually morphing wing is an unconventional structure. One of the most important problems in the design of aircraft using morphing wing is sufficiently accurate estimation of morphing wing weight parameters at early stages of the design.

Different methods of weight design [1, 3, 4, 5, 12, 17, 18, 19, 20] based on statistical data and simplified physical principles of structure operation give too wide spreading of the results even for conventional structures, as we will show later. Such approaches are not able to account for some principal features of morphing wing – change of the area of lifting surface, type of the joint between moving parts and etc. That is why weight design of morphing wing requires development of new approaches.

In the present work these approaches are developed in a quiet general form and their application for telescope wing, which is a particular case of the morphing wing, is demonstrated.

In aviation the structural mass m_{st} and especially the structural mass fraction which is m_{st} to m_o (aircraft takeoff mass) ratio

$$\bar{m}_{st} = \frac{m_{st}}{m_o} \tag{3.1}$$

determines aircraft's transport efficiency and even the possibility of designing the aircraft with desirable performance. It can be easily seen from existence equation [1, 3] which is used for takeoff mass estimation at early stages of the design. It is given below with simplified set of masses as an illustration only:

$$m_o = \frac{m_{pl}}{1 - \bar{m}_{st} - \bar{m}_{sys} - \bar{m}_f - \bar{m}_{pp}}, \tag{3.2}$$

where m_{pl} – payload mass (for example passengers and baggage);

$\overline{m}_{st}$ and $\overline{m}_{sys}$ – structural mass fraction and system mass faction, which can be estimated on statistical basis;

$\overline{m}_f$ and $\overline{m}_{pp}$ – fuel mass fraction and propulsion mass fraction, which depend mainly upon operational range and speed and can be calculated with quiet a good accuracy.

If the sum of all relative masses in (3.2) is greater than one, then such an aircraft could not exist. From this comes the name of the equation.

For some kinds of aircraft payload mass makes only 10% of takeoff mass and structural mass – 25÷30%. So on the one hand one-percent decrease of structural mass causes several-percent increase of payload mass, and on the other hand a small error in estimation of $\overline{m}_{st}$ yields a great misestimating of the key design parameter m_o.

It should be mentioned that the problem of early stage structural mass estimation is paid much attention in aircraft design theory. Basics of systematical research of aircraft construction strength and weight efficiency are given in a work of F. R. Shanley [19]. Many of so called "weight formulas" for estimation of aircraft absolute and relative masses can be found in [5, 17, 18, 20].

Relative structural mass depends upon many parameters: geometry, accelerations, load distribution, size and location of cutouts, material strength and stiffness characteristics and etc.

To take into account dependence of internal structural loads from geometry and external loads the beam theory is often used as a basis of weight formulas. Such parameters as engine location (at the wing or at the fuselage), gloved wing and etc. are accounted by multiple correction factors usually derived from statistics of available aircraft.

Such approach doesn't guarantee adequate precision of weight calculations in case of unusual scheme, advanced constructions or dramatically increased dimensions of an aircraft if the "square and cube" law [18, 19] is not considered in weight formulas.

Figure 3.1 presents an example of wing mass fracture calculation for two aircraft. One is similar to "Iliushin Il-96MT", and another, transport airplane, has payload of 250 000 kg (project "Ecolifter").
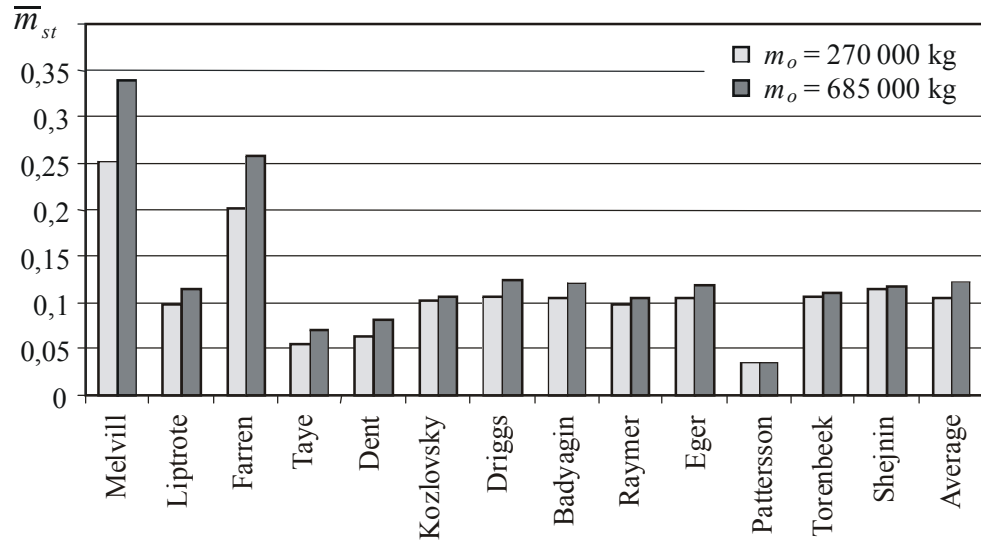
$$\overline{m}_{st}$$

Figure 3.1 – Results of wing mass fracture estimation

Different weight formulas give a significant spread in values. To overcome this shortcoming V.M. Sheinin proposed his method of multiple calculations [18], in which extreme estimations are discarded and intermediate are averaged. This method provides quiet high accuracy but its implementation is limited to conventional structures and requires some skill for usage.

Figure 3.2 presents another example – different load-carrying schemes for delta wings. Known weight formulas do not allow in principle to account all features of these designs.
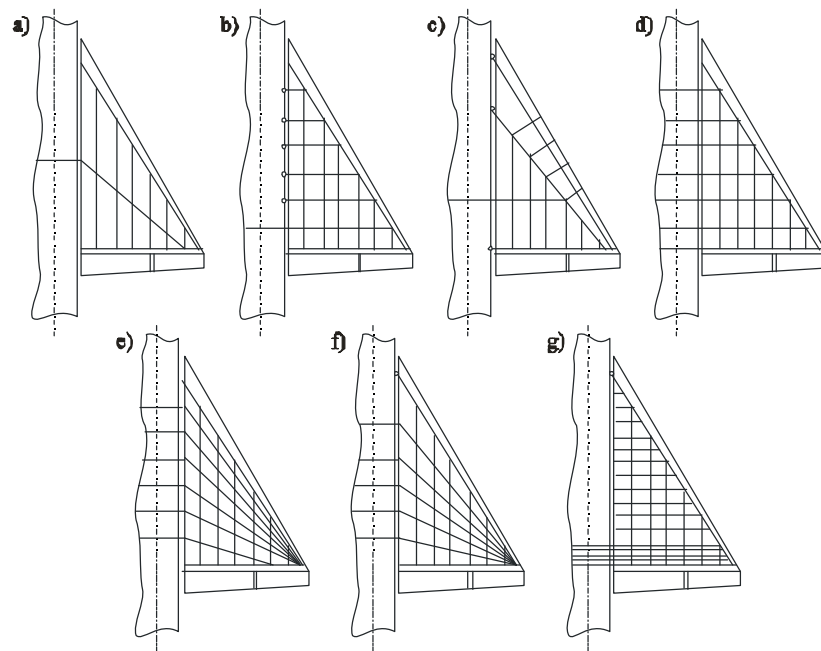
Figure 3.2 – Variants of structural schemes for the delta wings

Thus a new approach is needed in order to increase the accuracy in aircraft structure design.

Advantages in numerical simulation of structures and ubiquitous implementation of finite element method (FEM), together with determination of some integral properties of elastic systems [10, 13] allow create of more general approach for early-stage mass estimation and load-carrying scheme choice.

4 Weight analisys of airframe structures based on a new metric "load-carrying factor"

4.1 Load-carrying factor

Relationship between results of FEM simulation of the structure and its required mass can be expressed through the specific criterion – "load-carrying factor" – G, which accounts both for magnitude and length of action of internal loads in the structure [10, 12, 13, 15].

For frames

$$G = \sum_{i=1}^{n} |N_i| \cdot l_i ,$$
(4.1)

where i – rod number, N_i - force, l_i - length.

For shell structures

$$G = \sum_{i=1}^{n} R_i \cdot S_i ,$$
(4.2)

where i – element number, R_i – equivalent force flow, S_i – element area.

For 3D structures

$$G = \int_V \boldsymbol{s}^{eqv} dV ,$$
(4.3)

where $\boldsymbol{s}^{eqv}$ – equivalent stress, V – structural material volume.

Load-carrying factor has some interesting properties which can be useful for structure weight estimation.

G is determined by load-carrying scheme, i.e. element type, number of elements, types of their joints and arrangement. For statically determinate structures the value of G is independent of stiffness ratio of load-carrying elements, and for statically undeterminate, according to numerical simulations, is weekly dependent. For example, cross-section areas of some elements and their internal loads can change their order of magnitude during optimization, which result only in few percents of changing of G value for the whole structure.

Theoretically required structural material volume V_T for fully-stressed structure with definite load-carrying scheme can be estimated through G and

working stress value after single calculation of internal loads for some rational initial distribution of element stiffness according to simple relationship

$$V_T = \frac{G}{[\boldsymbol{s}]} \qquad (4.4)$$

Really, for fully-stressed frame we have

$$V_T = \sum_{i=1}^{n} \frac{|N_i|}{[\boldsymbol{s}]} \cdot l_i = \sum_{i=1}^{n} F_i \cdot l_i , \qquad (4.5)$$

where F_i – rod cross-section area.

Similar result can be obtained for shell structures using equivalent force flow as a measure of internal loads [13].

G value can be calculated with quiet high accuracy with relatively "coarse" FEM models.

Using V_T, material density $\boldsymbol{r}$ and full mass coefficient $\boldsymbol{j}$, which accounts for mass increase from joints and non-carrying elements, deviations from optimal material distribution in favor of simplicity and fabricability of the structure and etc., one can calculate real (practical) structural mass

$$m_{st} = \boldsymbol{j} \cdot \boldsymbol{r} \cdot V_T = \boldsymbol{j} \cdot \boldsymbol{r} \cdot \frac{G}{[\boldsymbol{s}]} \qquad (4.6)$$

or

$$m_{st} = \boldsymbol{j} \, \frac{G}{\bar{\boldsymbol{s}}} , \qquad (4.7)$$

where $\bar{\boldsymbol{s}}$ – material strength-to-weight ratio, $[\boldsymbol{s}]$ – material allowable strength.

In weight formula (4.7) all of the three multipliers determine nearly independent properties of the structure:

G - geometry, load-carrying scheme and loads;

$\bar{\boldsymbol{s}}$ - material strength;

$\boldsymbol{j}$ - structural and technological perfection.

Relationship (4.7) can be used for derivation of new weight formulas for the whole structure or its parts. In this case $\bar{\boldsymbol{s}}$ will account for material choice, G will account for all features of load-carrying scheme of the future structure, and $\boldsymbol{j}$ coefficient can be defined from analysis of some already built aircraft, taken as a prototype

$$j = \frac{\tilde{m}_{st} \cdot \tilde{\bar{s}}}{\tilde{G}}, \tag{4.8}$$

where sign "~" marks values for the prototype.

If the prototype has high weight perfection and no major changes in engineering solutions (j) and material choice ($\bar{s}$) are expected, for example, during modifications, then for mass estimation of a new structure formula (4.7) can be written with (4.8) especially simple

$$m_{st} = \frac{G}{\tilde{G}} \tilde{m}_{st} \tag{4.9}$$

Nowadays FEM models both for the prototype and for a new structure are almost always available, so calculation of G doesn't make a big difficulty.

4.2 Dimensionless criterion of structure load-carrying perfection

The disadvantage of the "load-carrying factor" criterion is its dimensionality. It makes difficult the usage of this criterion for comparison of different engineering solutions at very early design stages, when m_o, loads and dimensions of the structure are unknown, thus it is impossible to explicitly estimate of structure weight fraction.

While for the broad range of structures, which allow adequate representation by rod and membrane finite elements, it can be shown that for geometrically similar structures with the same external nodal forces (loads) the load-carrying factor is proportional to the ratio of geometrical similitude [12]. Thus the load-carrying factor is proportional to the characteristic dimension (length) of the structure.

And if we change all nodal forces applied to the structure by factor of k, then also the internal loads within the structure will be changed by factor of k, so as its load-carrying factor. With provision for all stated the above we can introduce the load-carrying factor coefficient

$$C_K = \frac{G}{P \cdot L}, \tag{4.10}$$

where G is load-carrying factor for the structure with some specific load-carrying scheme, dimensions and load distribution; P – characteristic load; L – characteristic

dimension (length). Because the dimension of load-carrying factor is the product of force and length, the C_K is dimensionless.

4.3 Examples of calculations
of load-carrying factor coefficient C_K

Formula (4.10) has a simple physical sense: C_K is a ratio of load-carrying factor G and characteristic load and characteristic length.

Consider the basic problem (figure 4.1a) – transfer of force P_a by distance $ab=1$.

Rod load $N_{ab} = P_a$, load-carrying factor for this one-rod structure:

$$G = N_{ab} \cdot l = P_a \cdot l \qquad (4.11)$$

and

$$C_K = \frac{G}{P_a \cdot l} = 1. \qquad (4.12)$$

Here force P_a is taken as characteristic load, and distance of its transfer is taken as reference length scale.

For the next problem the direction of P_a is rotated by 90°. A structure consisting of two rods ac and ad (figure 4.1b) is proposed. With $\alpha = 45°$ $C_K = 2,00$. The reference length scale is the distance between point a and rigid support – ab.
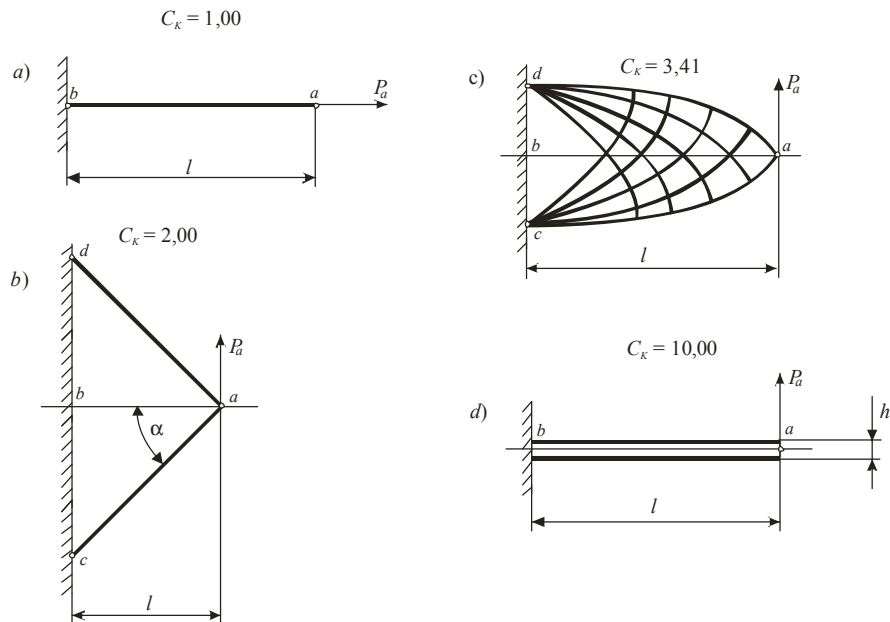
Figure 4.1 – Examples of simple structures

Figure 4.1c show Mitchell frame with geometrical limits $ab/cd=2$, for which $C_K = 3,41$.

For a beam of ideal H-section with $t/b = 0,1$ (figure 4.1d) load-carrying factor computed from loads in caps of spar only is $C_K = 10,00$.

Figure 4.2 shows a simple FEM model of three-layer plate as an example of model wing with planform bc and uniformly distributed load p. The plate is rested vertically at symmetry axis. FEM model consists of shell elements (skin panels and walls).
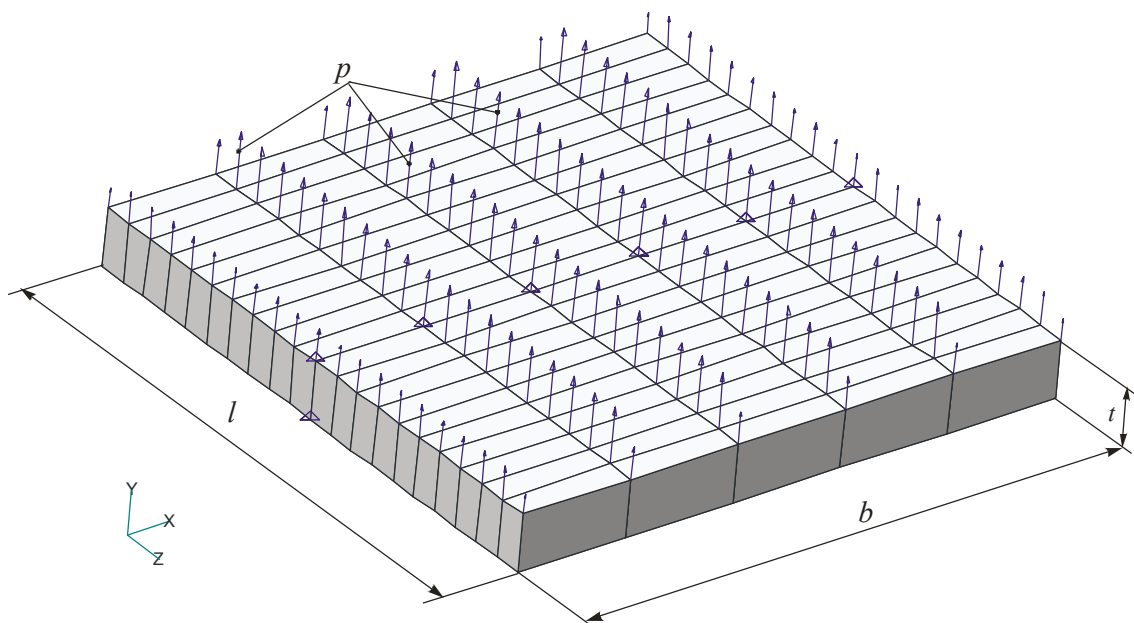
Figure 4.2 – FEM model of a three-layer plate

For $b = c$, which corresponds to aspect ratio $\boldsymbol{A} = 1$, and $t = 0,1c$ load-carrying factor coefficient is $C_K = 1,26$.

Figure 4.3 presents variation of C_K with $b/c = 1; 2; 4; 8; 12$, which make aspect ratio $\boldsymbol{A} = 1; 2; 4; 8; 12$.

Figure 4.4 presents variation of C_K with sweepback angle for aspect ratio $\boldsymbol{A} = 8$.

C_K
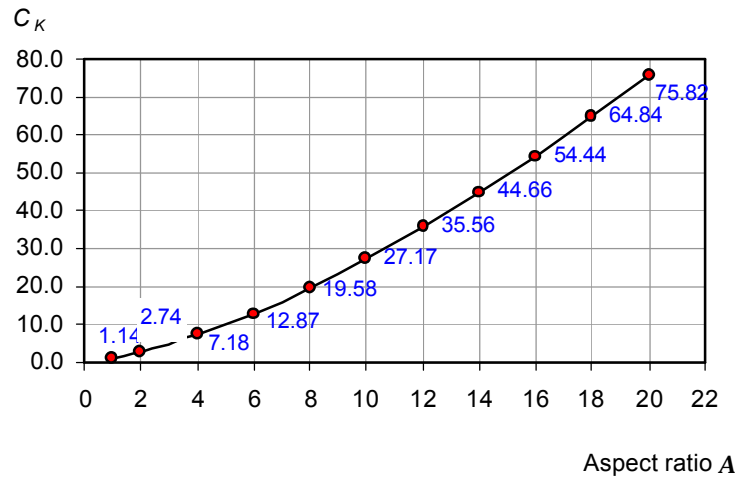
Figure 4.3 – Variation of coefficient C_K with wing aspect ratio

C_K
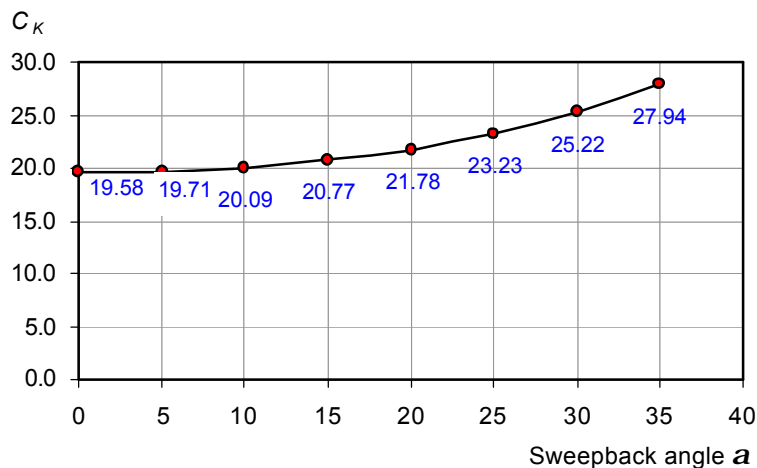
Figure 4.4 – Variation of coefficient C_K with wing sweepback angle

Quite obvious relationships shown at figures 4.3, 4.4 illustrate the possibility of the coefficient C_K to account for geometrical features of the wing. Naturally that for high aspect ratio they are in good agreement with wing weight formulas obtained from beam theory.

Dimensionless load-carrying factor coefficient has a definite physical meaning. Its value shows the ratio between theoretical mass of the considered structure and the mass of the simplest structure consisting of the single rod, transferring the concentrated force along its direction.

The numerical value of the load-carrying factor coefficient depends upon the choice of the structure characteristic length and load distribution. That is why some conventions about the choice of characteristic length and loading are required.

4.4 Wing weight equations based on dimensionless load-carrying factor coefficient

Choosing $\sqrt{S}$ as a characteristic length of the wing and accounting for the above mentioned relations between load-carrying factor and structure dimensions and loads, for geometrically similar wings we can write:

$$G = C_K \cdot n \cdot m_o \cdot g \cdot \sqrt{S} ,\qquad (4.13)$$

where n – load factor, S – wing area.

Relation (4.13) can be used for determination of C_K from the calculation for some geometrically similar wing (values for this wing are marked with "*" sign).

$$C_K = \frac{G^*}{n^* \cdot m_o^* \cdot g \cdot \sqrt{S^*}} \qquad (4.14)$$

In (4.13) and (4.14) $\sqrt{S}$ acts as a dimensional coefficient of geometric similarity – characteristic length, and product $n \cdot m_o \cdot g$ determines the load. Dimensionless magnitude C_K accounts for wing shape, structure and load distribution.

Load-carrying factor coefficient C_K is equal to load-carrying factor for the wing of some definite shape and structure, with unit area and unit net loading.

Accounting for

$$S = \frac{m_o}{p_o} ,\qquad (4.15)$$

where p_o – wing specific load,

We can write (4.13) as

$$G = C_K \cdot n \cdot m_o \cdot g \cdot \sqrt{\frac{m_o}{p_o}} . \qquad (4.16)$$

Then from (4.7) wing mass fracture can be found as

$$\overline{m}_{wing} = \frac{j}{s} C_K \cdot n \cdot g \cdot \sqrt{\frac{m_o}{p_o}} ,\qquad (4.17)$$

or

$$\overline{m}_{wing} = \frac{j}{s} C_K \cdot n \cdot g \cdot \sqrt{S} . \qquad (4.18)$$

Absolute mass of the wing structure will be

$$m_{wing} = \frac{j}{s} C_K \cdot n \cdot m_o \cdot g \cdot \sqrt{S} . \qquad (4.19)$$

Thus, load-carrying factor coefficient is a dimensionless value, which allows calculation of structure absolute mass and mass fracture at early stages of design and, what is the most important, it allows comparison of different load-carrying schemes.

4.5 Load-carrying factor of reinforced panels

On modern aircraft structures (especially in high-loaded wing structures) the main load-carrying element is stringered skin. The most important parameters for such structures are orientation of the stringers and relative skin thickness d:

$$\overline{d} = \frac{d_{skin}}{d_{reduct}} , \qquad (4.20)$$

where d_{skin} – skin thickness; $d_{reduct} = d_{skin} + F_s / b_s$ - reduced panel thickness; F_s and b_s – cross-section area and pitch of the stringers.

Optimal value of $\overline{d}$ rising from stability requirements lies in a narrow range from 0.4 to 0.6, where 0.4 is for panels with high compressive loads acting parallel to the stringers.

According to load-carrying factor definition (4.1, 4.2, 4.3) and its further use for weight estimation (4.7), two strategies for load-carrying factor calculation can be proposed for stringered panels.

Strategy I. Stringered panel is considered as substructure, consisting of the shell skin and a number of rods. Then:

$$G_{pan} = G_{skin} + G_r = s_{skin}^{eqv} \cdot V_{skin} + |s_r| \cdot V_r , \qquad (4.21)$$

where G_{skin} – skin load-carrying factor, G_r – rods load-carrying factor, V_{skin} – skin material volume, V_r – rods material volume, s_{skin}^{eqv} - skin equivalent stress, s_r – rods equivalent stress.

In fact, this strategy for a panel realizes the most general expression (4.3).

Strategy II. The alternative is the calculation of panel load-carrying factor using the values of maximum equivalent stress in the panel and of its full volume:

$$G_{pan} = s_{\max}^{eqv} \cdot V_{pan}, \qquad (4.22)$$

where $s_{\max}^{eqv}$ – maximum equivalent stress in the panel, $V_{pan} = V_{skin} + V_r$ – panel volume.

The purpose of calculating panel load-carrying factor in this way is the estimation of reinforced panel required mass from strength requirements with prescribed value of $\bar{d}$:

$$d_{reduct} = \frac{R^{eqv}}{[s]} = \frac{\sqrt{X^2 + \dfrac{Y^2}{\bar{d}^2} - \dfrac{XY}{\bar{d}} + 3\dfrac{T^2}{\bar{d}^2}}}{[s]}, \qquad (4.23)$$

where R^{eqv} – equivalent force flow in a reinforced panel, X, Y, T – normal and shear force fluxes in the panel.

Notice that for such choice of panel reduced thickness d_{reduct} rod elements can be underloaded.

Special research has shown that wing load-carrying factor is highly dependent on orientation of stringers. Calculation of load-carrying factor G according to strategy I is rational in case when relative skin thickness $\bar{d}$ or stringer orientation can be change during the process of mass optimization. Usage of strategy II is rational for weight estimation of structures with different load-carrying structures, defined by stringer orientation. Implementation of both strategies allows to estimate possibilities for load-carrying structure optimization.

4.6 Application of load-carrying factor coefficient for estimation of weight efficiency of wing load-carrying structure

Consider the application of load-carrying factor coefficient for comparative analysis of load-carrying structures of delta wings as example. For this purpose structures d, e, b from figure 3.2 are chosen, they are numbered 1, 2, 3 respectively. Structures 1 and 2 are widely used and are known as concurrent.

In the first structure spars are span-oriented, which gives the shortest paths of load transfer in the structure, but the longest spars in this case are located in the area of low structural height.

The second structure with spars and stringers coming from the wing tip has its own load-carrying and technological advantages. This structure provides load transfer through the areas with high structural height, cap of spar bevel is constant along the span. The disadvantage is structurally unavoidable otherstrengh of wing panels near the tip. Root rib for this structure should be more thick than for the first one because of the kink of longitudinal load-carrying elements.

Without quantitative analysis it is impossible to choose the best of these two structures, neither it is possible to make an accurate estimate for absolute mass and mass fracture for these wings.

The third structure uses only one spar for torque M_x transfer (from layout requirement). It is interesting, how inefficient this structure in comparison with the first two.

For calculations of load-carrying factor coefficient is such problems it is rational to use advanced implementation of FEM (MSC NASTRAN, ANSYS, ARGON, RIPAK and etc.).

Figure 4.5 presents FEM models for these wings. Airfoil is the same for all three wings, lenticular with relative thickness $\bar{t}$ = 10%. Skin panel and walls are modeled with isotropic elements. Depending upon analysis strategy and features of load-carrying structures rod elements are added, to model caps of spar and stringers.

Aerodynamic loading is considered to be uniform, because the main purpose of the wing load-carrying scheme is transfer of aerodynamic loading to the fuselage and for correct comparison of load-carrying structures some standardization of load distribution is needed.

Geometry is the same for all wings: wing span b is equal to root chord c , belly section - 0,222 b.

Results are presented in table 4.1.
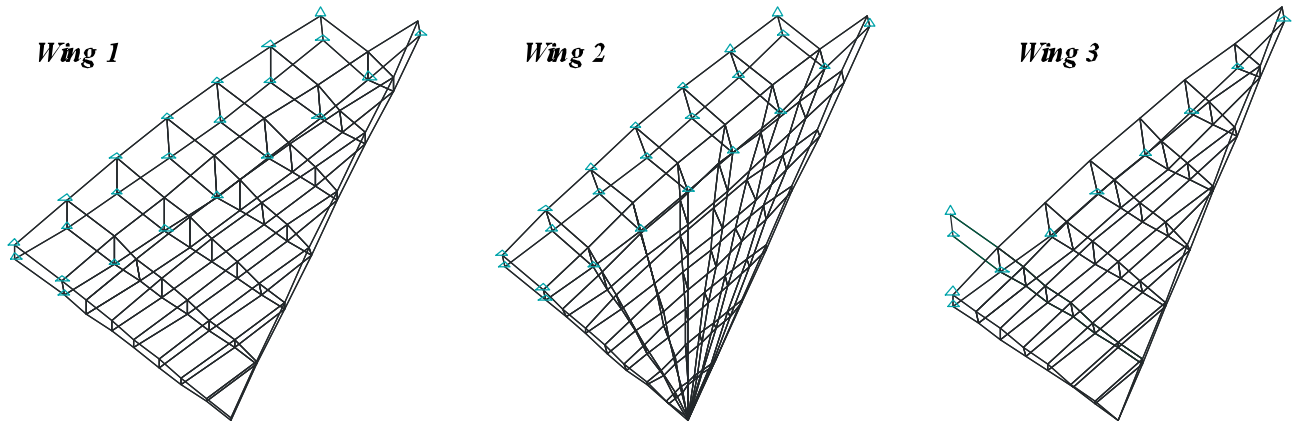
Figure 4.5 – FEM models of the wings

Table 4.1 – Load-carrying factor coefficients for the wings

Wing	Membrane structures	Panel structures					
		Strategy I			Strategy II		
		$\bar{\delta} = 0,6$	$\bar{\delta} = 0,5$	$\bar{\delta} = 0,4$	$\bar{\delta} = 0,6$	$\bar{\delta} = 0,5$	$\bar{\delta} = 0,4$
1	1,62	1,68	1,70	1,71	1,84	1,94	2,07
2	1,68	1,76	1,78	1,81	1,83	1,89	1,98
3	2,55	2,69	2,75	2,83	2,68	3,03	3,56

Models composed of membrane elements only were used for estimation of minimal value of load-carrying factor coefficient which can be achieved for prescribed constraints conditions. As expected, values for wings 1 and 2 are very close. Weight efficiency of the wing 3 is 57 % less (rod elements were used to model the central beam).

Calculations were performed in a following way. From FEM model for each membrane element of the wing skin its area S_m and volume $V_m = S_m \cdot d_{skin}$ were defined. Then volume of rods for the element was calculated

$$V_r = V_m \cdot \frac{1 - \bar{d}}{\bar{d}} . \tag{4.24}$$
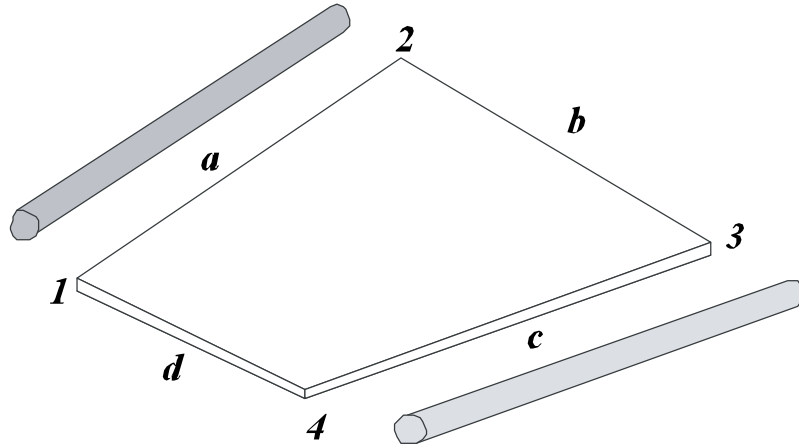
Figure 4.6 – Modeling of stringered panel by shell and rods

From known lengths *a* and c (figure 4.6) cross-section areas for the rods were found:

$$F_r = \frac{V_r}{l_a + l_c}.$$ (4.25)

On nodes 1-2 and 3-4 (in the direction close to stringers) rod elements with cross-section area F_r and lengths l_a and l_c were introduced. Then static calculations were performed, following by calculations of load-carrying factor G according to strategies I and II. Load-carrying factor coefficient was calculated from (4.10), where sum of all nodal forces (loads) in FRM model were taken as a characteristic load:

$$C_K = \frac{G}{\sum_j P_j \cdot \sqrt{S}},$$ (4.26)

where P_j – nodal forces, applied to the console of wing; S – area of wing together with belly section.

From table 4.1 it follows that the results obtained from strategy I are quiet close for all $\bar{d}$ and there is only slight difference from membrane models, which give the estimation for minimal possible value of C_K for prescribed conditions of wing-fuselage joint. Results obtained from strategy II are adequate in accounting for specific of stringered panels straining, thus providing the possibility for objective comparison of load-carrying structures with different values of *d* and calculation of absolute mass and mass fracture for such wings from formulas (4.19, 4.18).

5 Using 3D FEM modeling
for weight calculations

5.1 Theoretical background

Weight analysis of morphing wing requires consideration of unusual external shapes, for which it's very difficult to propose rational airframe structures and create FEM models like those that shown at figure 3.2.

That is why for weight analysis of morphing wing it is reasonable to use 3D continuum FEM models which fill all allowed volume with the account for geometrical constraints, i.e. they have the external shape as that of the wing and do not fill hollows in which it is not allowed to place load-carrying elements due to some reasons. Such models contain all possible airframe structures, including the optimal ones.

Probably for the first time the idea of this aproach was stated in [10]. Basic algorithm for density distribution optimisation for 3D-models presented in [14].

The theoretically required mass of the optimal structure, contained within 3D-model, can be estimated as following.

Consider some hypothetical material with non-uniform density distribution. Consider its strength – allow stress $[s]$, and coefficient of elasticity E are linear functions of density:

$$[s] = r \cdot [\overline{s}], \tag{5.1}$$

$$E = r \cdot \overline{E}, \tag{5.2}$$

where $[\overline{s}]$ and $\overline{E}$ are strength and coefficient of elasticity for unit density.

Assign some amount of this material m for creation of 3D-model. Mesh it with finite elements of "solid" type and assign the same density and coefficient of elasticity for all of the elements:

$$r_{0i} = \frac{m}{V}, \tag{5.3}$$

$$E_{0i} = r_{0i}\overline{E}, \tag{5.4}$$

where subscripts denote: 0 – initial distribution , i – element number, V – total volume of all finite elements of the 3D-model.

Auxiliary optimization problem can be formulated as following:

Minimize potential strain energy of 3D-model

$$U \rightarrow \min \tag{5.5}$$

under the constraint of its constant mass

$$m = const. \tag{5.6}$$

with the assumption that densities of elements can vary, i.e. they are considered as design variables:

$$x_i = r_i, \ i = 1,\ldots n \ , \tag{5.7}$$

where n is the number of elements if the 3D-model.

To solve this problem we use the main idea of [10].

Constrain the variables r_i with mass conservation (5.6)

$$\sum_{i=1}^{n} r_i V_i = m, \tag{5.8}$$

where V_i – volume of element.

Compute the initial uniform distribution of the filler density

$$r_{oi} = m \cdot \left(\sum_{i=1}^{n} V_i \right)^{-1}, \tag{5.9}$$

where V_i is the volume of the element.

Define the principal stresses within elements s_{10i}, s_{20i}, s_{30i} and write down the relationship for 3D-model energy

$$U = \sum_{i=1}^{n} \frac{s_{eqv\,o\,i}^{2}}{2 r_i \overline{\overline{E}}} \cdot V_i. \tag{5.10}$$

Relation (5.10) assumes that stresses in elements are considered as constant, and densities r_i can vary.

To find the optimal values of densities under proposed assumptions we use Langrangian multiplier method [11] and write the following system of equations

$$\begin{cases} \dfrac{\partial U}{\partial r_i} + l \dfrac{\partial j}{\partial r_i} = 0, (i = 1,2,\ldots,n) \\ j(r_i) = \sum_{i=1}^{n} r_i V_i - m = 0, \end{cases} \tag{5.11}$$

where l - Langrangian multiplier , j - auxiliary function, expressing the mass conservation (5.8).

Differentiate with the account for (5.10) and obtain

$$\begin{cases} -\dfrac{\boldsymbol{s}^2_{eqv\,oi}V_i}{2\overline{E}\boldsymbol{r}_i^2} + \boldsymbol{l}\,V_i = 0, (i=1,2,...,n) \\ \displaystyle\sum_{i=1}^{n}\boldsymbol{r}_iV_i - m = 0 \end{cases} \tag{5.12}$$

Whence it follows that

$$\boldsymbol{r}_i = \dfrac{\boldsymbol{s}_{eqv\,oi}}{\sqrt{2\overline{E}\boldsymbol{l}}} \tag{5.13}$$

and with the account for (5.8)

$$\boldsymbol{r}_{1i} = \dfrac{m}{\displaystyle\sum_{i=1}^{n}\boldsymbol{s}_{eqv\,oi}V_i}\boldsymbol{s}_{eqv\,oi}, \tag{5.14}$$

where $\boldsymbol{r}_{1i}$ is the found new density distribution, instead of some initial $\boldsymbol{r}_{oi}$ set, for example, by (5.3).

With stresses $\boldsymbol{s}_{eqvoi}$ corresponding to elements density distribution $\boldsymbol{r}_{oi}$ and new density distribution $\boldsymbol{r}_{1i}$, obtained from solving (5.11) the extremum problem (5.5-5.7) potential strain energy of 3D-model will be lower and become $U_{1-0}<U_0$, where U_0 – potential energy of the initial 3D-model with stresses $\boldsymbol{s}_{(1,2,3)0i}$ and elements density $\boldsymbol{r}_{oi}$; U_{1-0} – energy of 3D-model with stresses $\boldsymbol{s}_{eqvoi}$ and new density distribution $\boldsymbol{r}_{1i}$. Energy U_{1-0} can be calculated by substitution of $\boldsymbol{r}_{1i}$ into (5.10).

But 3D-model with a new density distribution $\boldsymbol{r}_{1i}$ will have another stress distribution $\boldsymbol{s}_{(1,2,3)1i}$, which will satisfy equilibrium and deformation consistency conditions. In a new 3D-model stress distribution $\boldsymbol{s}_{(1,2,3)\,oi}$ will satisfy equilibrium condition only, but not the deformation consistency. Actual potential strain energy of 3D-model with new distribution of density $\boldsymbol{r}_{1i}$ will be U_1 and according to the principle of minimal strain energy

$$U_1<U_{1-0}. \tag{5.15}$$

Using the new distribution $\boldsymbol{r}_{1i}$ as the initial one and making successive calculations of structure stress state according to (5.14), we get a sequence of structures with energies

$$U_0>U_1>U_2>\ldots \tag{5.16}$$

This monotonically decreasing sequence is limited from below, because the strain energy is always positive, and thus it is convergent. Reduction of the energy to the minimal possible value means a search for density distribution into 3D-model that gives the maximal structure stiffness.

We can also prove [11] that this iteration process yields to the structure with minimal value $\sum_{i=1}^{n} s_{eqv\,i} \cdot V_i$, i.e. with minimal load-carrying factor G, calculated by (4.3).

The knowledge of this value allows as to determine from (4.7) the minimal theoretically required mass of the structure, which can be designed with the account for geometrical constraints.

In the proposed iteration process high-loaded elements will increase their density and low-loaded will decrease. And variation of density will continue until all the elements with non-zero density will have will have equal specific strain energy to density ratio. Density of some elements will be nearly zero, which indicate non-rationality of placement of load-carrying elements in these zones.

5.2 Methodology of testing

During the calculations (5.14) new values of element densities are assigned proportionally to the equivalent stresses within them. Because for weight analysis we are interested in the minimal possible value of the load-carrying factor, corresponding to the given density distribution, these densities can be evaluated with more simple relation:

$$r_{1i} = \frac{s_{eqv\,oi}}{[\overline{s}]} . \tag{5.17}$$

As an example consider the calculation of load-carrying factor for 3D-model of the wing structure (figure 5.1).
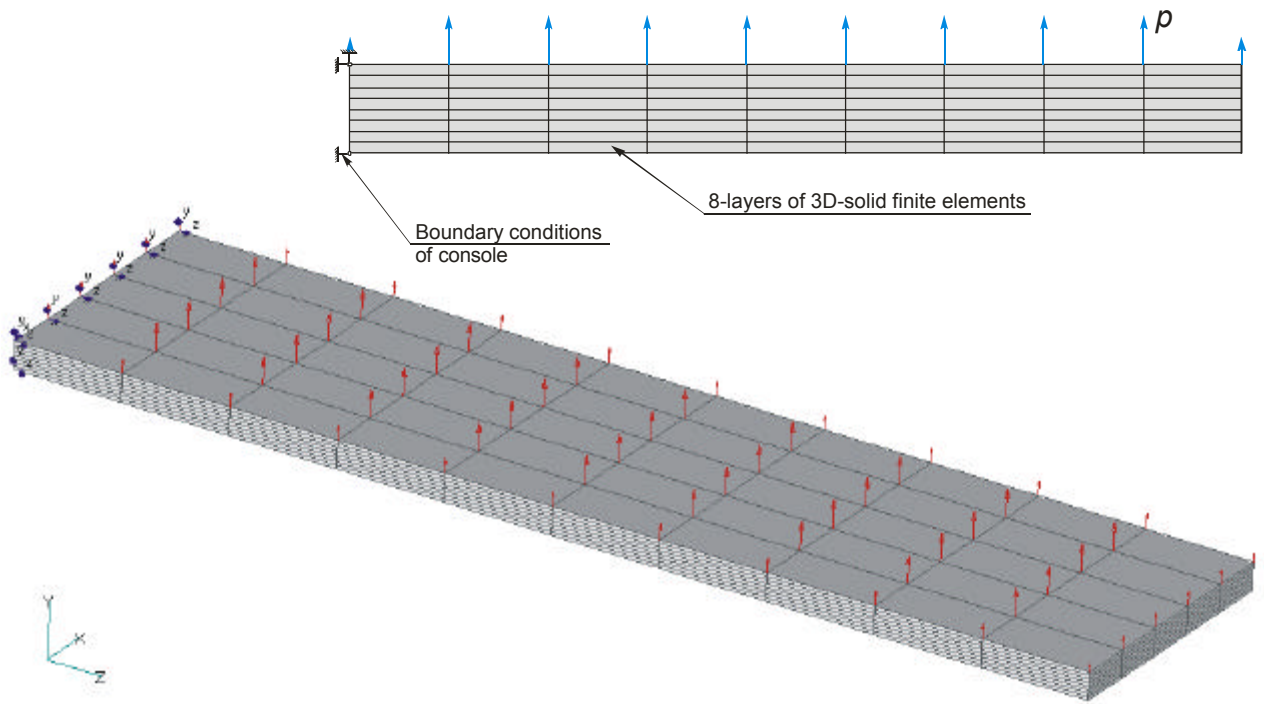
Figure 5.1 – 3D-model of the wing structure

Figure 5.1 shows wing box structure with $b/c = 8$, $t/c = 0.1$, fixed in the root section and loaded with uniformly distributed load. Calculation of theoretically optimal thin-wall structure, consisting of isotropic skins and shear-carrying walls, yields for the given geometrical constraints the value of load-carrying factor coefficient $C_K = 19{,}58$ (figure 5.2). Calculation for the wing model consisting of solid elements in case of uniform density distribution yields $C_K = 28{,}10$. But in the iteration optimization process for density distribution after only 10 iterations we obtain $C_K = 22{,}11$ with 8-layer meshing of 3D wing model, which can be considered reasonable for estimation purposes. As it was expected, in course of optimization density of the high-loaded surface layers was increased.
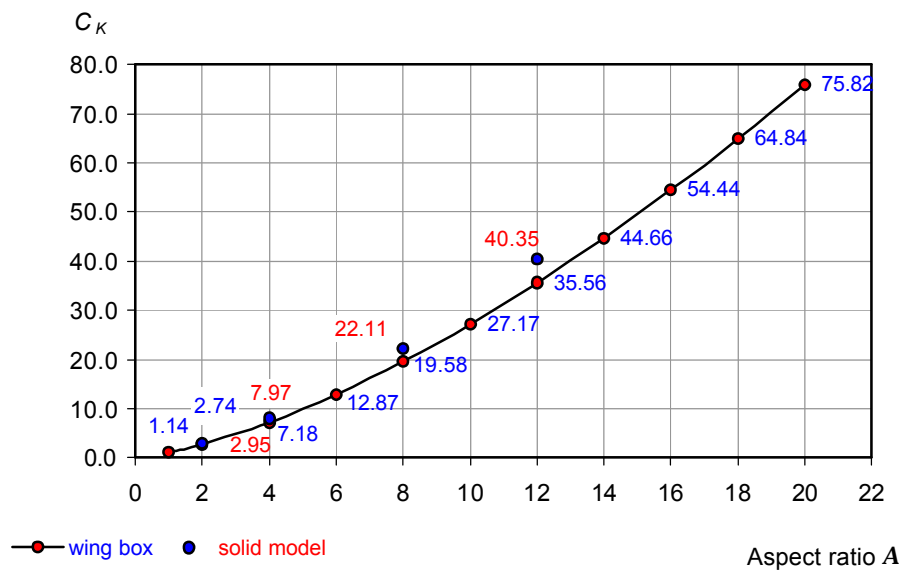
Figure 5.2 – Load-carrying factor coefficient of wing for different aspect ratio

Investigation for aspect ratio $A = 2, 4, 8, 12$ is shown at figures 5.2 and 5.3.
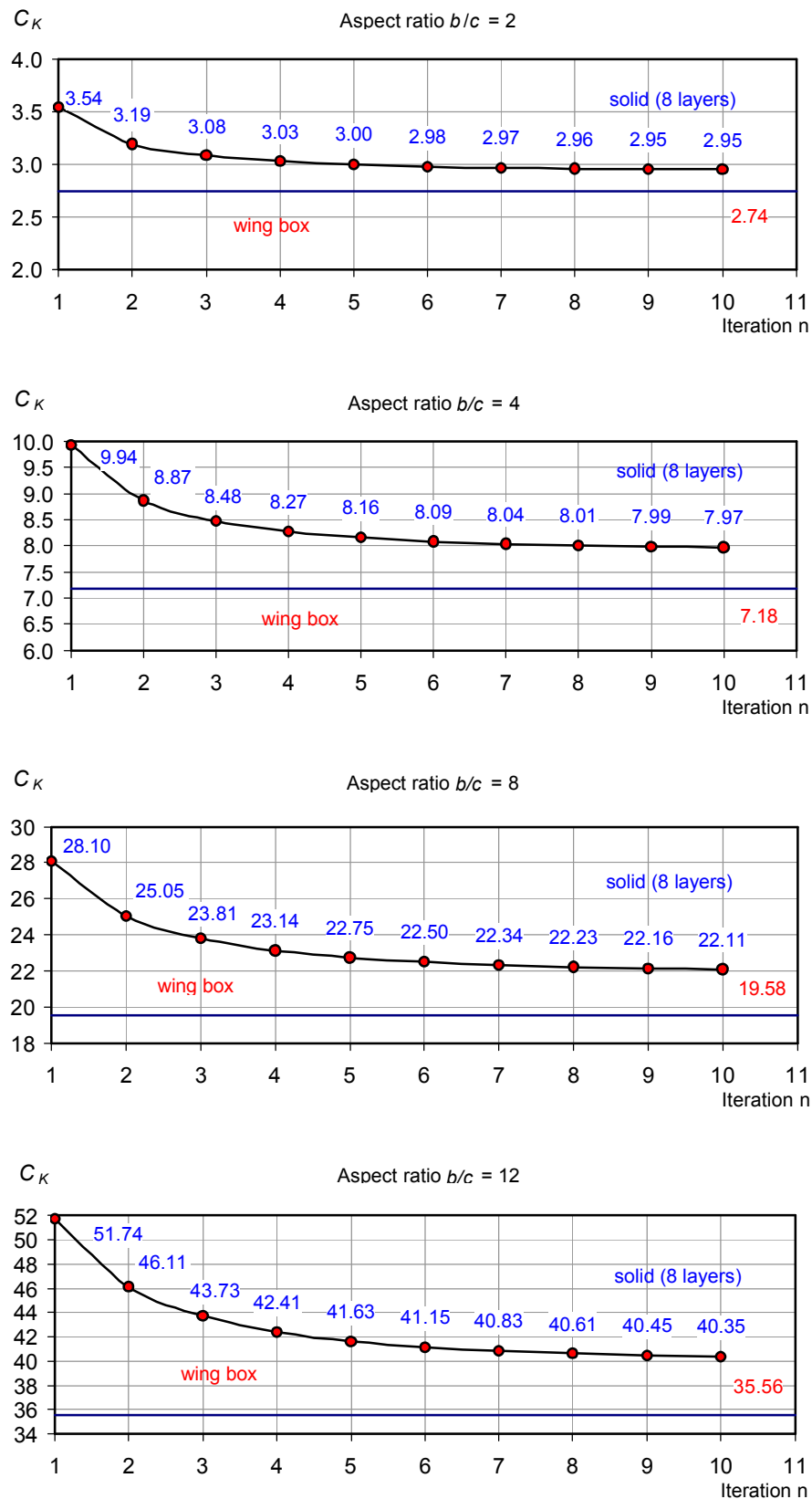
Figure 5.3 – Comparison of load-carrying factor coefficient calculations for thin-wall structure and for 3D-solid model with variable density

From 8-layer model the value of C_K is 12% higher comparing with ideal structure, as it was expected. It is explained by the fact that for the optimal density distribution in 8-layer 3D model the real wing thickness will be 7/8 t.

As the number of layers in the model increased, the results of C_K calculation with 3D model approach asymptotically to the theoretical optimum. But because of the necessity to consider multiple variants of the structure, only 8-layer models were used in all calculations of this research.

Thus 3D-modelling allows to obtain the estimation of theoretically necessary mass of the structure with reasonable accuracy and considerably simplifies preparation of FEM models.

6 Full weight coefficient estimation

Full mass coefficient was calculated for the wing of maneuvering aircraft Yakovlev Yak-130. General drawing of the aircraft is shown at figure 6.1. Finite-element model of the wing developed for the calculation of j is shown at figure 6.2. Calculations provided the value j = 3,3.
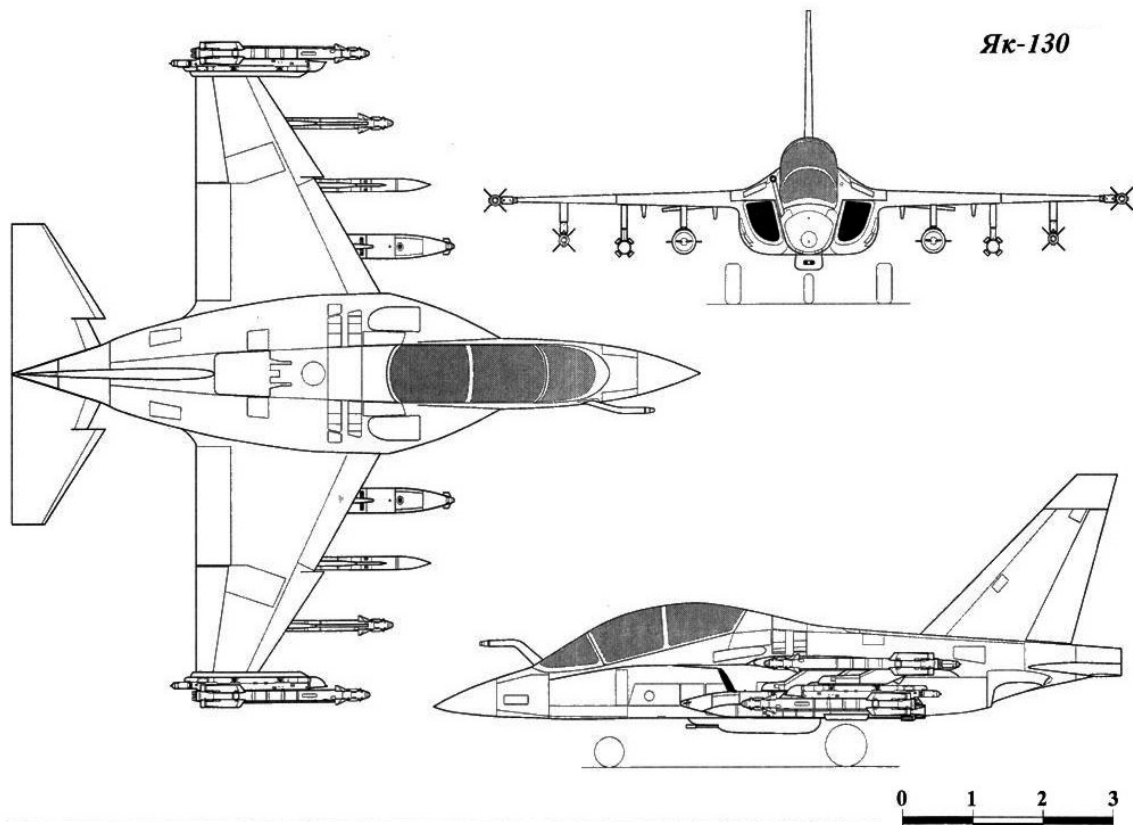
Figure 6.1 – Layout of maneuver airplane Yak-130
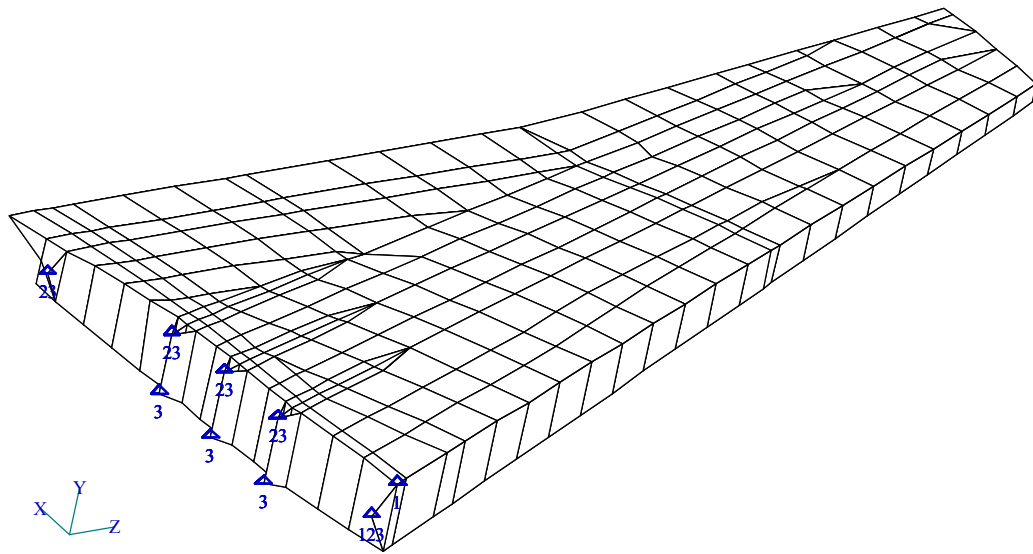
Figure 6.2 – Finite-element model of Yak-130 wing

Because there are no prototypes of telescope wings available nowadays, now the full mass coefficient is being calculated for the flap of a liner wing. It was chosen as one of the possible prototypes because its design includes rails and contact pairs. 3D-model for calculation of j is shown at figure 6.3.

For this structure full mass coefficient about 5 was obtained.

Calculation for flap was performed with one load case only. This of course yields underestimated value of load-carrying factor for this structure, especially for the rail, and consequently results in overestimated value of full mass coefficient.

The same result was obtained for slat (figure 6.4).

The method for calculation of full mass coefficient for movable aircraft structures require additional investigation.
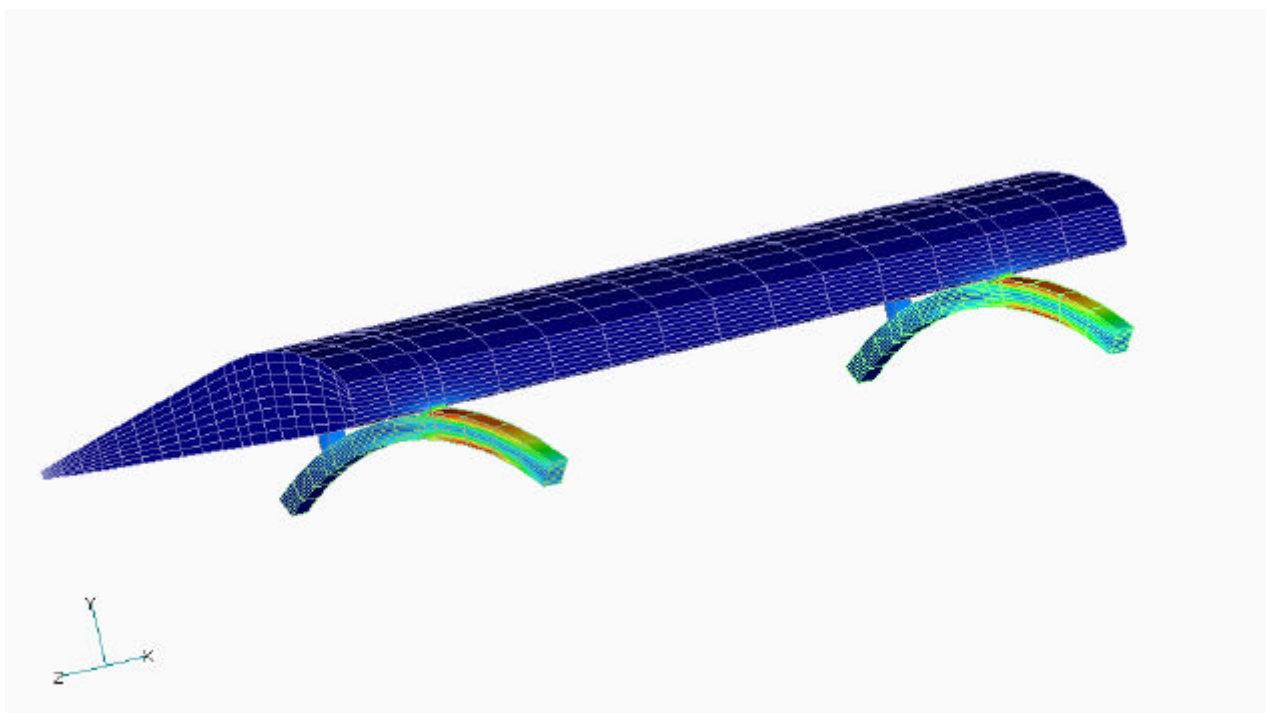
Figure 6.3 – Finite-element model of a flap
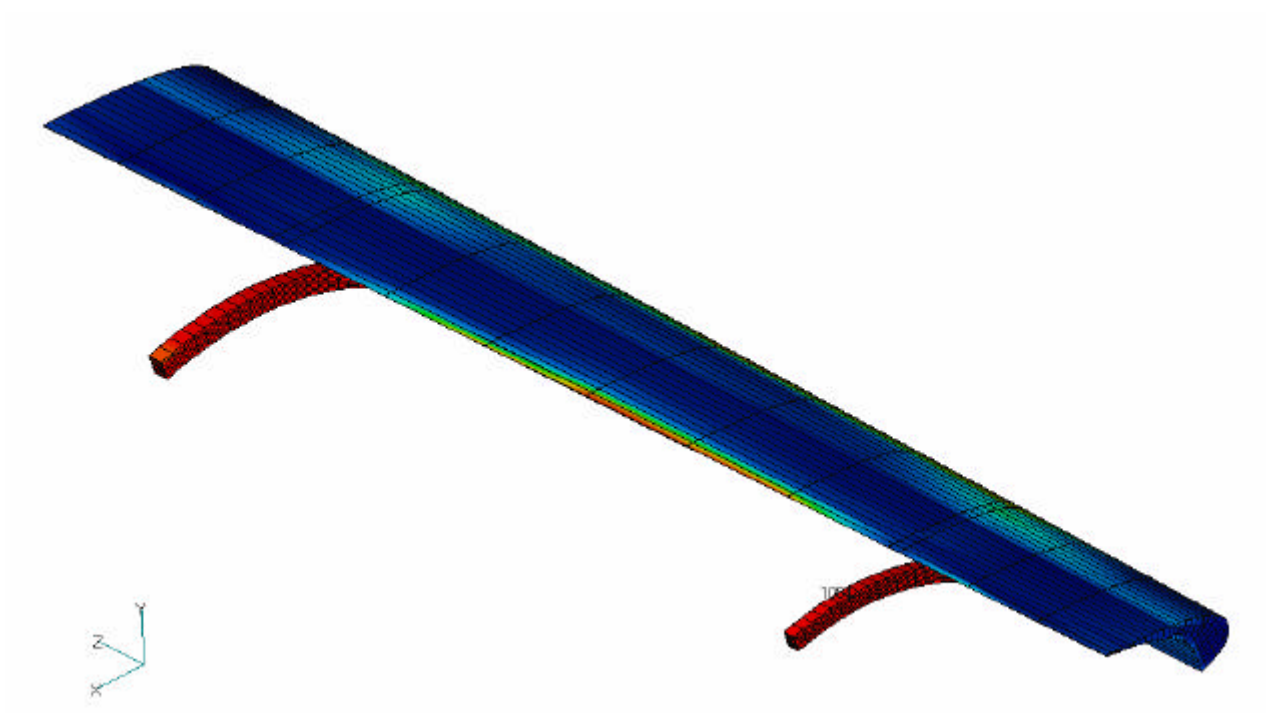
Figure 6.4 – Finite-element model of a slat

7 Computational research telescope wings aerodynamics

7.1 Brief description of computational method of aerodynamic calculations

The method for calculations of telescope wing aerodynamics basing on discrete vortex method with linear formulation [2, 6, 8] was used for calculations of angle of attack derivatives of lift coefficient and pitching moment coefficient, and drag due to lift factor. Zero lift drag was calculated with empirical formula, basing upon equivalent flat plate skin friction.

Main ideas of discrete vortex method are widely known and used for aerodynamic calculations. The wing is replaced by N chordwise strips, and each strip is divided by n panels. At each panel an oblique horseshoe vortex and an impermeability point (collocation point) are placed. Computational scheme "1/4 – 3/4" was used in the present method. In this scheme the attached horseshoe vortex is located 1/4 of the panel chord from the leading edge of the panel, and collocation point 3/4 of the panel chord from the leading edge of the panel (figure 7.1).
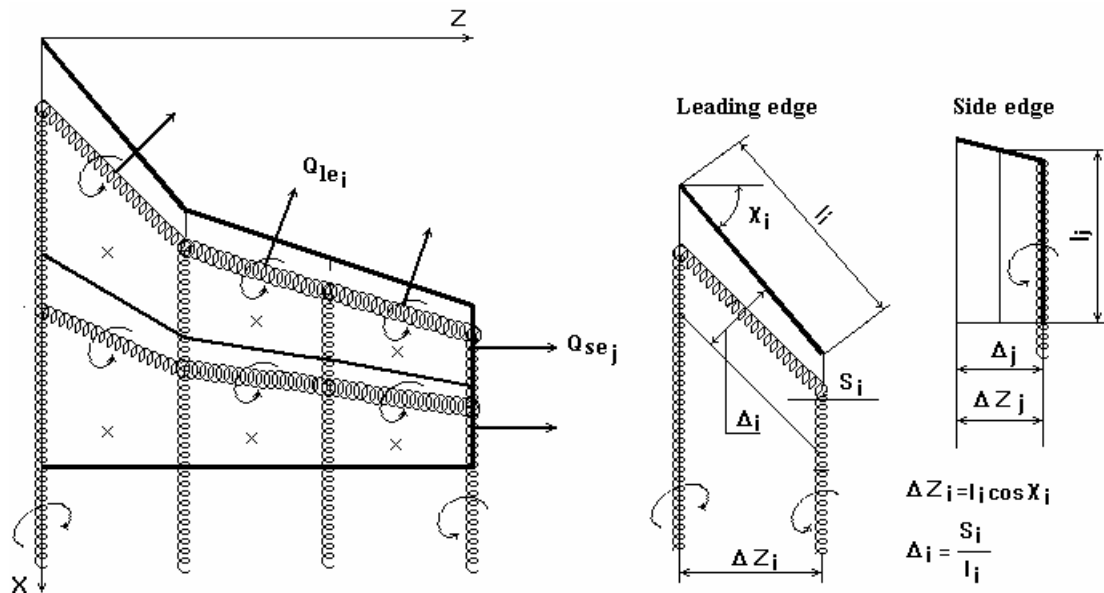
Figure 7.1 – Computational scheme of discrete vortex method

Impermeability condition satisfied in the collocation points yields to the system of linear algebraic equations about unknown intensities of the vortices:

$$\sum_{i=1}^{m}(w_{yij}+\Delta w_{yij})\Gamma_i^{\boldsymbol{a}}=-2\boldsymbol{p}, \quad j=\overline{1,m}; \tag{7.1}$$

where $w_{yij}=w_y\!\left(\boldsymbol{x}_{0ij}, \boldsymbol{V}_{0ij}, \Lambda_{\boldsymbol{m}}\right)$ is dimensionless velocity induced by vortex with number i in the collocation point with number j;

$\Delta w_{yij}=w_y\!\left(\boldsymbol{x}_{0ij}, \Delta \boldsymbol{V}_{0ij}, \Lambda_{\boldsymbol{m}}\right)$ is additional dimensionless velocity induced in the collocation point j by the mirrored vortex symmetrical to vortex i;

$\boldsymbol{x}_{0ij}, \boldsymbol{V}_{0ij}$ are coordinates of collocation point in the coordinate system with the origin in the middle of the vortex;

$\Lambda_{\boldsymbol{m}}$ is sweepback angle of the vortex.

Solving system (7.1) we obtain $\Gamma_i^{\boldsymbol{a}}$ and the integral aerodynamic parameters of the wing can be found as following:

$$C_{L_{\boldsymbol{a}}}=\frac{A}{N^2}\sum_{i=1}^{m}\Gamma_i^{\boldsymbol{a}} \tag{7.2}$$

$$C_{m_{\boldsymbol{a}}}=\frac{A}{N^2}\sum_{i=1}^{m}\Gamma_i^{\boldsymbol{a}}\frac{x_i}{c_A}, \tag{7.3}$$

$$\overline{x}_F^{\boldsymbol{a}}=-\frac{C_{m_{\boldsymbol{a}}}}{C_{L_{\boldsymbol{a}}}}, \tag{7.4}$$

$$C_{L_{\boldsymbol{a}}\sec}=\frac{1}{N}\frac{l}{c_{\sec}}\sum_{i=1}^{n}\Gamma_i^{\boldsymbol{a}}, \tag{7.5}$$

$$\overline{\Gamma}=\frac{C_{y\sec}^{\boldsymbol{a}}c_{\sec}}{C_y^{\boldsymbol{a}}c_m}, \tag{7.6}$$

where x_i is the coordinate of the middle point of i-th horseshoe bound vortex.

Zero lift drag coefficient of the wing was calculated as

$$C_{D_0}=2C_f\left(0{,}93+2{,}8\,\overline{t}\right)\left(1+5\,\overline{t}M^4\right), \tag{7.7}$$

flat-plate skin friction coefficient was calculated as the sum

$$2C_f=2C_{f1}\frac{S_1}{S}+2C_{f2}\frac{S_2}{S}, \tag{7.8}$$

flat-plate skin friction coefficient for each part of the wing was calculated according to Reynolds number under the assumption of turbulent boundary layer

$$2C_{fi} = \frac{0,91}{\left(1+0,1M^2\right)\left[\log\left(\frac{Re_i}{\left(1+0,1M^2\right)}\right)\right]^{2,58}} \cdot \quad (7.9)$$

Reynolds number for each part of the wing was based on its mean chord

$$Re_i = \frac{V \cdot c_i}{v}.$$

Coefficient of kinematic viscosity was taken from standard atmosphere for the altitude of $0\ m$.

Maximum lift-to-drag ratio was calculated as

$$L/D_{MAX} = \frac{1}{2\sqrt{C_{D_o} \cdot K}}$$

7.2 Testing of computational program for calculation of spanwise circulation distribution

In order to validate calculation results obtained with discrete vortex method [2, 6] a number of test calculations were performed for trapezoidal wings, geometrically similar to the considered telescope wing. Table 7.1 presents comparison for two wings of the same aspect ratio 10 and same leading edge sweepback angle, obtained from linear discrete vortex method [8].

Table 7.1 – Computed angle of attack derivative of lift coefficient for two trapezoidal wings

Wing	C_{L_a}, from paper [3], mesh 12?4	C_{L_a}, present calculations, mesh 200?20	Relative error, %
$A = 10$; $l = 1.0$; $L_{le} = 0.17$	4,951608	4,842948	2,24
$A = 10$; $l = 0.5$; $L_{le} = 0.17$	5,069728	4,983007	1,74

Figures 7.2 and 7.3 show spanwise distribution of dimensionless circulation. A good agreement between the results can be seen. The difference in the values of C_{L_a}, which is visible in table 7.1, can be explained by the difference in computational grids. It is obvious that the more fine grid used in present calculations provides more accurate result.
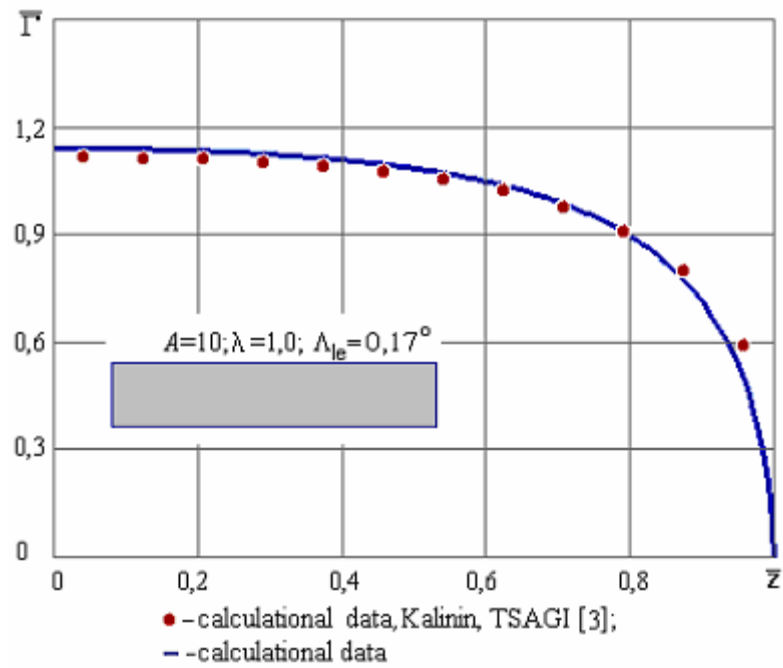
Figure 7.2 – Spanwise load distribution for the wing with unit taper ratio
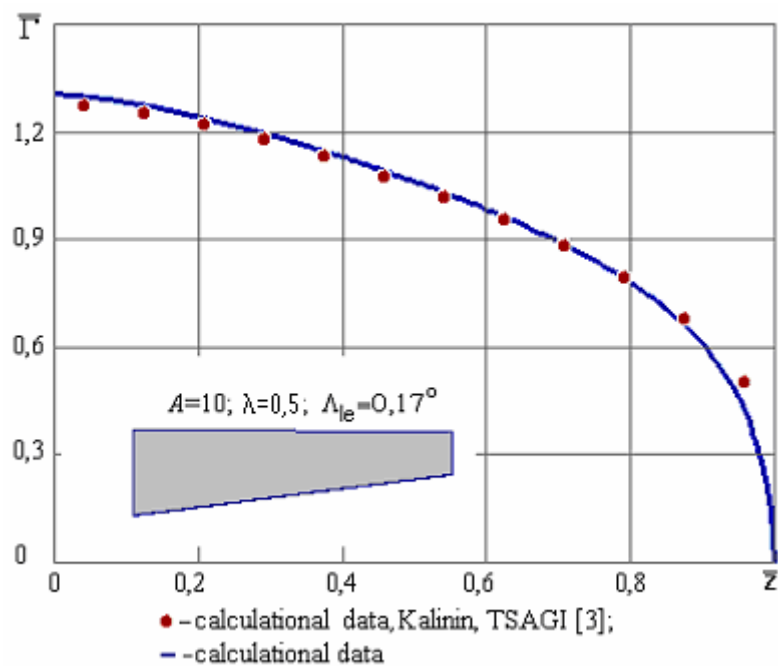
Figure 7.3 – Spanwise load distribution for the wing with taper ratio 0.5

Figures 7.4 and 7.5 shows comparison of computational results with experimental data.
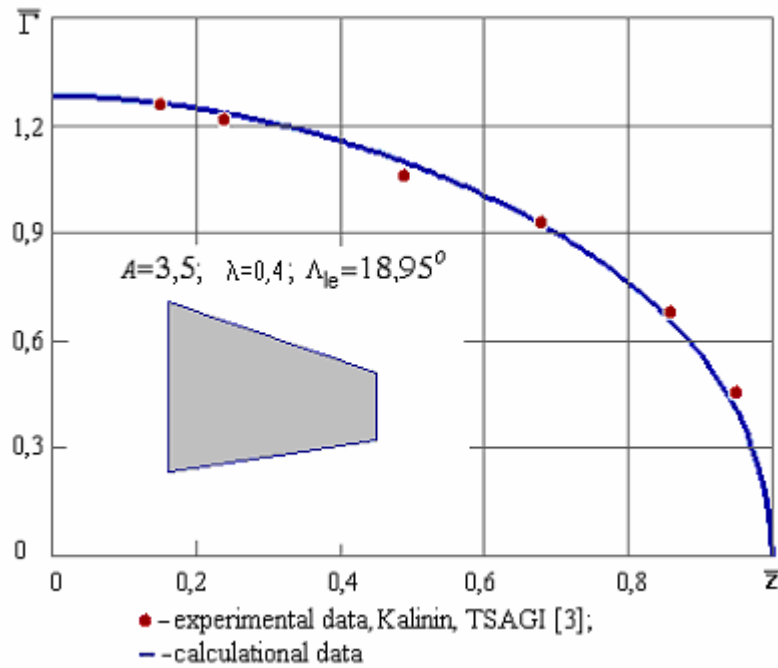
Figure 7.4 – Spanwise load distribution for the wing with taper ratio 0.4
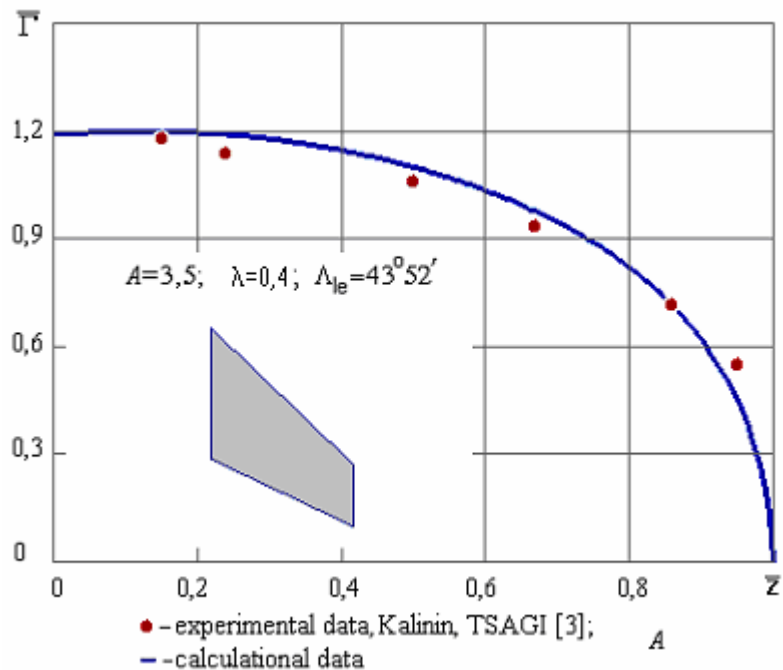
Figure 7.5 – Spanwise load distribution for the sweptback wing with taper ratio 0.4

Comparison with other calculations and experimental data has shown a good agreement.

Table 7.2 presents aerodynamic performance for the trapezoidal wing with aspect ratio $A = 10,964$ and taper ratio $l = 0,5$ (wing W_2b) and for the telescope wing (wing W_2a) calculated with discrete vortex method. Zero lift drag coefficient was calculated for the airspeed 35 *m/s*.

Table 7.2 – Calculated aerodynamic performance of trapezoidal and telescope wing

Wing	Aspect ratio	Area, m^2	C_{L_a}	C_{m_a}	$-\overline{x}_F^{\,a}$	C_{D_0}	K	L/D_{max}	Mesh
W_2a	10.800	0,012	5,0127	-0,0240	0,2746	0,0185	0,0301	21,179	96?20+48?20
W_2b	10,964	0,012	4,9938	-0,0259	0,2976	0,0229	0,0297	19,185	100?20

Calculations were performed for the models which were tested in the wind-tunnel (see section 8). Table 7.3 and figure 7.6 present results for four telescope wings with different span of the movable part.

Table 7.3 – Calculated aerodynamic performance of four different telescope wings

Wing	Aspect ratio	Area, m^2	C_{L_a}	C_{m_a}	$-\overline{x}_F^{\,a}$	C_{D_0}	K	L/D_{max}	Mesh
W_05	3,273	0,110	3,3363	-0,0141	0,2437	0,0124	0,0979	14,338	125?20+25?20
W_15	4,923	0,130	3,9739	-0,0191	0,2755	0,0127	0,0653	17,357	125?20+75?20
W_20	5,786	0,140	4,1887	-0.0209	0,2856	0,0128	0,0557	18,717	100?20+80?20
W_30	7,562	0,160	4,5021	-0.0236	0,3002	0,0130	0,0427	21,211	75?20+90?20
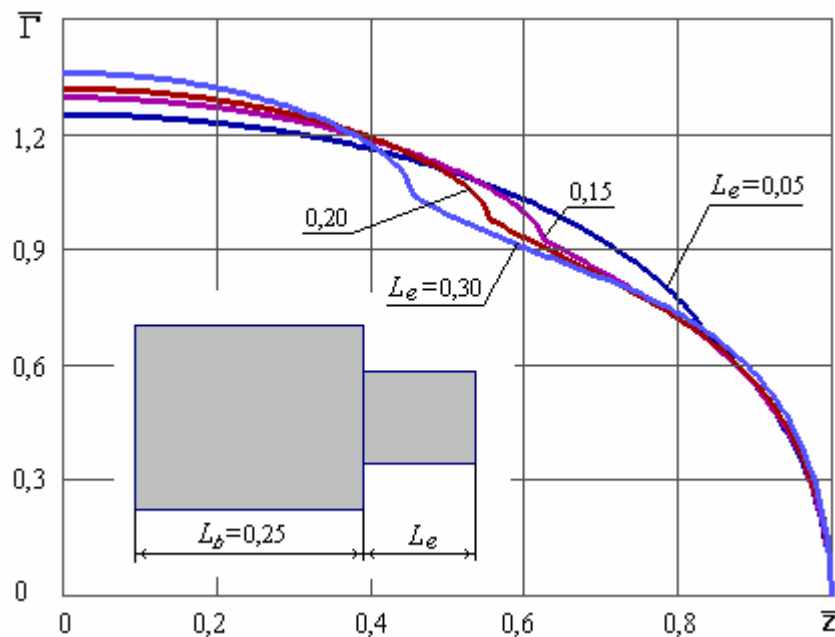
Figure 7.6 – Spanwise load distribution for four different telescope wings

The calculations have shown that the increase of the relative span of the movable part of the telescope wing results in the more sharp "kink" of the load distribution at the joint between the two parts.

7.3 Results of the calculations

Results of the calculations for six different wings shown at figure 7.7 are considered.
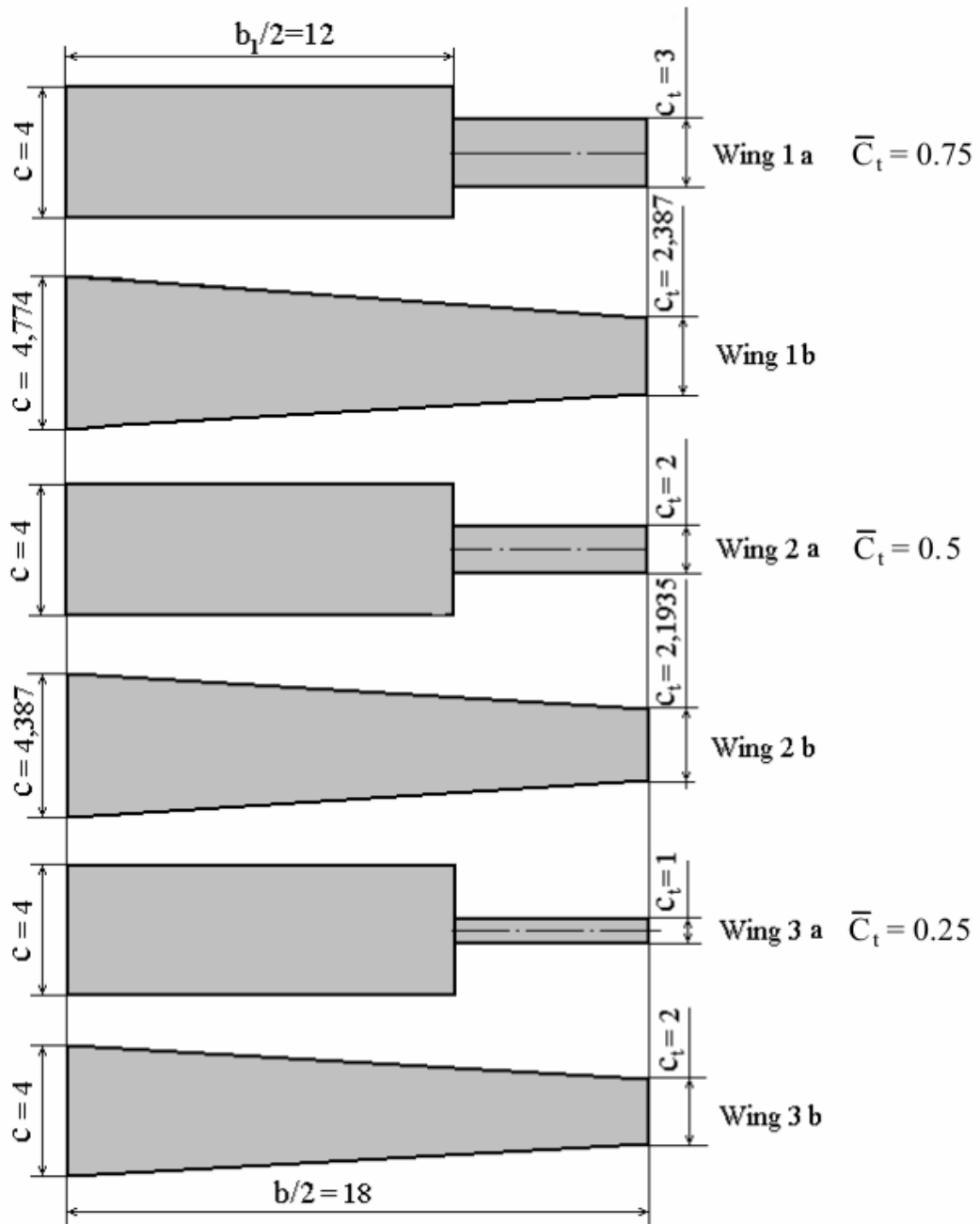
Figure 7.7 – Geometry of the wings

The table 7.4 below shows aerodynamic coefficients for all of the six wings.

Table 7.4 – Aerodynamic coefficients for all of the six wings

$\overline{c}_t$	b/2 – 18	Wing
0,75	$A = 9.818; C_{L_a} = 4.9197; K = 0.0354;$ $C_{D_o} = 0.00636; L/D_{MAX} = 33.290$	1a
–	$A = 10.058; C_{L_a} = 4.9362; K = 0.0323;$ $C_{D_o} = 0.00643; L/D_{MAX} = 34.692$	1b
0,5	$A = 10.800; C_{L_a} = 5.0183; K = 0.0301;$ $C_{D_o} = 0.00639; L/D_{MAX} = 36.051$	2a
–	$A = 10.941; C_{L_a} = 5.0238; K = 0.0297;$ $C_{D_o} = 0.00653; L/D_{MAX} = 35.895$	2b
0,25	$A = 12.000; C_{L_a} = 4.9096; K = 0.0311;$ $C_{D_o} = 0.00638; L/D_{MAX} = 35.461$	3a
–	$A = 12.000; C_{L_a} = 5.1146; K = 0.0272;$ $C_{D_o} = 0.00663; L/D_{MAX} = 37.257$	3b

Figure 7.8 shows the spanwise load distribution for the telescope wings. Figures 7.9 and 7.10 present the spanwise distribution of dimensionless velocity circulation for wings 1 and 5.
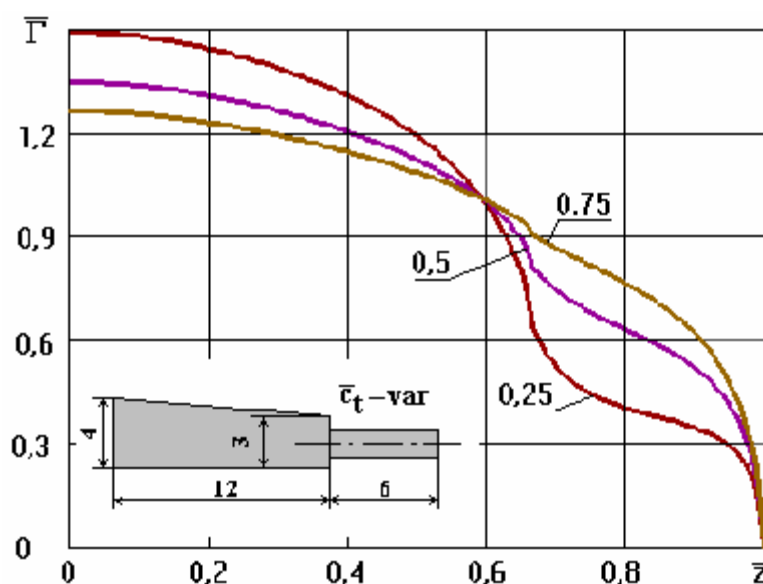
Figure 7.8 – Spanwise load distribution for the telescope wing with semispan 18
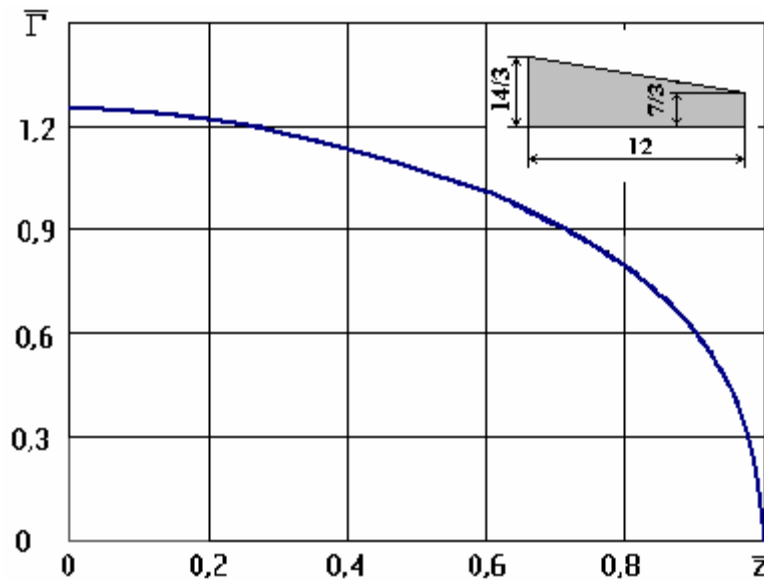
Figure 7.9 – Spanwise load distribution for trapezoidal wing "1"
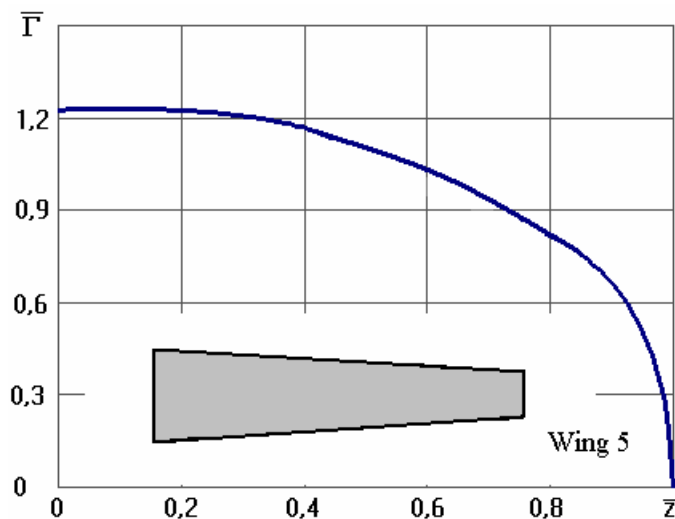
Figure 7.10 – Spanwise load distribution for trapezoidal wing "5"

As one can see from the table 7.4, the telescope wing with $\overline{c}_t = 0.5$ (wing 2a) provides more lift and has better aerodynamic efficiency.

Figure 7.11 presents spanwise load distribution for the rectangular wing with aspect ratio $A = 6,0$.
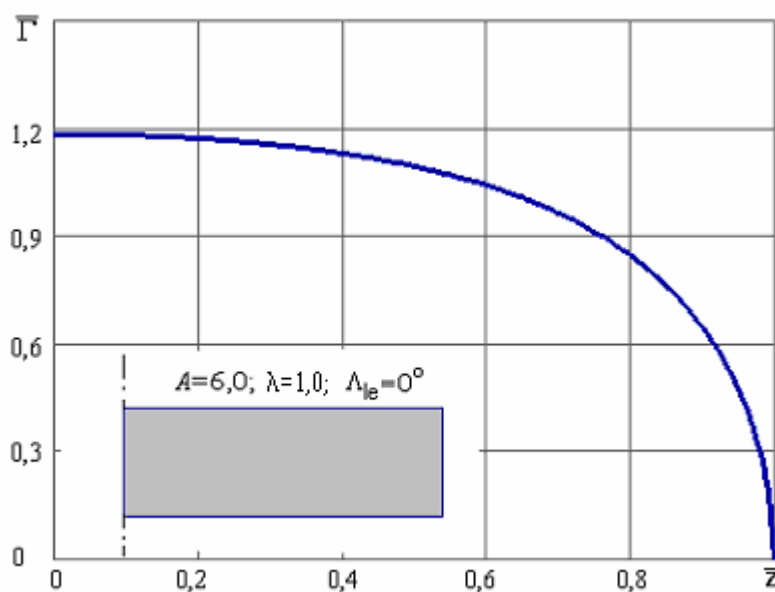
Figure 7.11 – Spanwise load distribution for the rectangular wing with aspect ratio $A = 6,0$

Table 7.5 presents calculated aerodynamic performance for the rectangular wing with aspect ratio $A = 6,0$.

Table 7.5 – Calculated aerodynamic performance for the rectangular wing with aspect ratio $A = 6.0$

Wing	Aspect ratio	Area, m^2	C_{L_a}	C_{m_a}	$\overline{x}_F^{-a}$	C_{D_0}	K	L/D_{max}	Mesh
W_6	6,0	96,0	4,2179	-0,0175	0,2388	0,0078	0,0601	23,112	192?20

7.4 Results of numerical simulations
for the test model with pressure orifices

For computational identification of loads and pressure distribution a CFD model was created using Star-CD™ software. This software is developed by CD-Adapco®, permanent academic license was provided to SSAU by Russian representation of distributing company CAD-FEM GmbH. This software provides solution to general governing equations of fluid dynamics (Navier-Stokes equations) with finite volume method.

CAD model of the telescope wing is shown at figure 7.12. It has the same dimensions as the wind-tunnel test model, designed for study of pressure distribution, which is described in the next section. Figure 7.13 shows the details of the surface mesh in the joint area. For both parts of the wing mesh is collocated to the joint in order to provide accurate resolution of the sharp gradients of the flow parameters which are expected in this region. The size of the mesh cell near the joint is about 0,2 mm in spanwise direction.
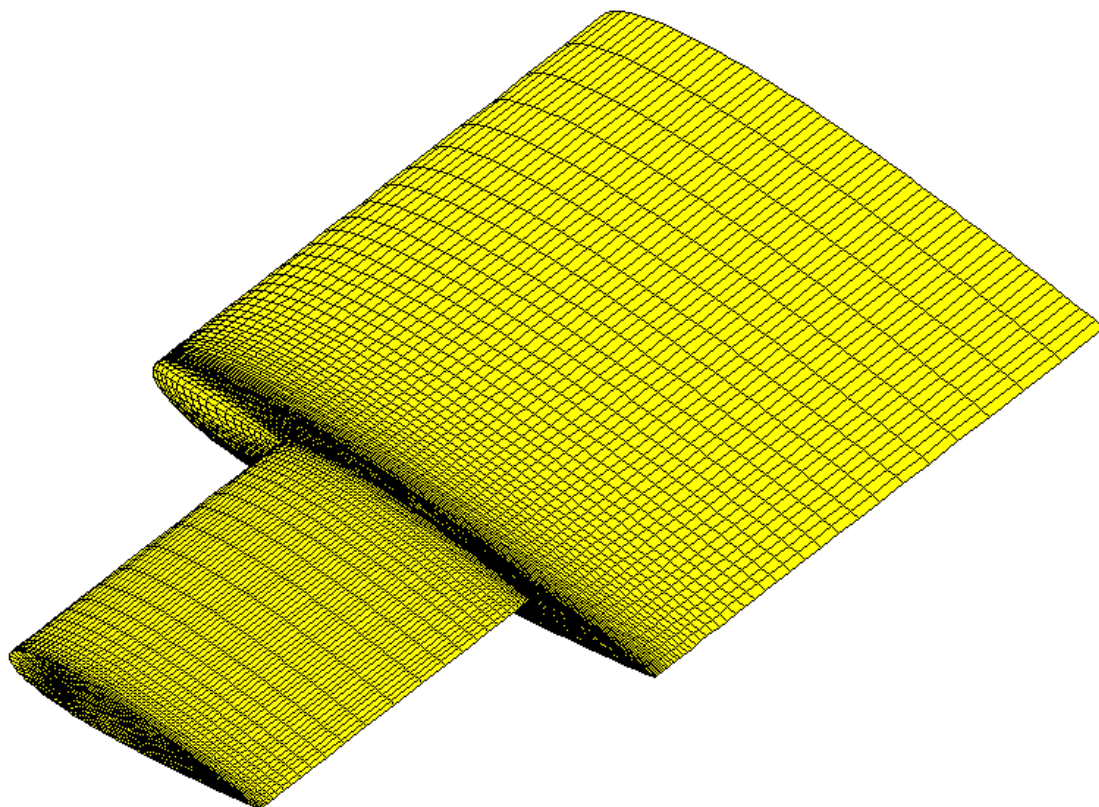
Figure 7.12 – Geometrical model of the telescope wing
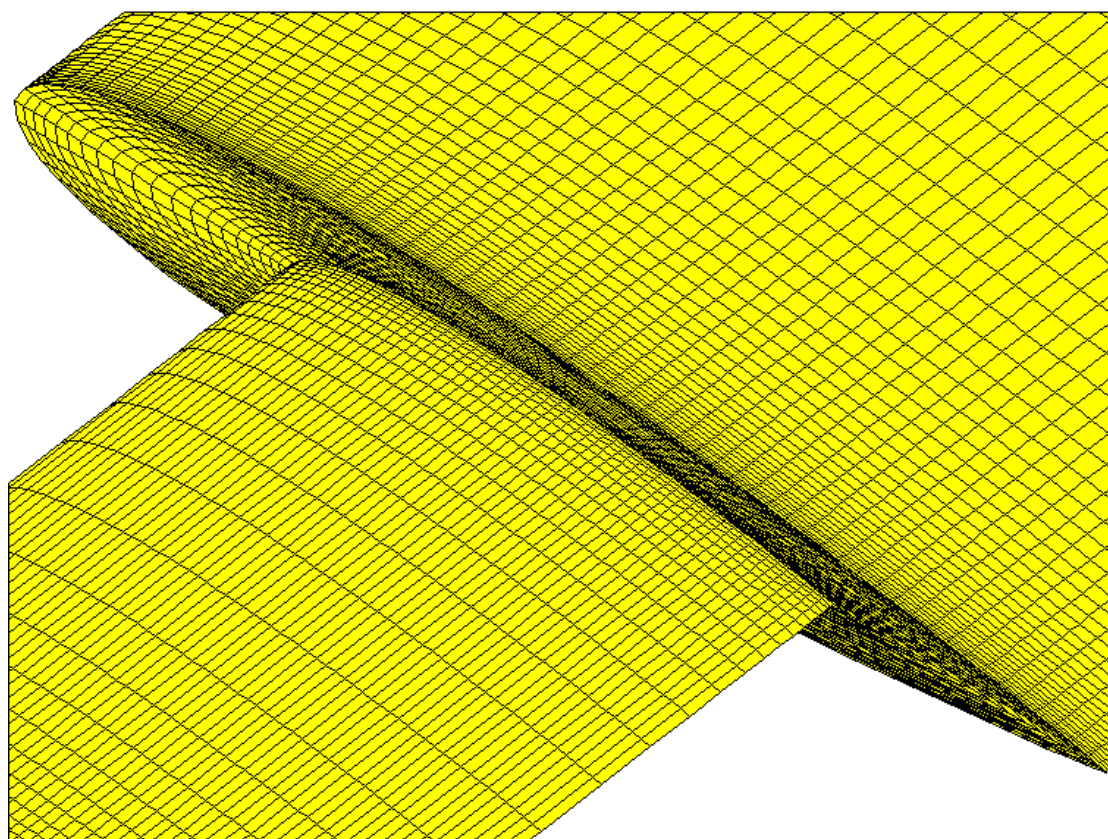
Figure 7.13 – Mesh in the joint area

Figure 7.14 shows the general view of the computational domain around the telescope wing, and figures 7.15 and 7.16 the same domain as it is seen when viewed along *Z, X* and *Y* axis of global Cartesian coordinate system. Global Cartesian coordinate system is connected to the wing and the directions of its axis correspond to usually assumed in aerodynamics – *X* is pointing backwards (streamwise) along the root chord, *Y* is pointing up, *Z* is pointing in spanwise direction.

Only one half of the wing was considered in order to reduce computational expenses, i.e. the flow was considered to be symmetrical. Distances between the wing and the boundaries of the computational domain were taken according to standard practice in CFD simulations. Inlet, upper and lower boundaries were located 10 chords away from the wing, outlet boundary – 20 chords away. Side boundary was located one span away from the wing. Such choice of computational domain is a compromise between computational expenses and influence of boundary conditions. The computational model consists from more than 1 200 000 cells, the mesh is collocated from the boundaries to the wing.

Components of the free-stream velocity vector were imposed at inlet, upper and lower boundaries, according to the values of airspeed and angle of attack. All simulations were performed for the airspeed 35 *m/s*, angles of attack were 0°, 2°, 4°, 6°, 8°, 10°. The flow was considered as fully turbulent (Reynolds number Re = $4,6 \cdot 10^5$), thus turbulence parameters were also imposed at these boundaries – turbulence intensity 1%, turbulence length scale 0,001 *m*.
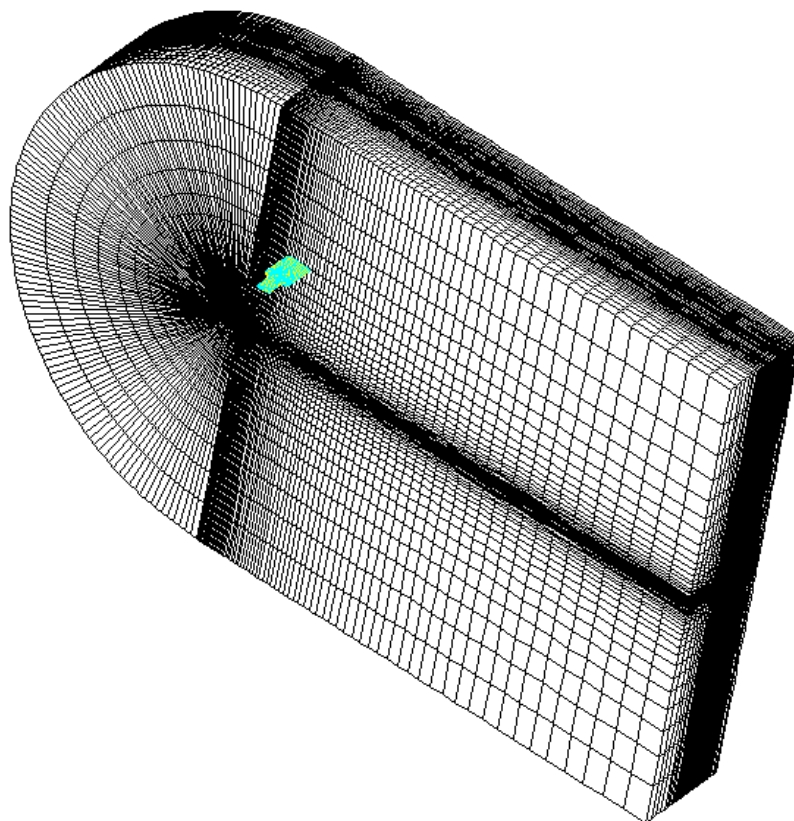
Figure 7.14 – General view of the computational domain
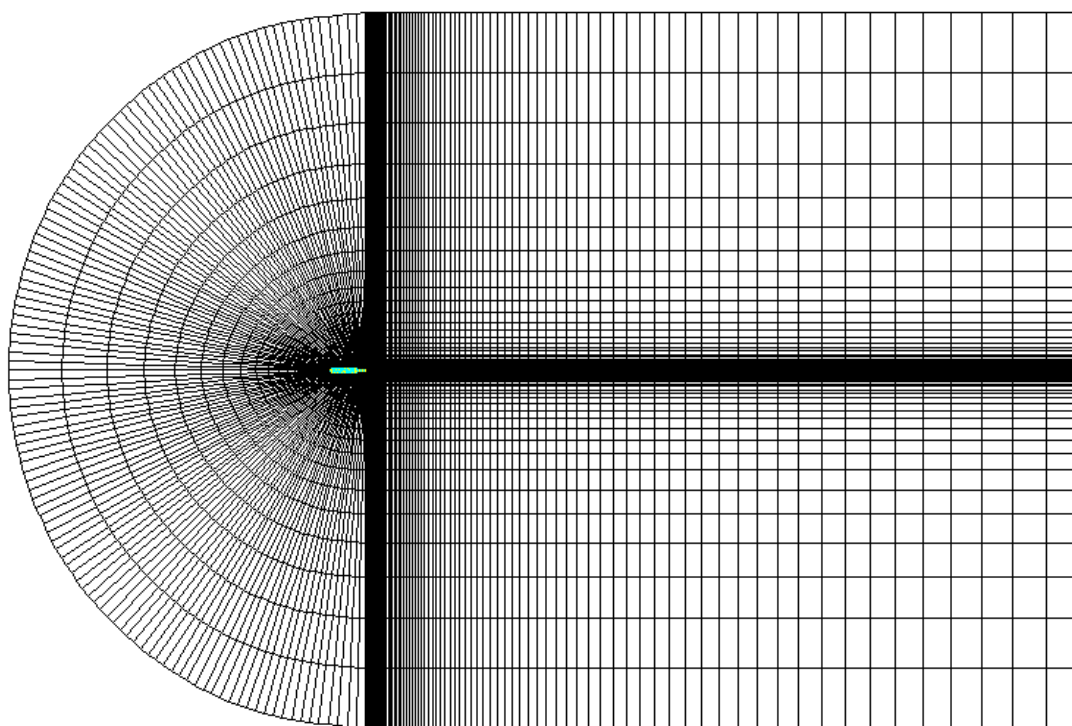
Figure 7.15 – Computational domain as it is seen along Z axis (in spanwise direction)
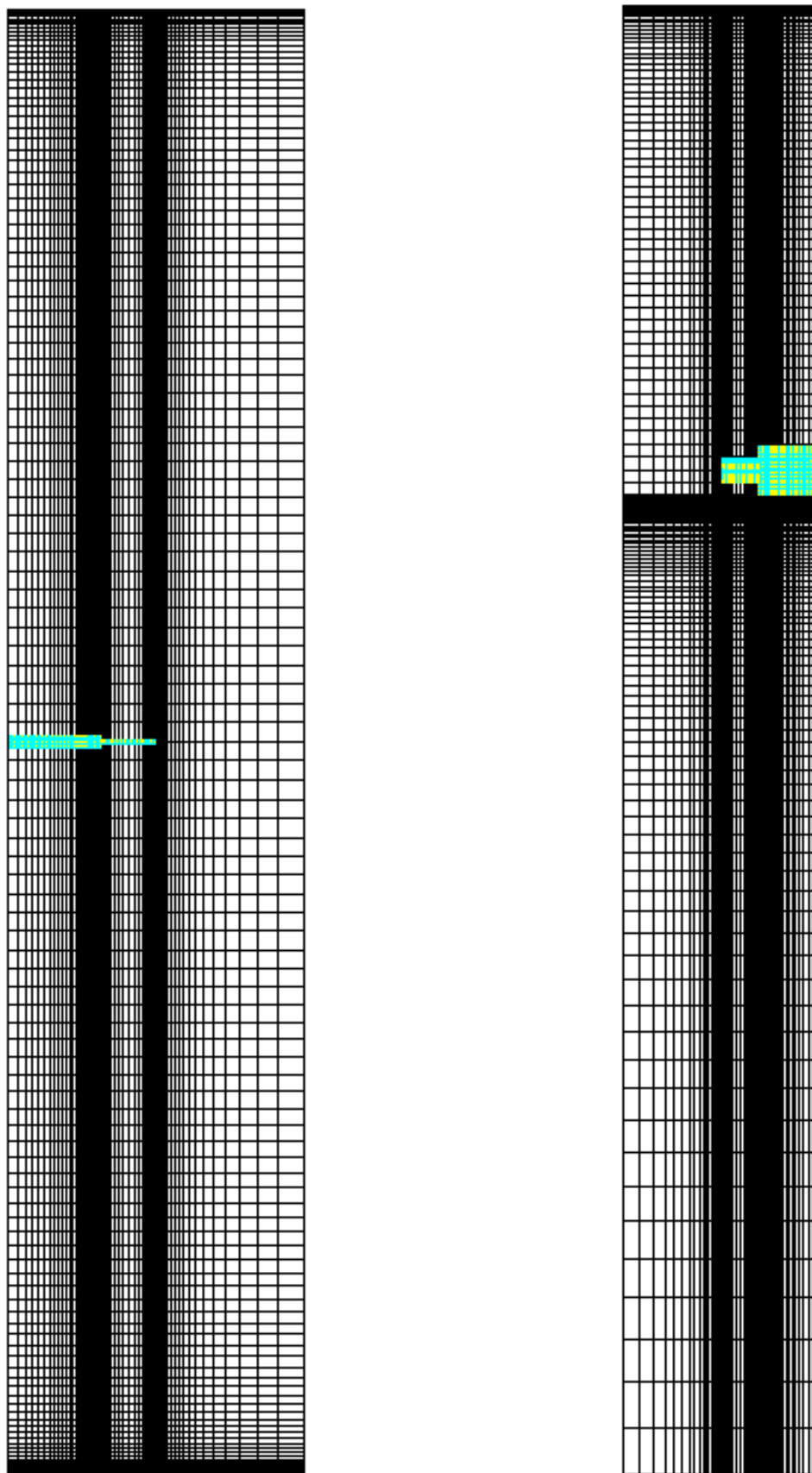
Figure 7.16 – Computational domain as it is seen along *X* axis (forward view)
and *Y* axis (view from above)

Atmospheric pressure of $1 \cdot 10^5$ *Pa* was specified at the outlet boundary. To minimize the influence of the outlet boundary it was considered that pressure distribution is not uniform, but its integral mean value is equal to the prescribed pressure. Zero streamwise gradients were prescribed for turbulence parameters at the outlet.

Symmetry boundary conditions were prescribed for side boundaries, i.e. zero normal flow (along *Z*-axis for this case).

No-slip condition was used for wing surface, i.e. all components of the velocity are equal to zero.

A well-known "k-ε RNG" turbulence model in combination with non-equilibrium wall function, accounting for streamwise pressure gradient influence at the velocity profile in the boundary layer, was used for simulations.

All simulations were run as steady state, using second-order-accurate differencing schemes for all flow parameters.

The results of the simulations were used for plotting of pressure coefficient distribution which are shown at figures 7.17-7.22.
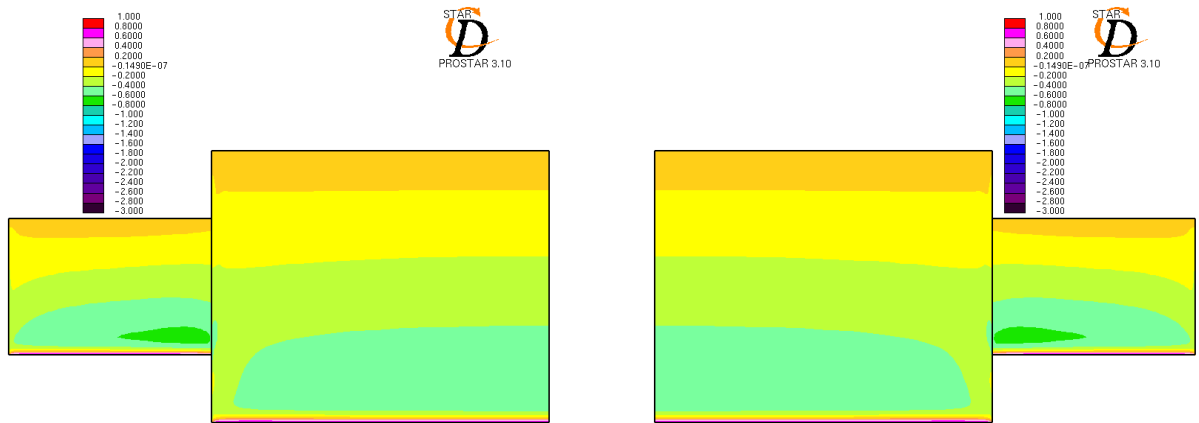
Figure 7.17 – Pressure coefficient distribution for lower and upper surface of the telescope wing, α = 0°
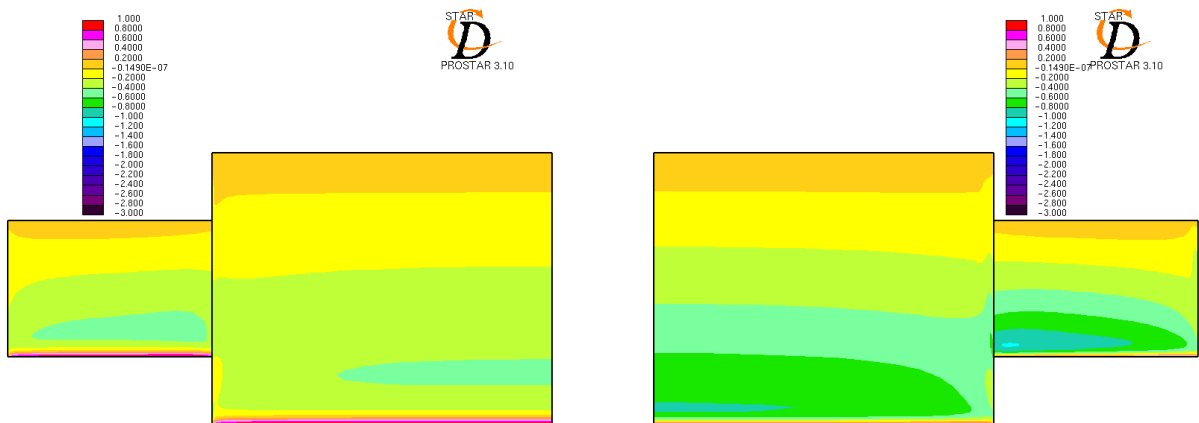
Figure 7.18 – Pressure coefficient distribution for lower and upper surface of the telescope wing, α = 2°
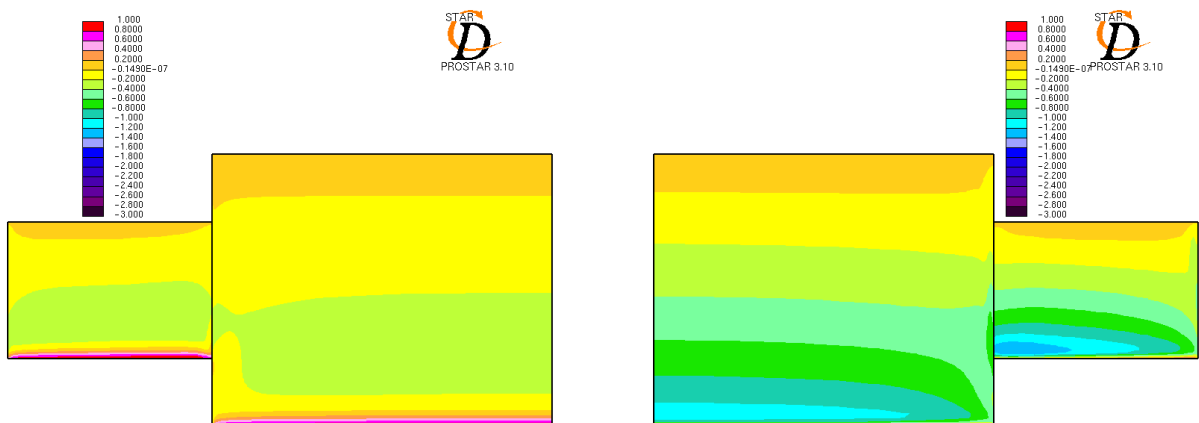
Figure 7.19 – Pressure coefficient distribution for lower and upper surface of the telescope wing, α = 4°
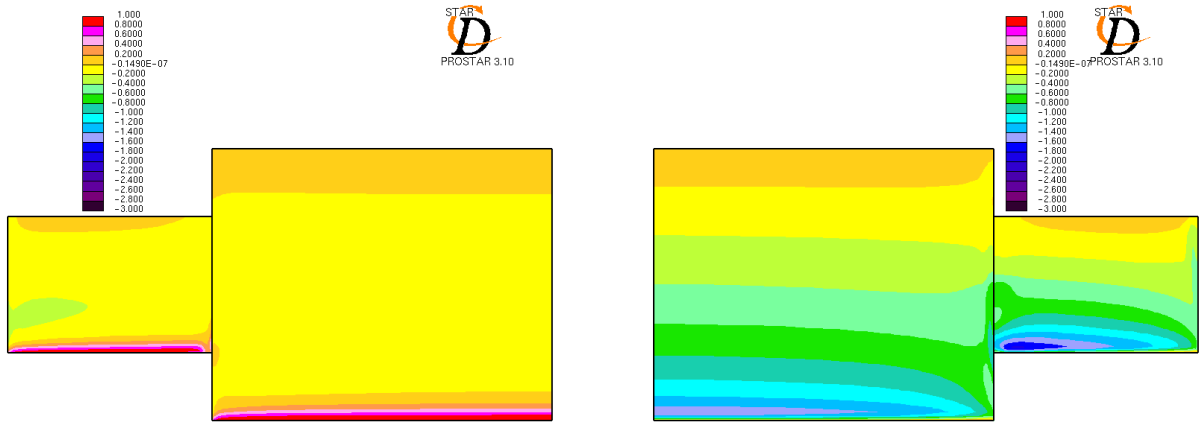
Figure 7.20 – Pressure coefficient distribution for lower and upper surface of the telescope wing, α = 6°
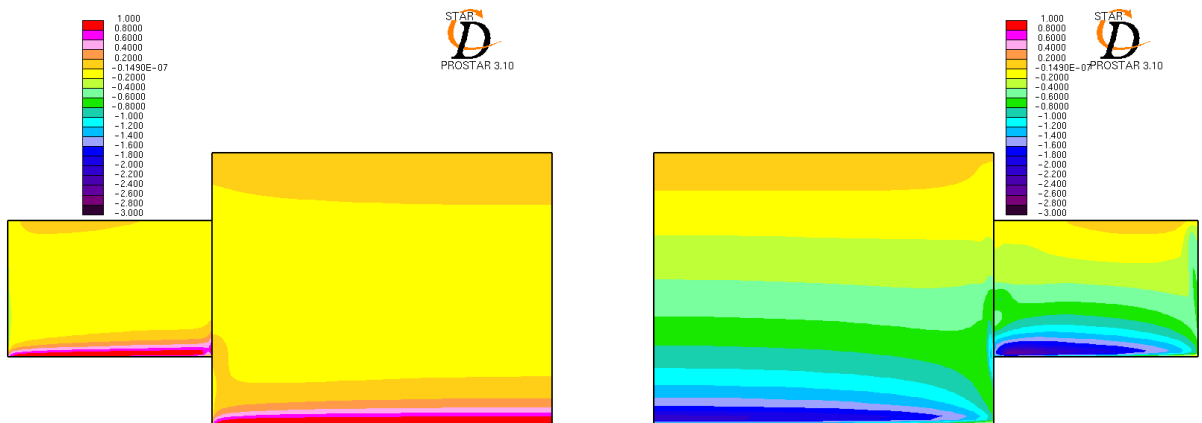
Figure 7.21 – Pressure coefficient distribution for lower and upper surface of the telescope wing, α = 8°
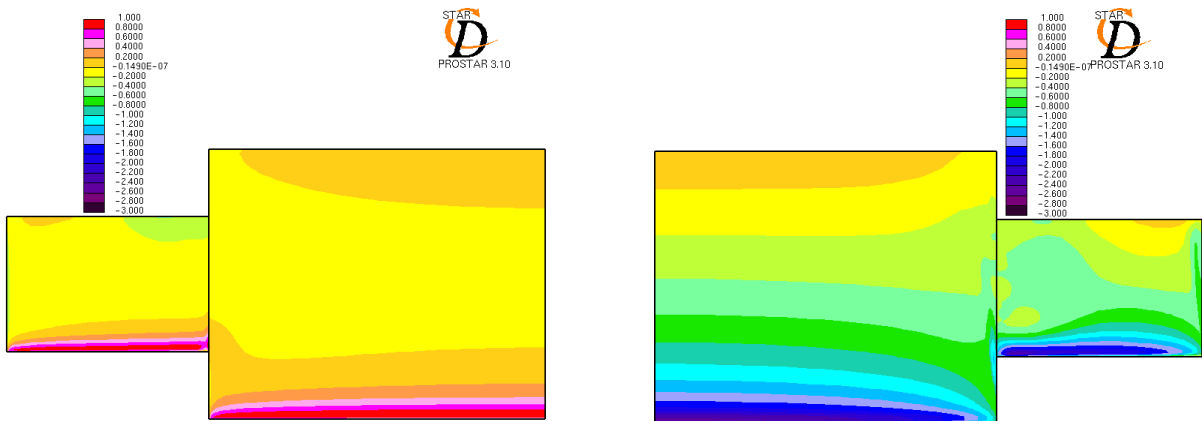
Figure 7.22 – Pressure coefficient distribution for lower and upper surface of the telescope wing, α = 10°

Figures 7.23 and 7.24 show flow pattern at the joint between two parts of the telescope wing for α = 0° and α = 10°. It can be seen from figure 7.24, that for α = 10° the flow is very complicated, with multiple separations and recirculations.
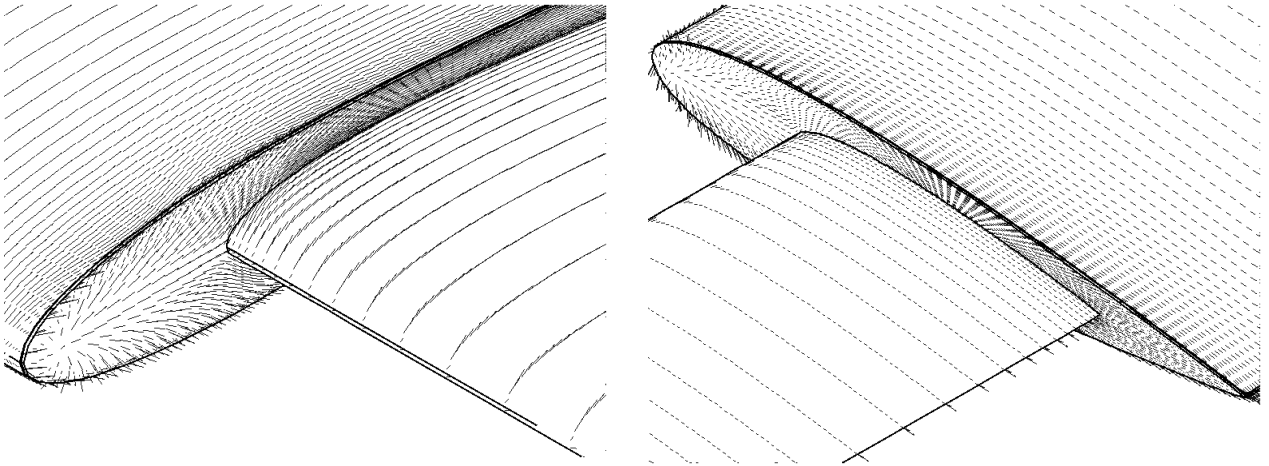
Figure 7.23 – Flow pattern at the joint between two parts of the telescope wing, $\alpha = 0°$
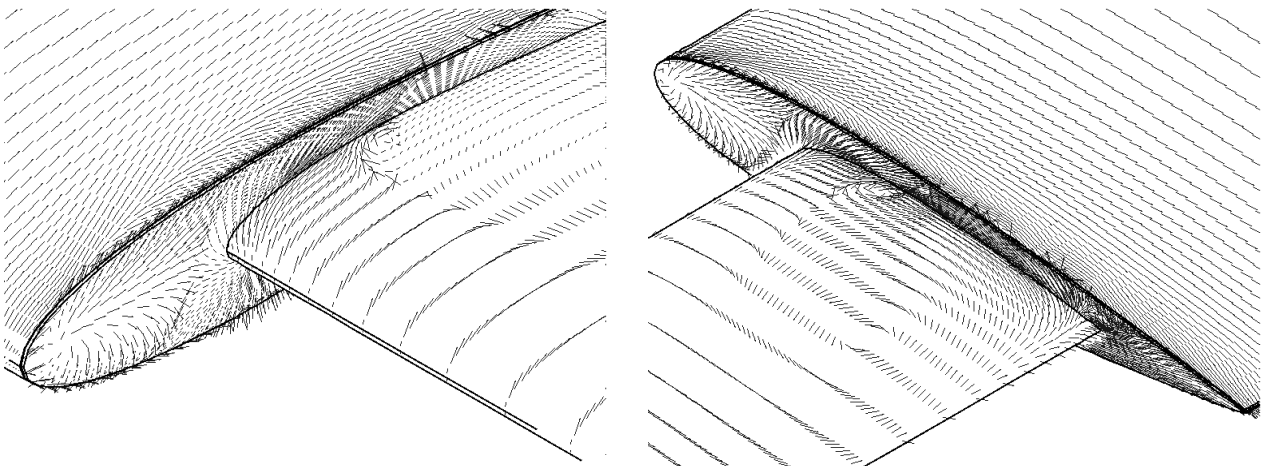
Figure 7.24 – Flow pattern at the joint between two parts of the telescope wing, $\alpha = 10°$

By integration of pressure distribution, spanwise circulation distributions, shown at figure 7.25, were obtained. Local increase in circulation at the joint between two parts of the wing can be explained by suction at the upper wing surface, caused by vortex system forming at the joint. Local increase of circulation at the wing tip is caused by suction in the tip vortex core.
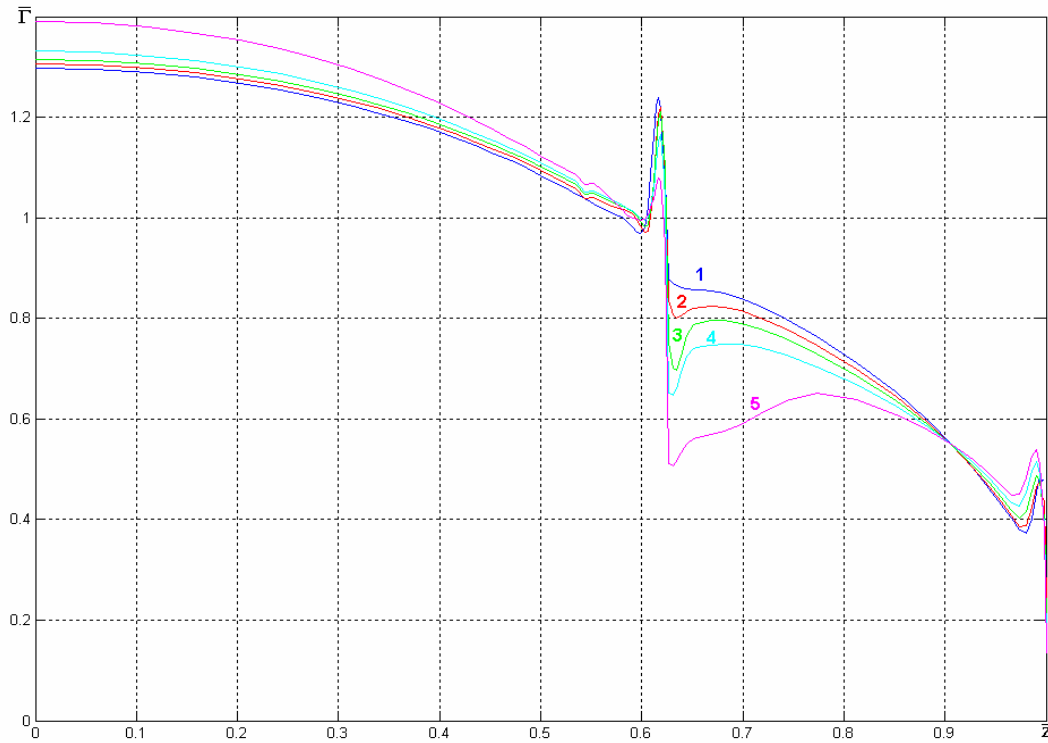
Figure 7.25 – Spanwise distribution of dimensionless circulation for
the telescope wing at different angles of attack:
1 - $\alpha = 2°$, 2 - $\alpha = 4°$, 3 - $\alpha = 6°$, 4 - $\alpha = 8°$, 5 - $\alpha = 10°$

Aerodynamic performance was also estimated from the results of simulations
– lift coefficient C_L vs. angle of attack (shown at figure 7.26) and drag coefficient C_D
vs. angle of attack (shown at figure 7.27). Figure 7.28 shows lift-to-drag ratio C_L/C_D
vs. angle of attack, and figure 7.29 – drag polar, i.e. C_L vs. C_D. It can be seen that for
this range of angle of attack the lift coefficient increases nearly linear with the angle
of attack. Maximum lift-to-drag ratio for this Reynolds number is achieved at $\alpha =$
8°. Drag due to lift factor K is about 0,068.
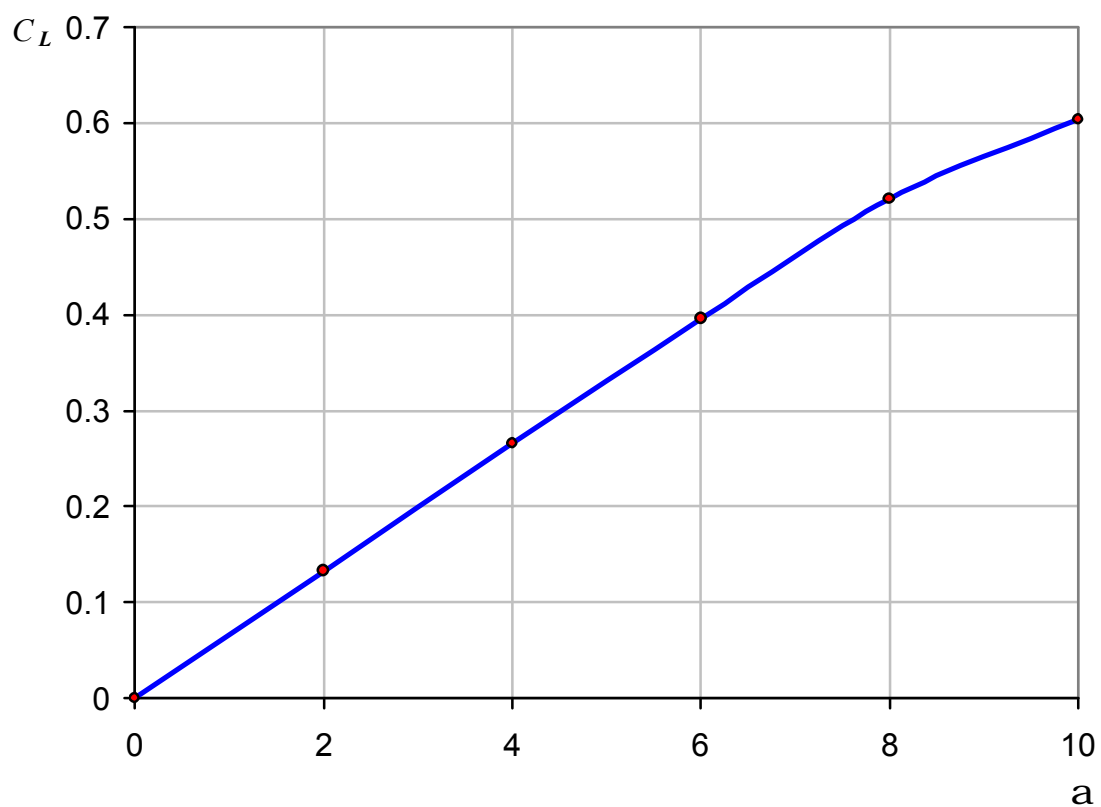
Figure 7.26 – Lift coefficient vs. angle of attack
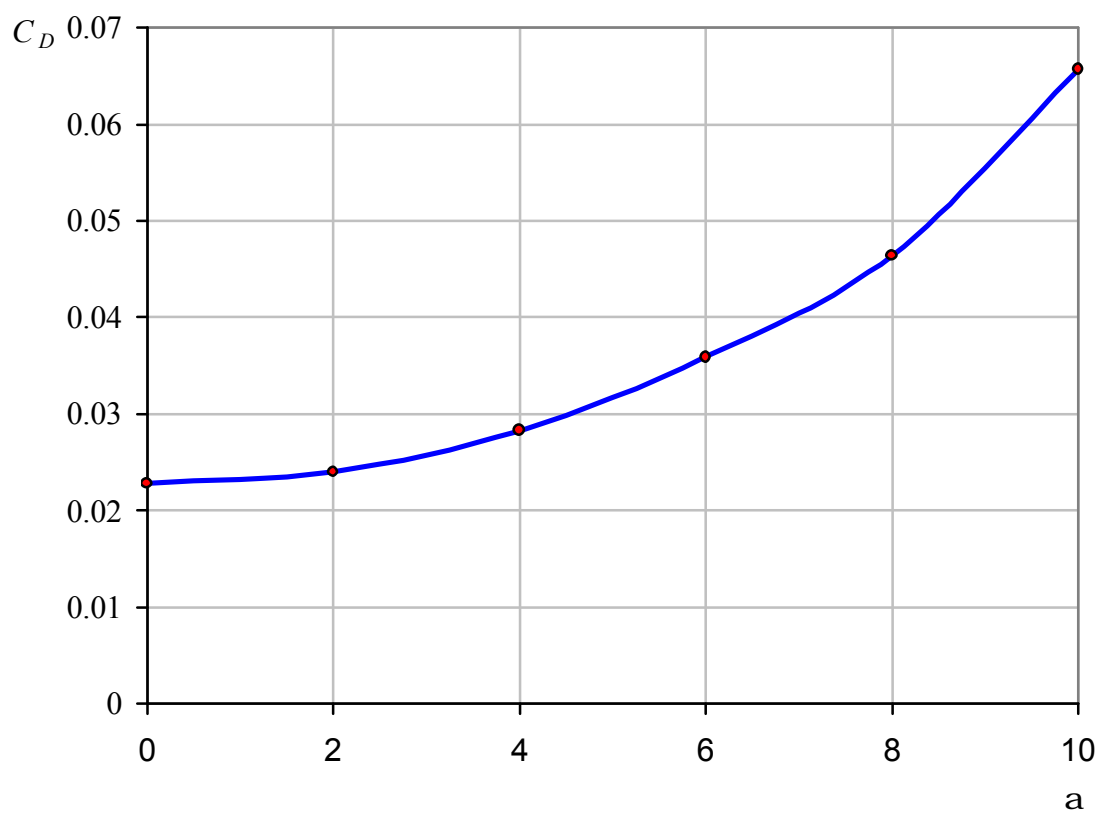
Figure 7.27 – Drag coefficient vs. angle of attack
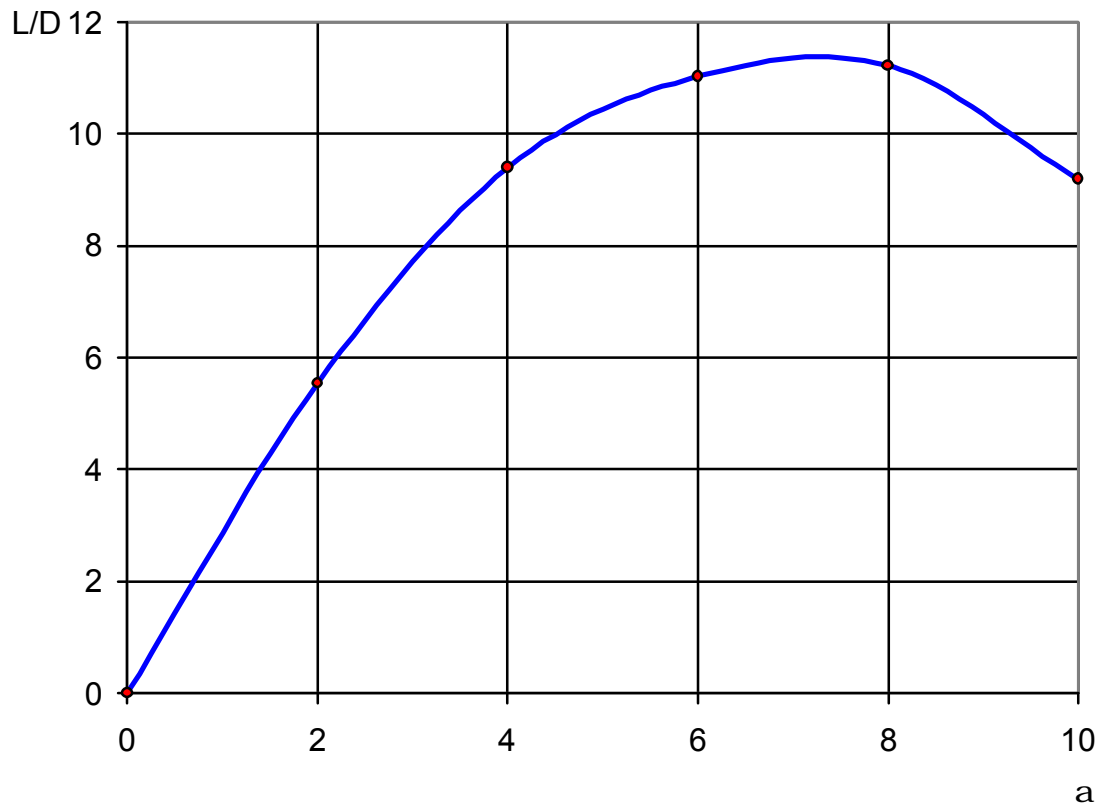
Figure 7.28 – Lift-to-drag ratio vs. angle of attack
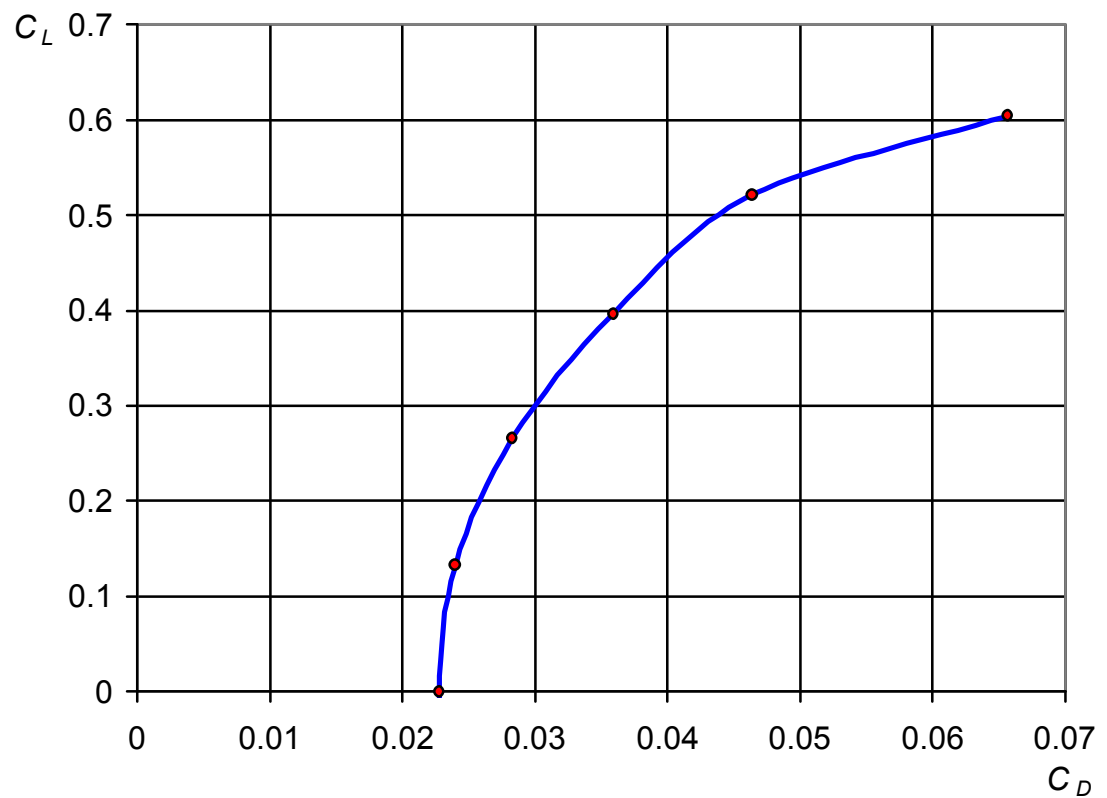
Figure 7.29 – Drag polar

Figure 7.30 presents comparison of different calculations for the telescope wing. Spanwise circulation distribution was calculated with Star-CD ($\alpha = 2°$) and with discrete vortex method, linear and non-linear ($\alpha = 2°$) variant. A good general agreement can be seen. The main difference is near the joint between two parts of the wing. Star-CD results show sharp increase in circulation, while linear discrete vortex method give quite a small "junk". Non-linear discrete vortex method overestimates circulation for the main part of the wing comparing with two other computational models.
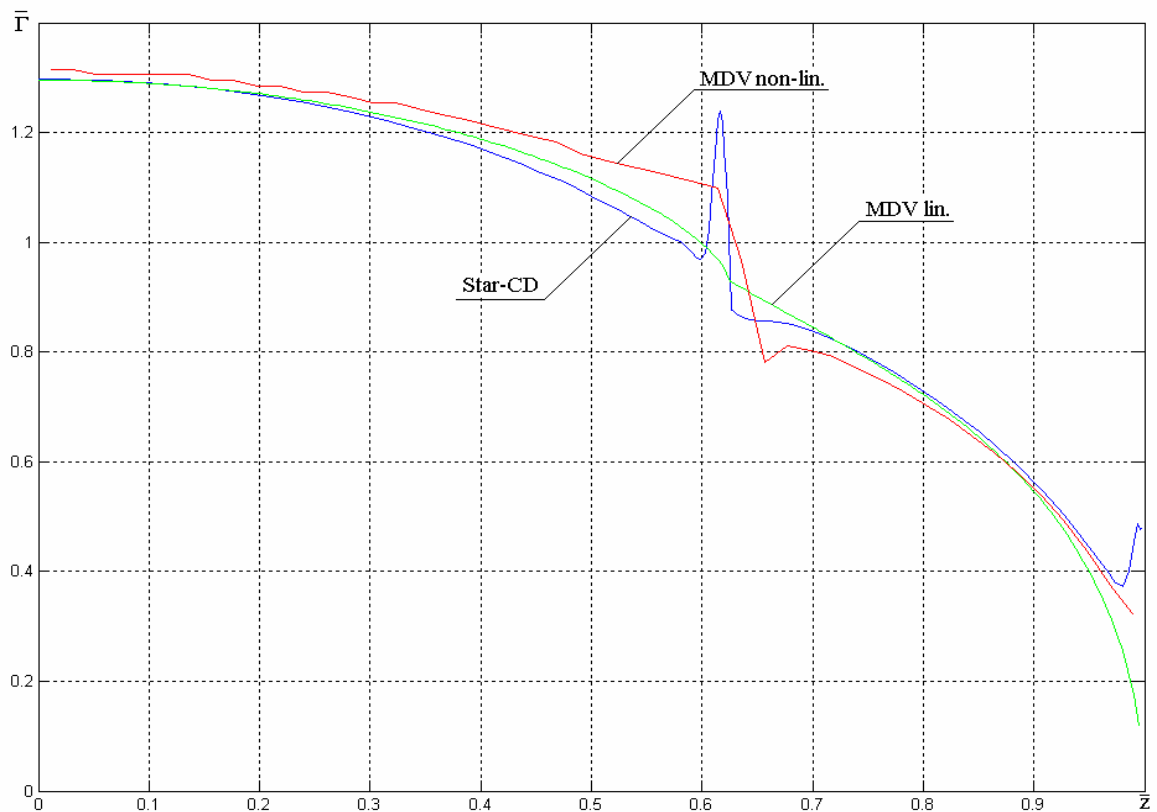
Figure 7.30 – Spanwise distribution of dimensionless circulation for the telescope wing

Figures 7.31 – 7.36 present chord plots of the pressure coefficient for seven test sections, for which the measurements were performed in the wind-tunnel tests. Note that for the Section 4 (located at the main part of the wing near the joint) pressure distribution is sufficiently different from the other sections. This is probably explained by the influence of local separation zones, which are visible from figures 7.23 and 7.24.

Section 1

Section 2

Section 3

Section 4

Section 5

Section 6

Section 7
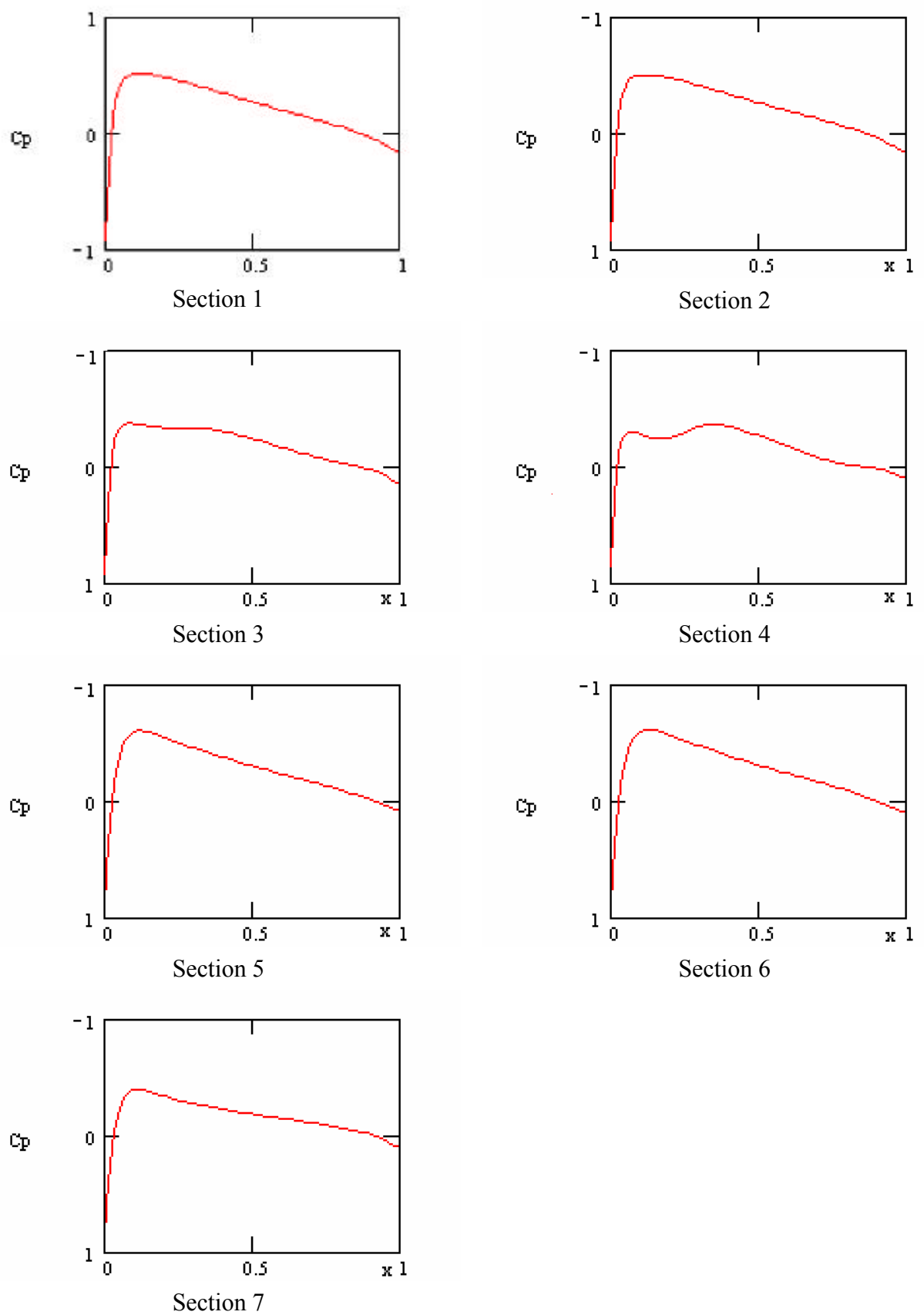
Figure 7.31 – Simulation results for $\alpha = 0°$

Section 1

Section 2

Section 3

Section 4

Section 5

Section 6

Section 7
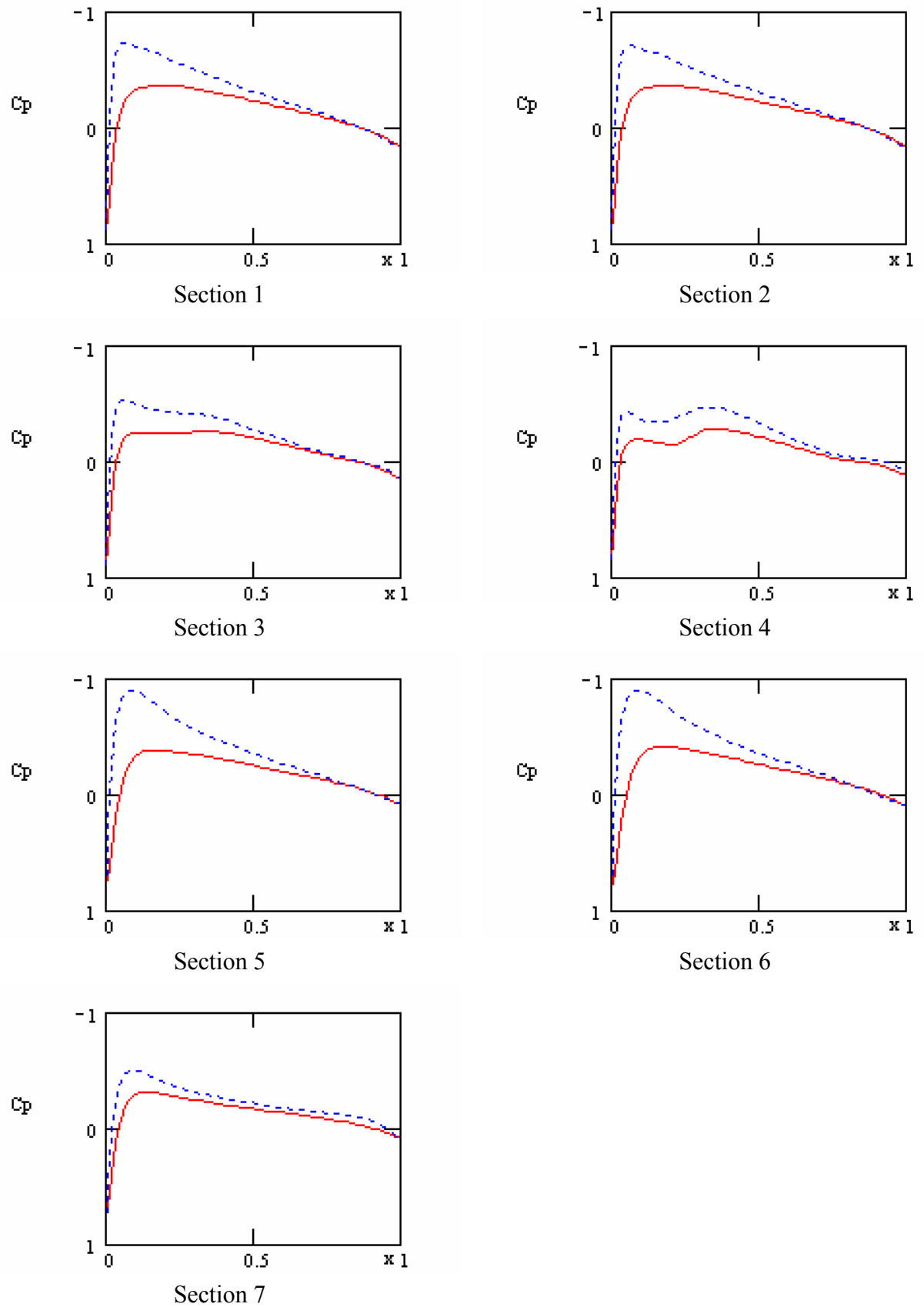
Figure 7.32 – Simulation results for $\alpha = 2^{\circ}$

Section 1

Section 2

Section 3

Section 4

Section 5

Section 6

Section 7
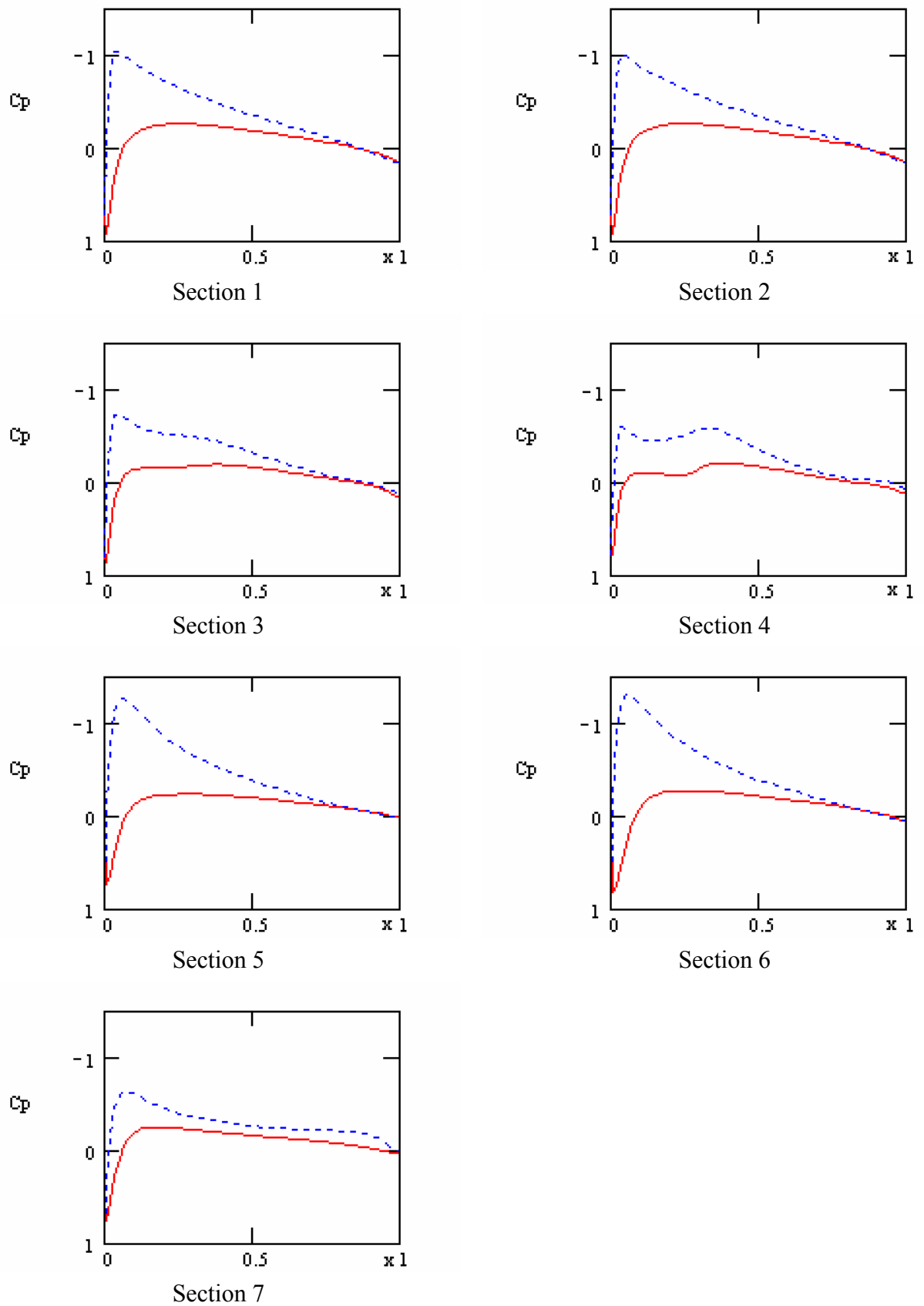
Figure 7.33 – Simulation results for $\alpha = 4°$

Section 1

Section 2

Section 3

Section 4

Section 5

Section 6

Section 7
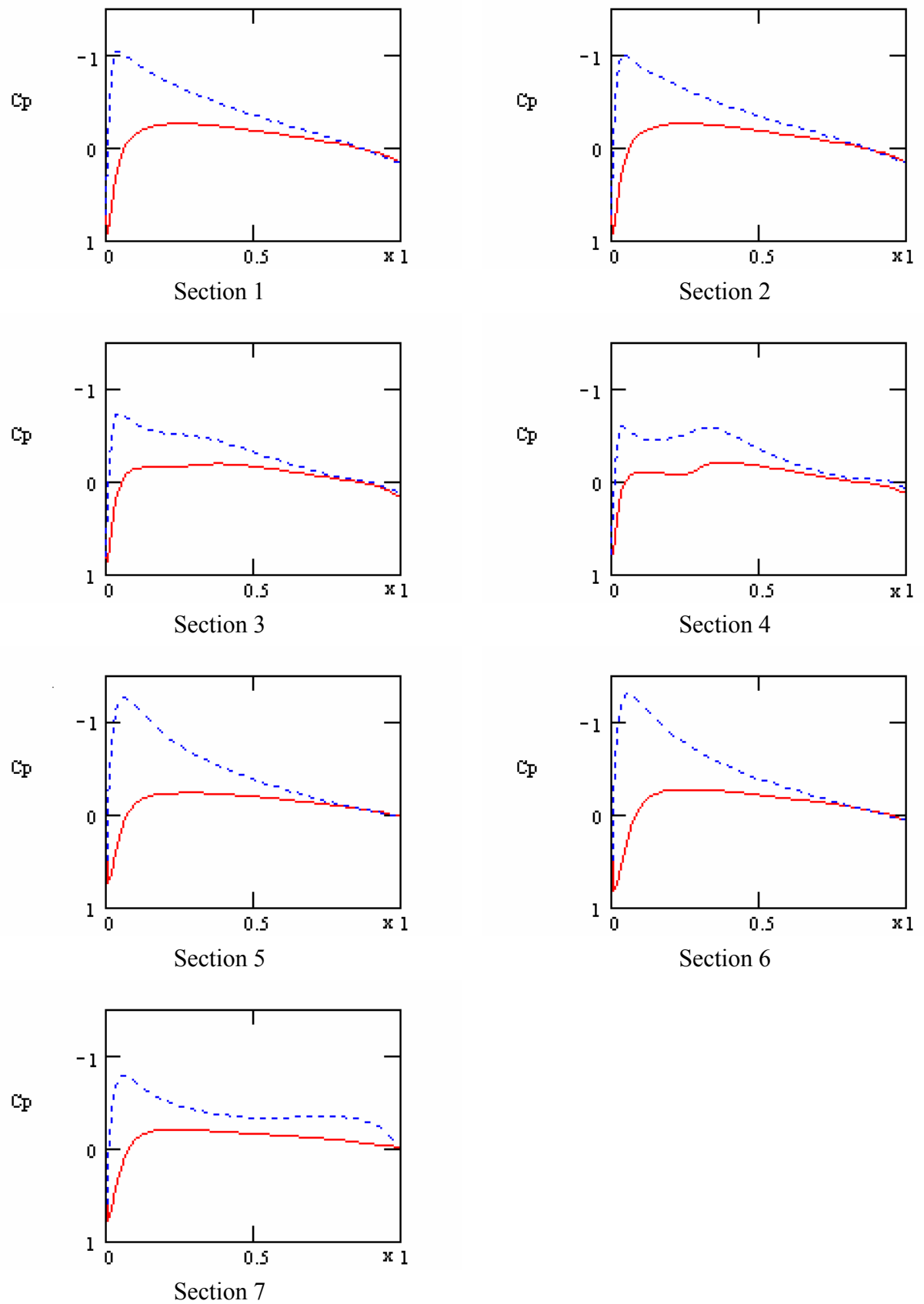
Figure 7.34 – Simulation results for $\alpha = 6°$

Section 1

Section 2

Section 3

Section 4

Section 5

Section 6

Section 7
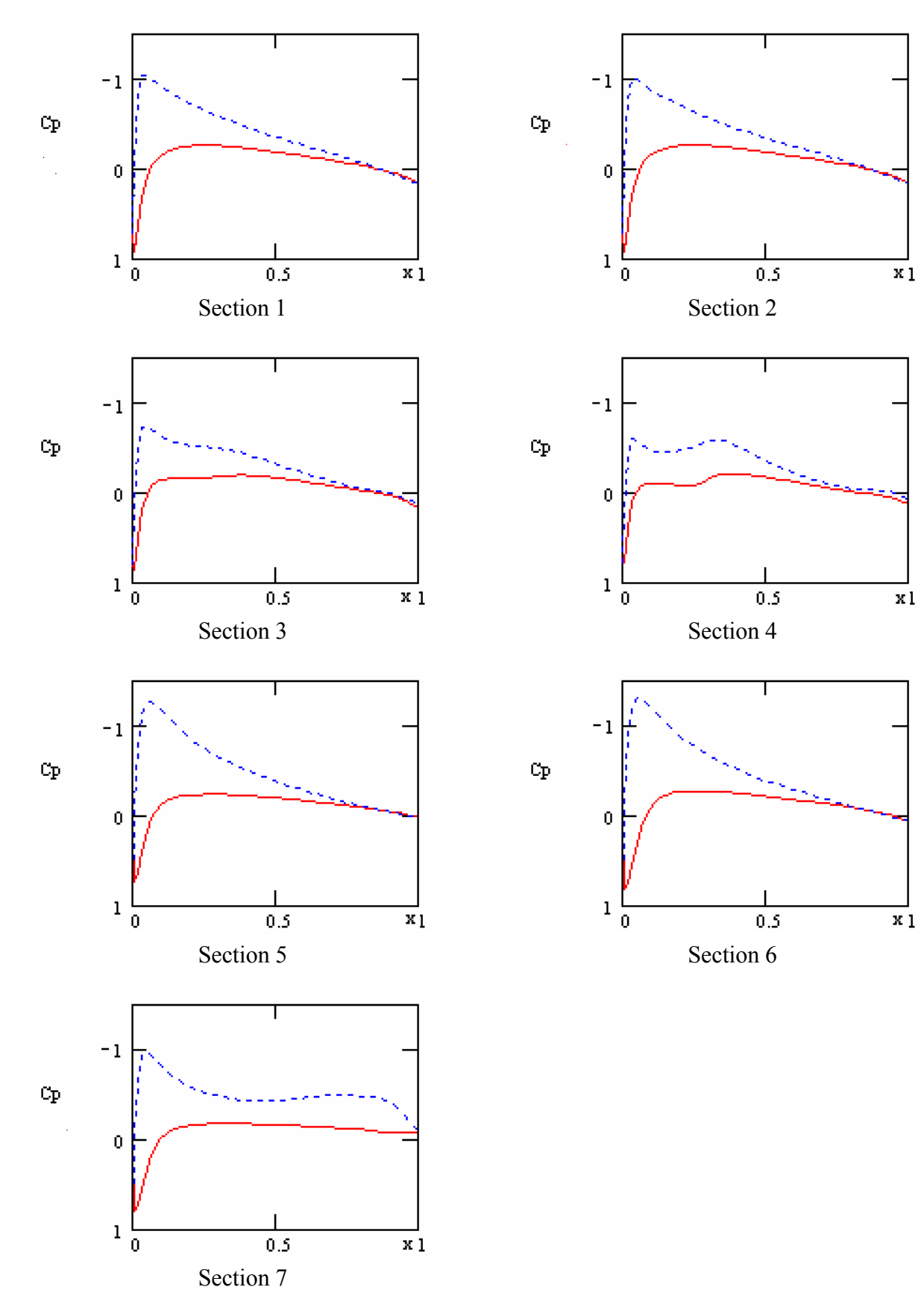
Figure 7.35 – Simulation results for $\alpha = 8°$

Section 1

Section 2

Section 3

Section 4

Section 5

Section 6

Section 7
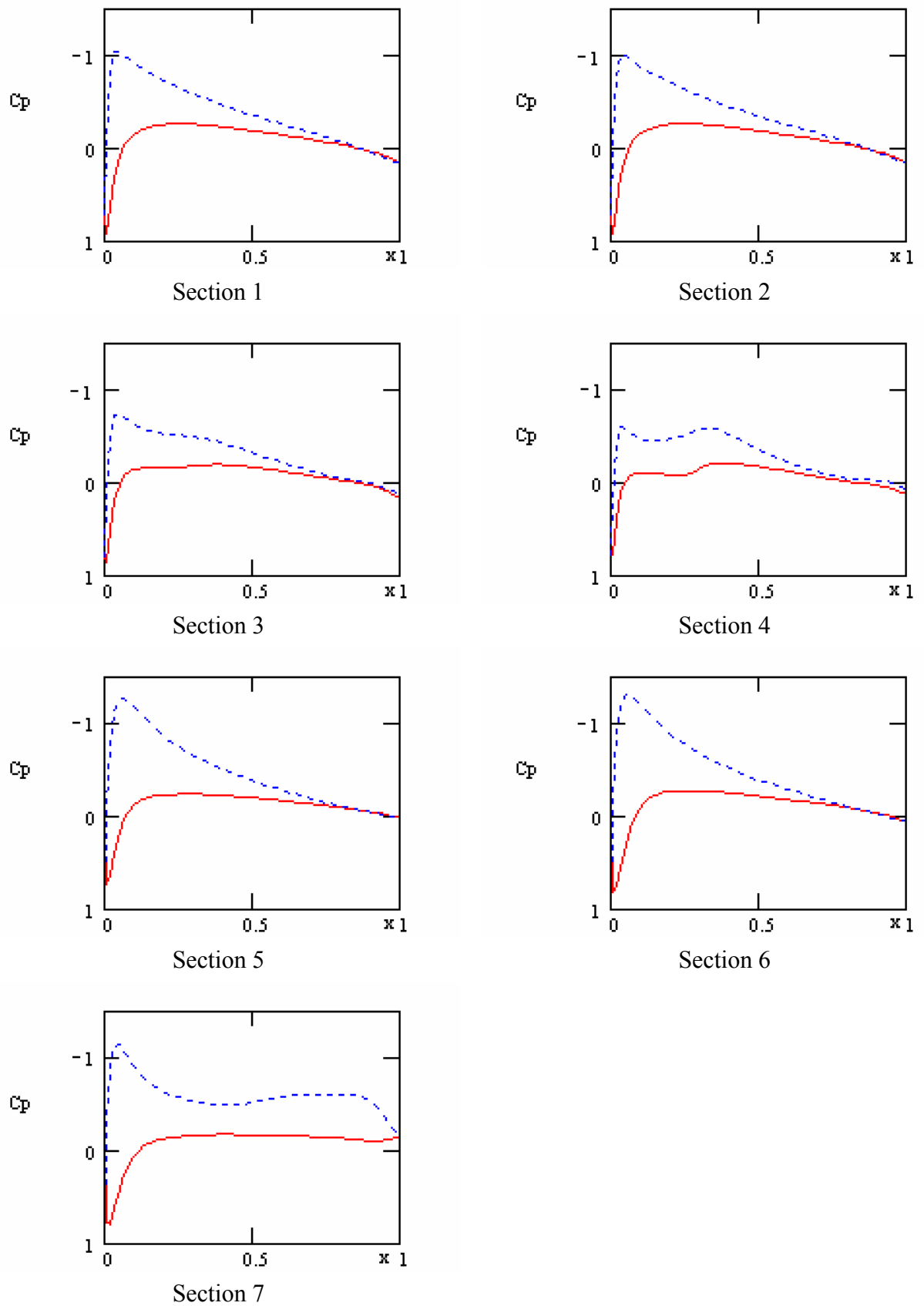
Figure 7.36 – Simulation results for $\alpha = 10°$

8 Experimental research
of telescope wing aerodynamics

8.1 Description of test models
for balance tests in the wind-tunnel

In order to analyze aerodynamic performance of the telescope wing a number of test models were manufactured. Geometry of the parts of these models presented at figures 8.1 - 8.4.
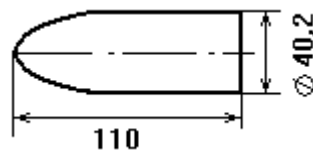
Figure 8.1 – Geometry of the nose part of the model fuselage
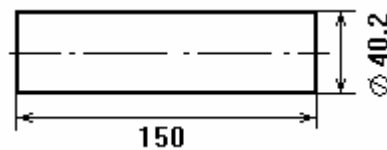
Figure 8.2 – Geometry of the main part of the model fuselage ("clean fuselage" variant)
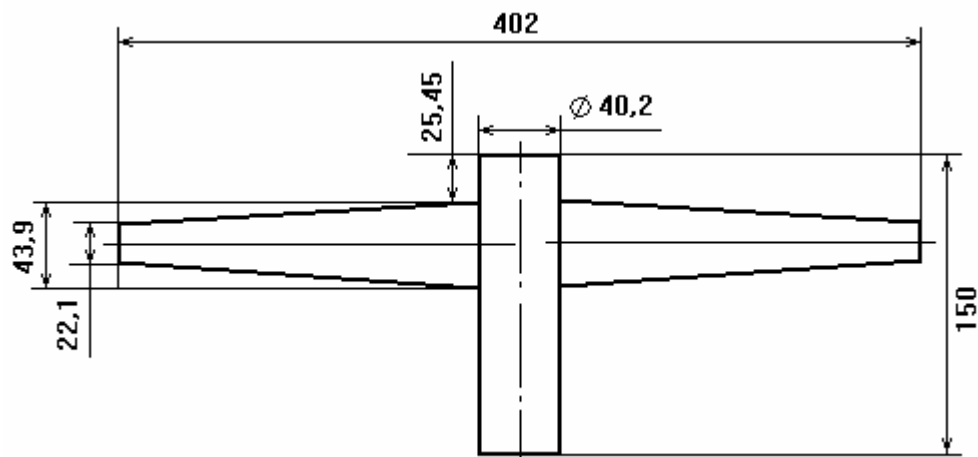
Figure 8.3 – Geometry of the main part of the winged model
("trapezoidal wing-fuselage" variant)
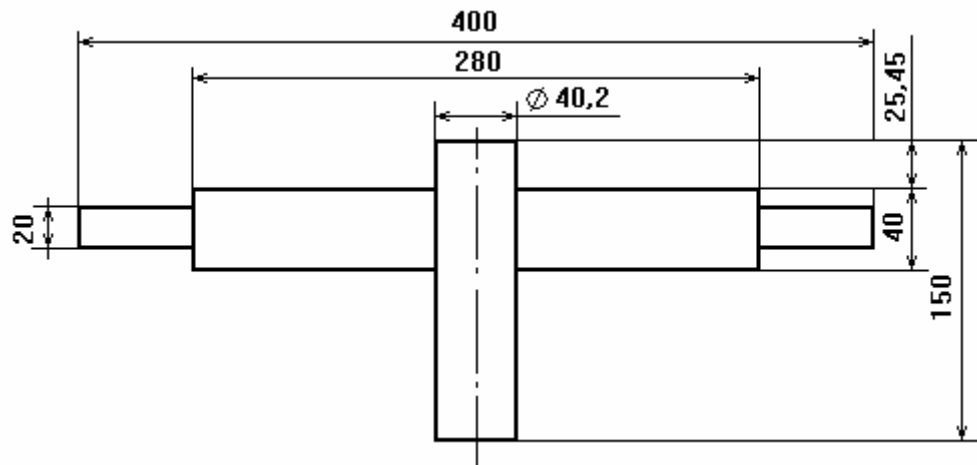
Figure 8.4 – Geometry of the main part of the winged model
("telescope wing-fuselage" variant)

Photos of the model elements are shown at figures 8.5 - 8.8.

Figure 8.5 – Nose part of the model fuselage
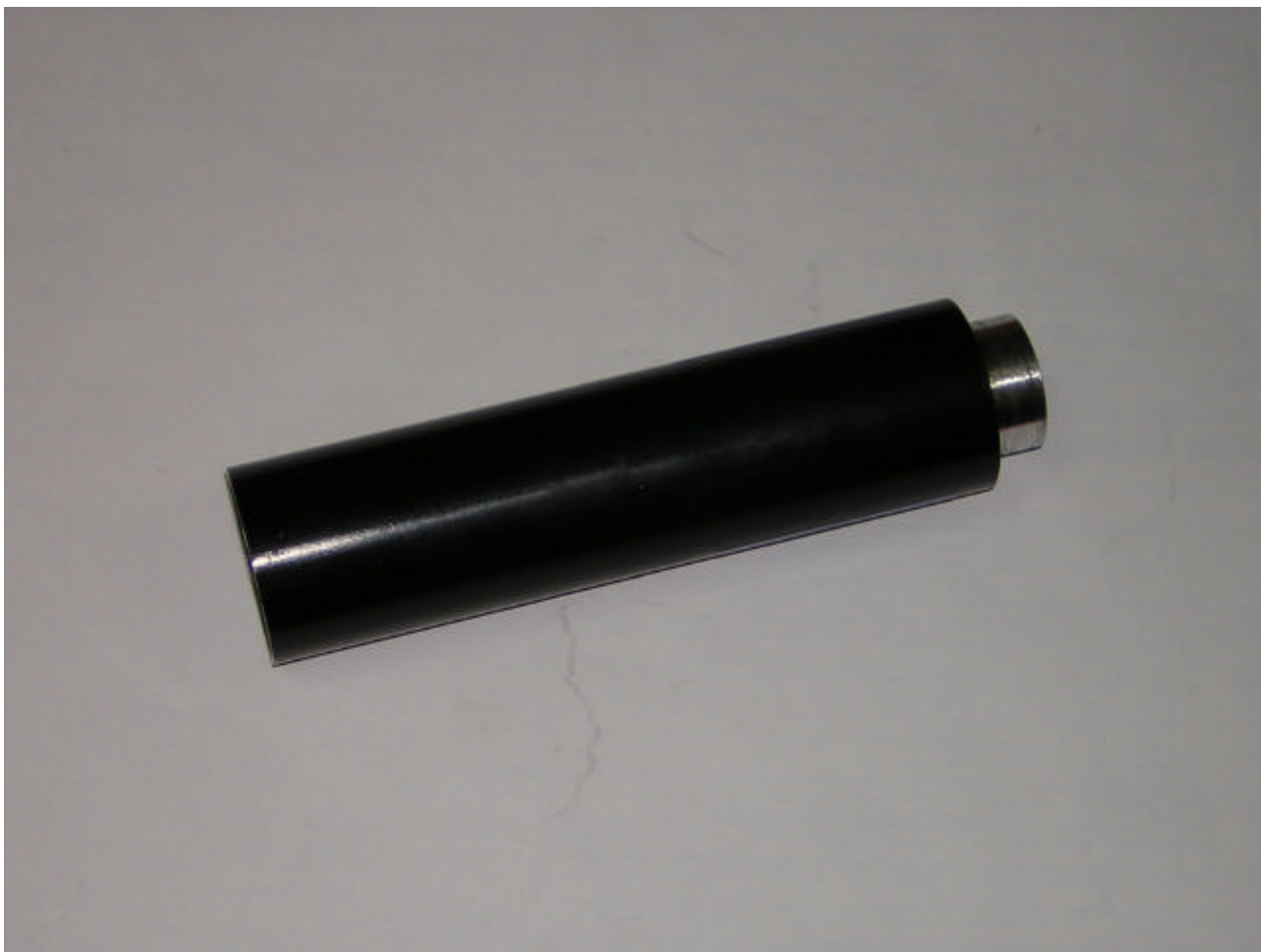
Figure 8.6 – Main part of the model fuselage ("clean fuselage" variant)

Figure 8.7 – Main part of the winged model ("trapezoidal wing-fuselage" variant)
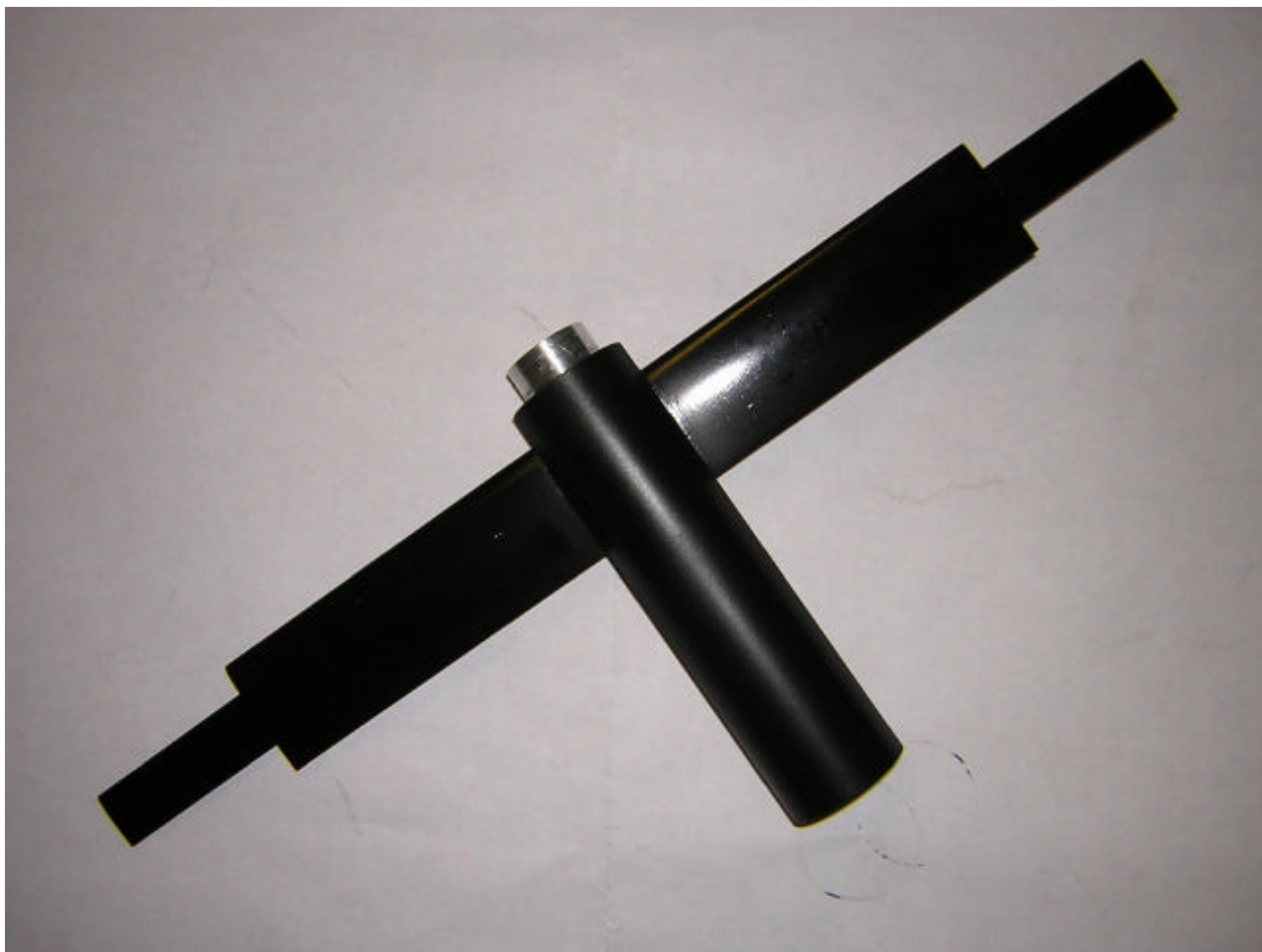
Figure 8.8 – Main part of the winged model ("telescope wing-fuselage" variant)

Experimental program was comprised of tests of "clean" fuselage (figure 8.9), "trapezoidal wing-fuselage" combination (figure 8.10) and "telescope wing-fuselage" combination (figure 8.11).

Figure 8.9 – "Clean" fuselage model

Figure 8.10 – Model of "trapezoidal wing-fuselage" combination

Figure 8.11 – Model of "telescope wing-fuselage" combination

8.2 Results of balance tests

Experimental program involved four-fold measurement for each airspeed (25, 30, 35 and 40 m/s). In order to reduce the influence of the model asymmetry all tests were performed for normal and for inverted (i.e. rotated 180° about the longitudinal axis) position of the model. Thus each model ("clear" fuselage, "trapezoidal wing-fuselage" and "telescope wing-fuselage" combinations) was tested 16 times. Combinations of model position and airspeed were picked up with the help of random number generator.

Experiments were performed with the help of automated system based on T-3 SSAU low-speed wind-tunnel. This wind-tunnel is equipped with inner-model 6-component strain balance. Automated system sustains constant prescribed airspeed during the experiment, controls changes of the angle of attack, acquires data from the strain balance and provides real-time low-level data processing.

Next level of data processing includes corrections eliminating the influence of different collateral factors.

After that the polynomial fits were found with MATLAB software – 5th order for the lift coefficient vs. angle of attack and 6th order for the drag coefficient vs. angle of attack. At figures 8.12 - 8.23 points present experimental data and solid lines are polynomial fits.

Polynomial fits for clean fuselage were subtracted from the polynomial fits for "trapezoidal wing-fuselage" and "telescope wing-fuselage" combinations in order to obtain aerodynamic performance of the "isolated" wings. These data include some effects resulting from the interference between wing and fuselage, so they will be different from performance of "clean" wings. But for the considered two wings (trapezoidal and telescope) such effects are nearly the same, so the aerodynamic performance of "isolated" wing can be used for comparison. Results are shown at figures 8.24 and 8.25. It can be noticed that the influence of the airspeed is rather small.

Figures 8.26 and 8.27 and present drag polars of the "isolated" wings and table 8.1 presents maximum aerodynamic efficiency for these wings. Comparison of the tables 7.2 and 8.1 reveals some difference between calculated and experimental values of maximum aerodynamic efficiency. This can be caused by the effects arising from low Reynolds numbers and from interference between wing and fuselage, which were not accounted in the calculations. But the experiments also approved that aerodynamic efficiency of telescope wing is nearly the same as of the trapezoidal wing.

Table 8.1 – Experimental values of maximum aerodynamic efficiency

| Airspeed, m/s	25	30	35	40
Telescope wing	15.3	17.0	17.8	19.6
Trapezoidal wing	14.7	16.4	17.8	20.3
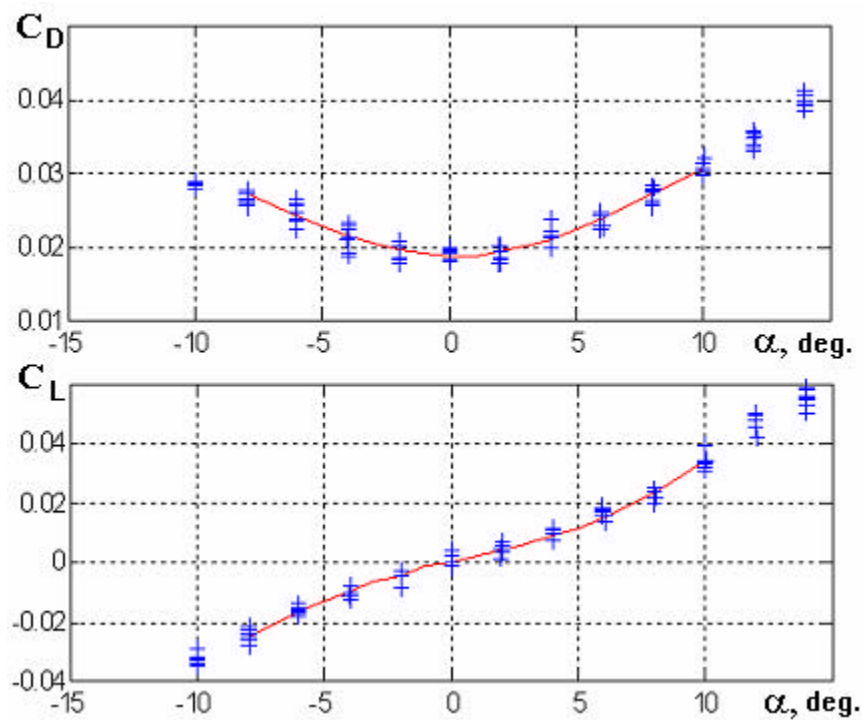
Figure 8.12 – Experimental data and polynomial fit for "clean" fuselage (V=25 m/s)
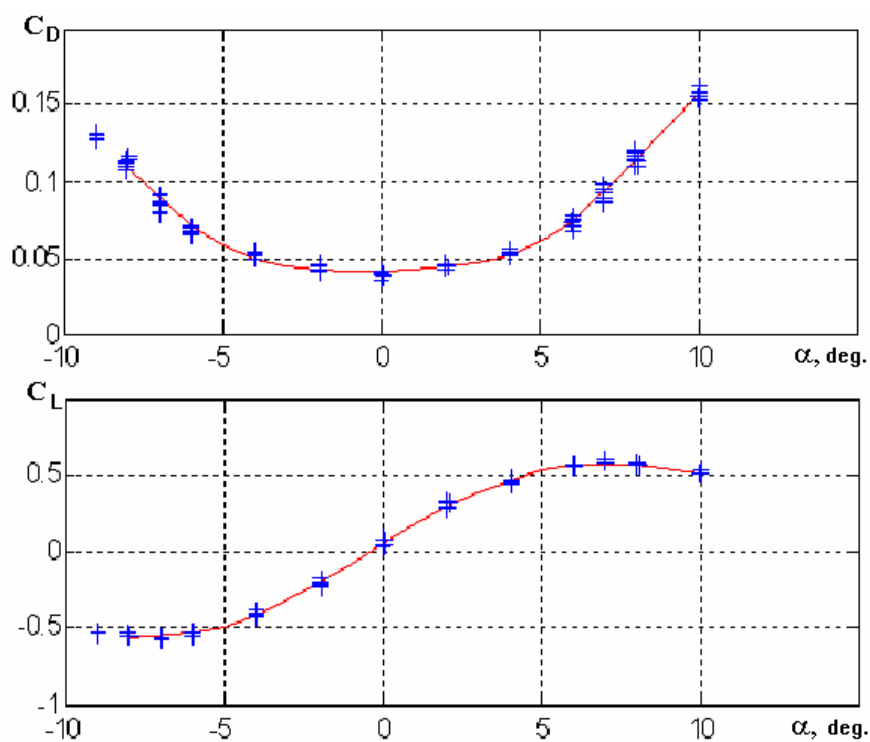
Figure 8.13 – Experimental data and polynomial fit for "telescope wing-fuselage" combination (V=25 m/s)
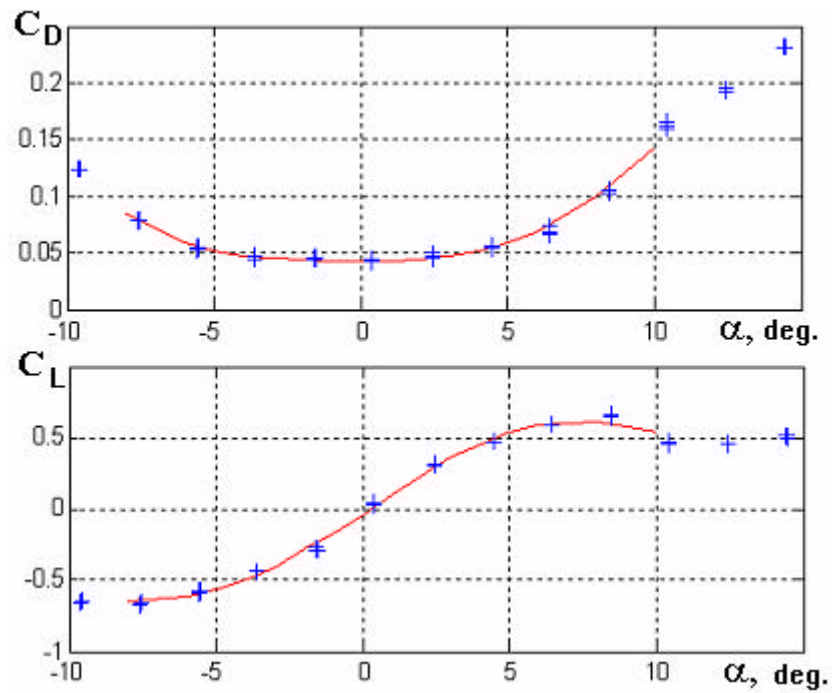
Figure 8.14 – Experimental data and polynomial fit for "trapezoidal wing-fuselage" combination (V=25 m/s)
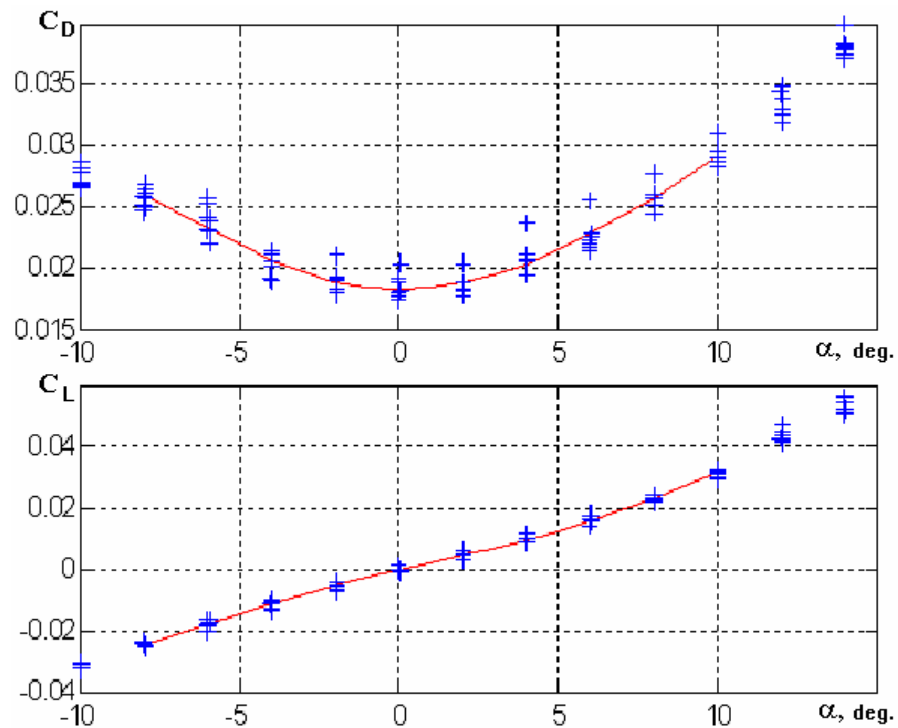
Figure 8.15 – Experimental data and polynomial fit for "clean" fuselage (V=30 m/s)
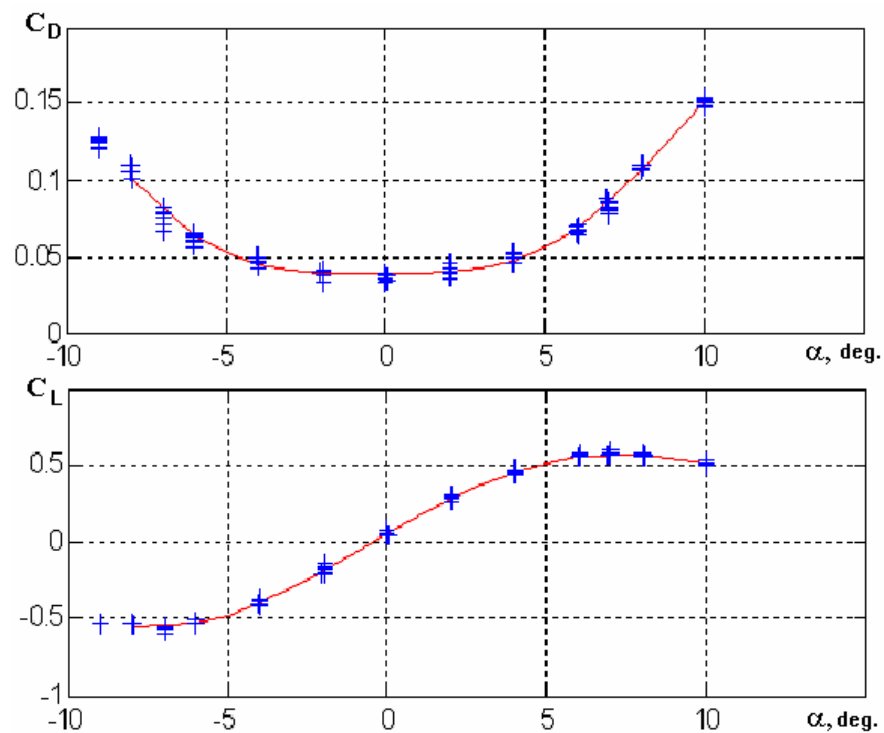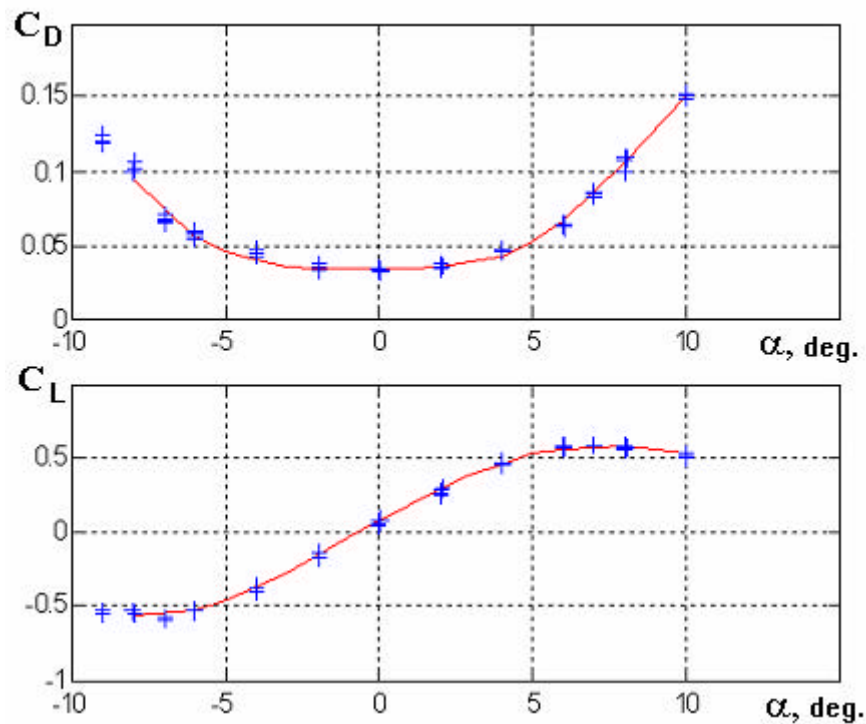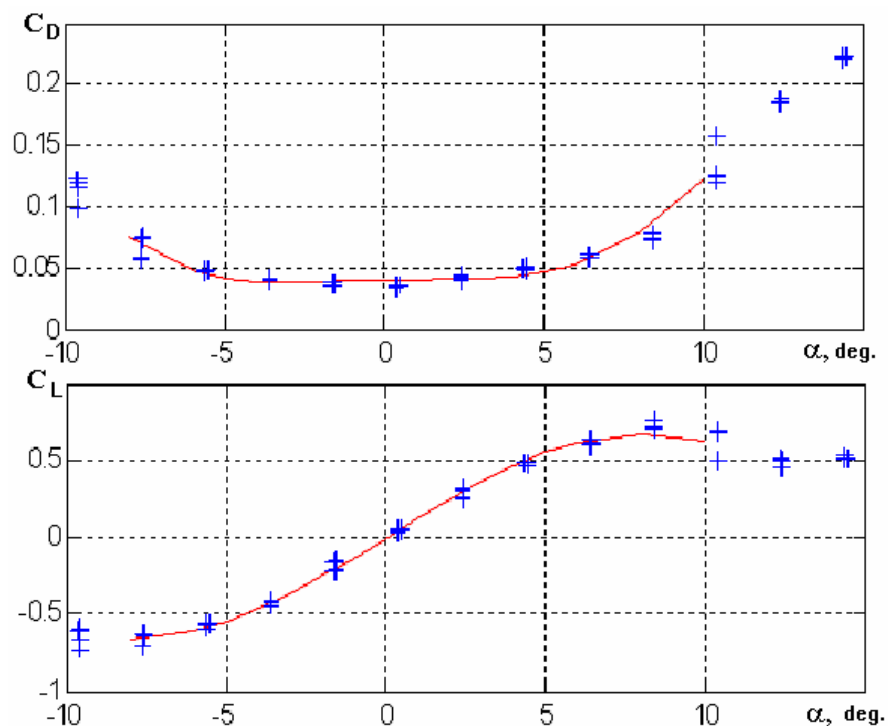
Figure 8.16 – Experimental data and polynomial fit for "telescope wing-fuselage" combination (V=30 m/s)
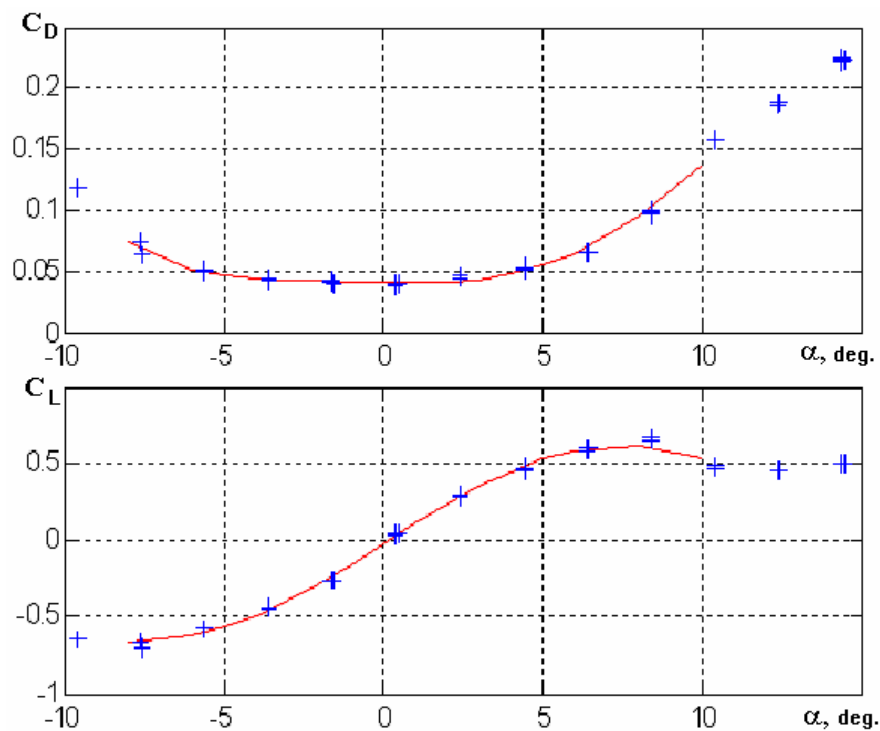
Figure 8.17 – Experimental data and polynomial fit for "trapezoidal wing-fuselage" combination (V=30 m/s)
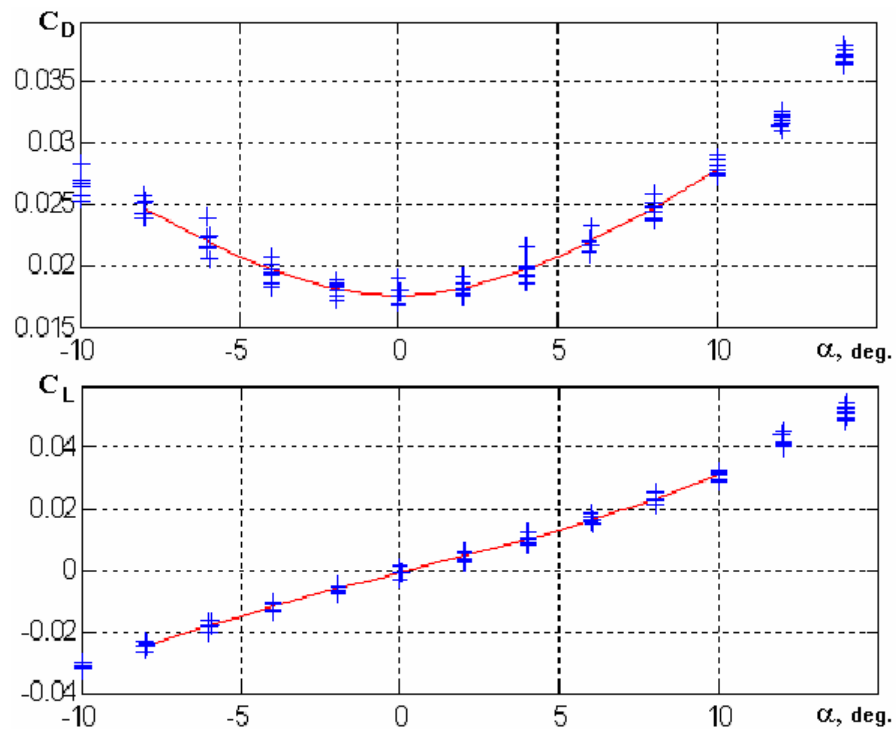
Figure 8.18 – Experimental data and polynomial fit for "clean" fuselage (V=35 m/s)
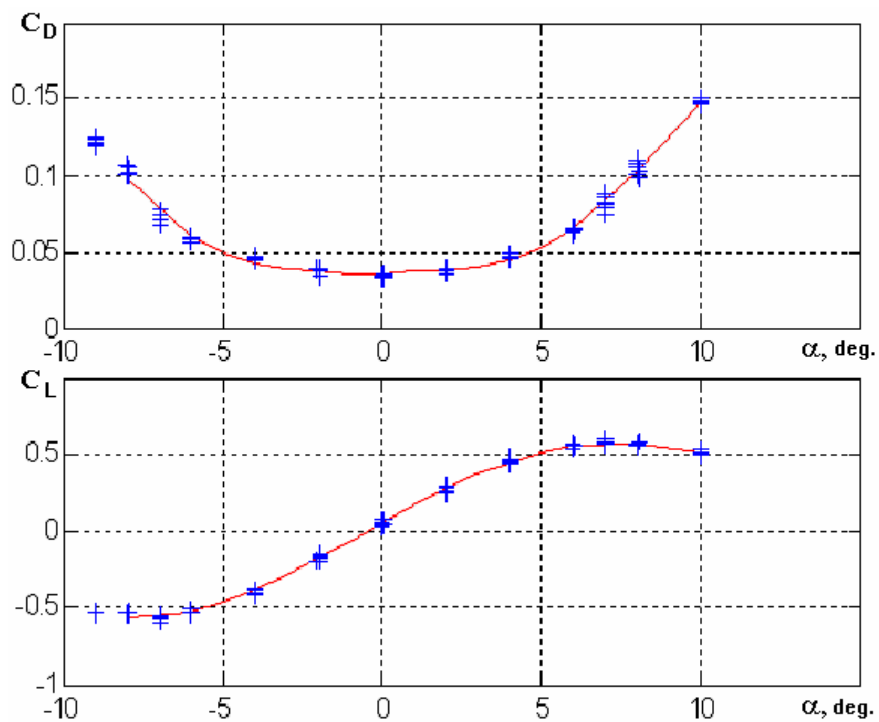
Figure 8.19 – Experimental data and polynomial fit for "telescope wing-fuselage" combination (V=35 m/s)
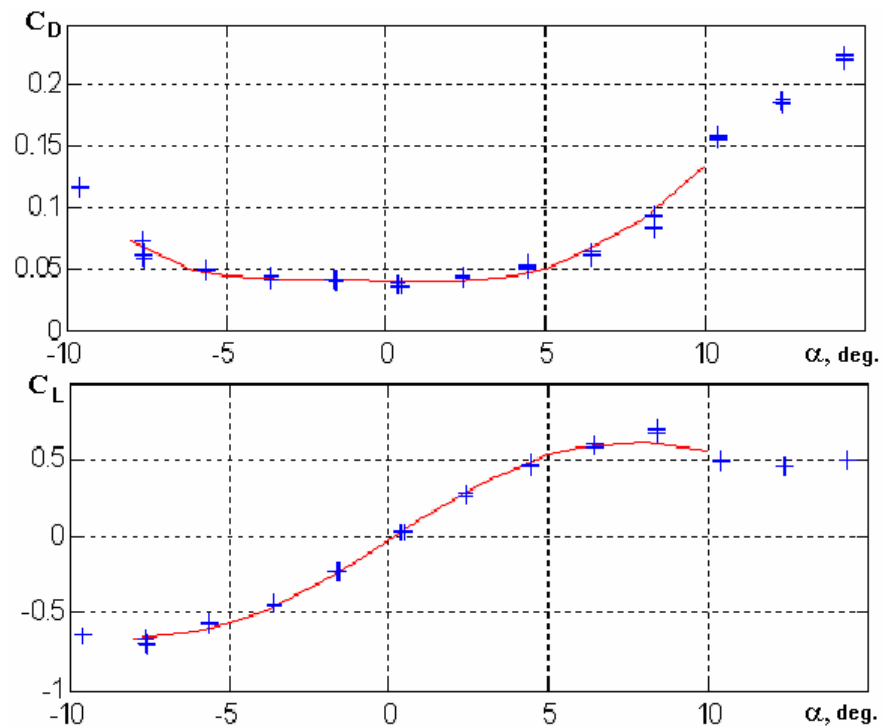
Figure 8.20 – Experimental data and polynomial fit for "trapezoidal wing-fuselage" combination (V=35 m/s)
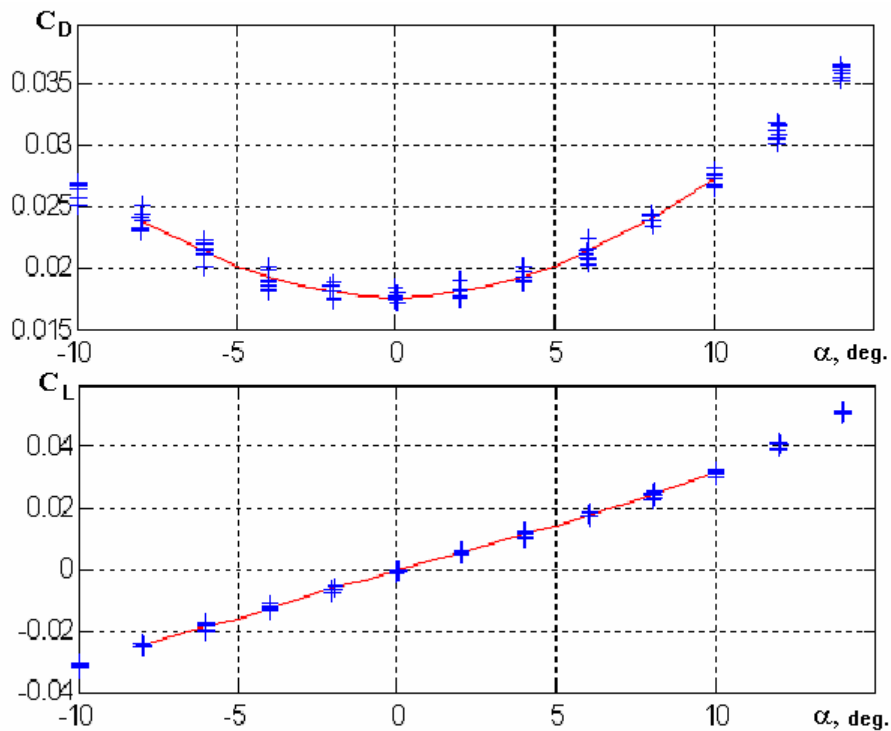
Figure 8.21 – Experimental data and polynomial fit for "clean" fuselage (V=40 m/s)

Figure 8.22 – Experimental data and polynomial fit for "telescope wing-fuselage" combination (V=40 m/s)

Figure 8.23 – Experimental data and polynomial fit for "trapezoidal wing-fuselage" combination (V=40 m/s)
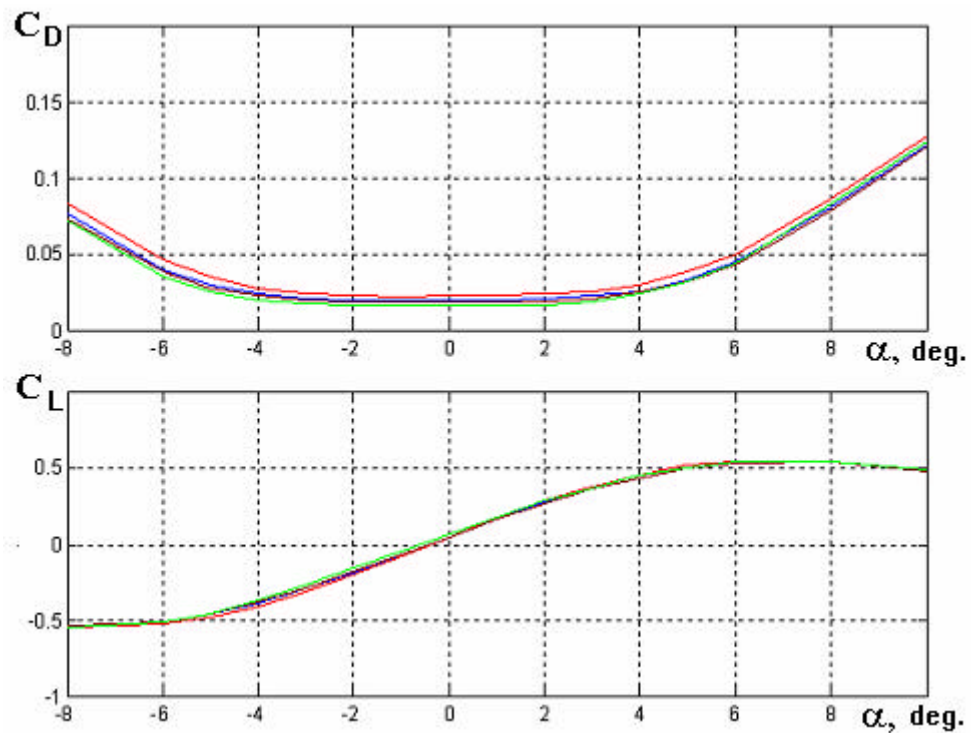
Figure 8.24 – Aerodynamic coefficients of "isolated" telescope wing
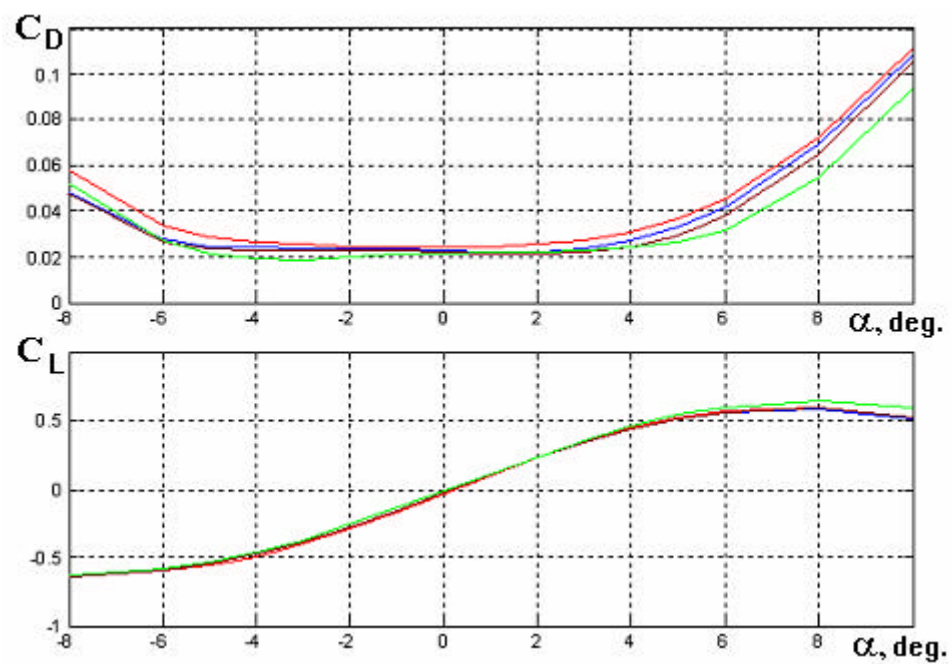
Figure 8.25 – Aerodynamic coefficients of "isolated" trapezoidal wing
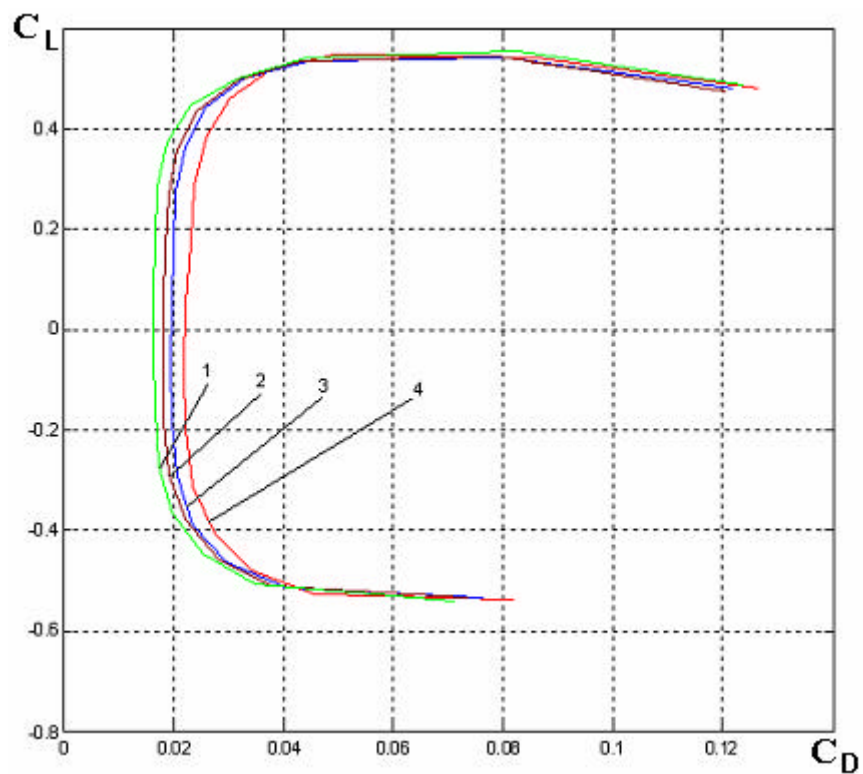
Figure 8.26 – Drag polars of "isolated" telescope wing
1 – V=40 m/s; 2 – 35 m/s; 3 – 30 m/s; 4 – 25 m/s
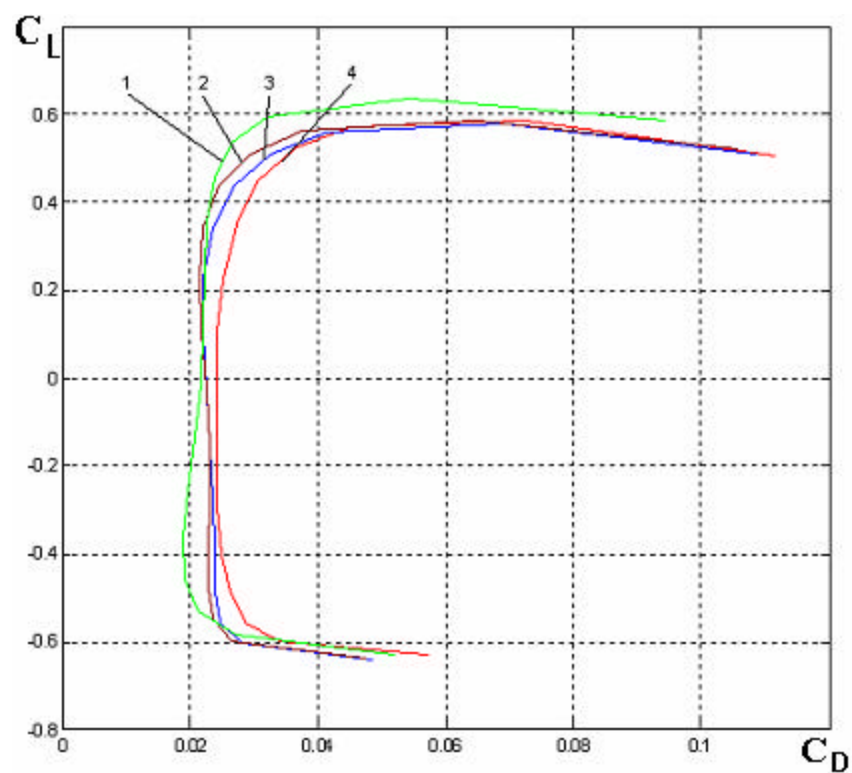
Figure 8.27 – Drag polars of "isolated" trapezoidal wing
1 – V=40 m/s; 2 – 35 m/s; 3 – 30 m/s; 4 – 25 m/s

8.3 Description of the telescope wing test model
for study of the pressure distribution

To study the pressure distribution at the telescope wing a test model with NACA 0012 airfoil and variable span of the movable part was manufactured. The model draft is shown at figure 8.28. Dash-and-dot lines mark the sections were pressure orifices are located. Each section has 16 pressure orifices. Coordinates of the orifices are listed in table 8.2. The numbering is staggered – orifices with even numbers are at one side of the wing and with odd numbers are at the other side of the wing. The first orifice is at the leading edge. General view of the model at different stages of manufacturing is shown at photos at figures 8.29 and 8.30.

Table 8.2 – Relative location of pressure orifices in the section

Point	1	2	3	4	5	6	7	8
x	0	0.025	0.040	0.073	0.113	0.165	0.225	0.295
Point	9	10	11	12	13	14	15	16
x	0.373	0.450	0.555	0.650	0.733	0.805	0.853	0.908
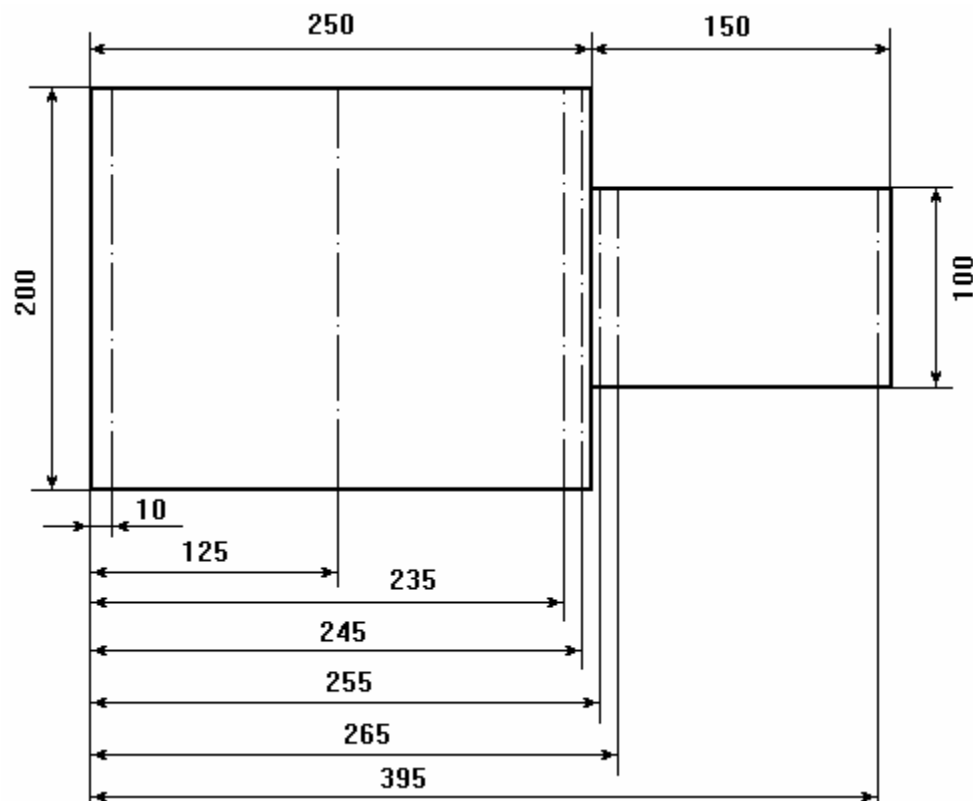
Figure 8.28 – Geometry of the telescope wing model.
Dash-and-dot lines mark sections with pressure orifices.
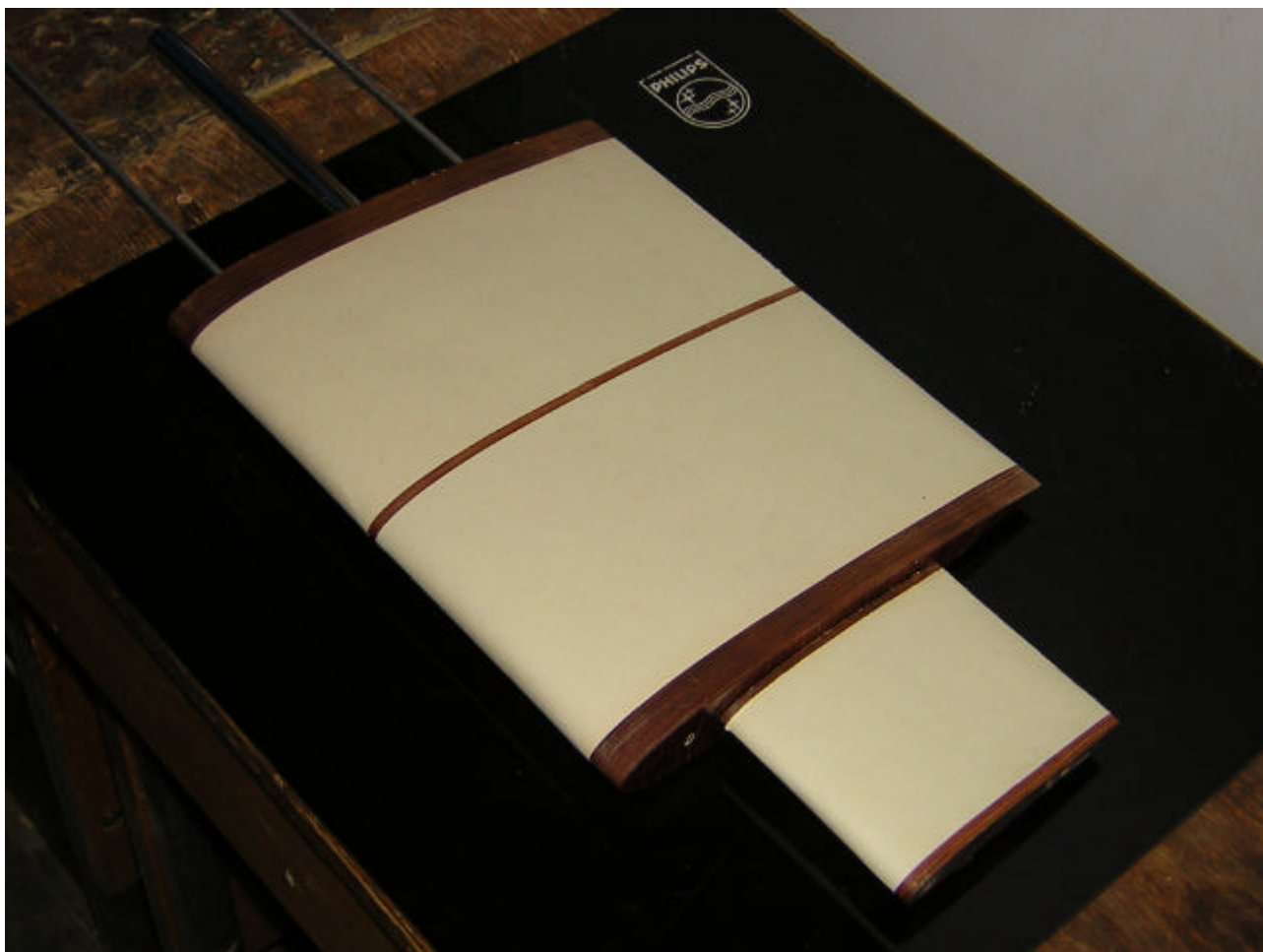
Figure 8.29 – Photo of the telescope wing model with pressure orifices
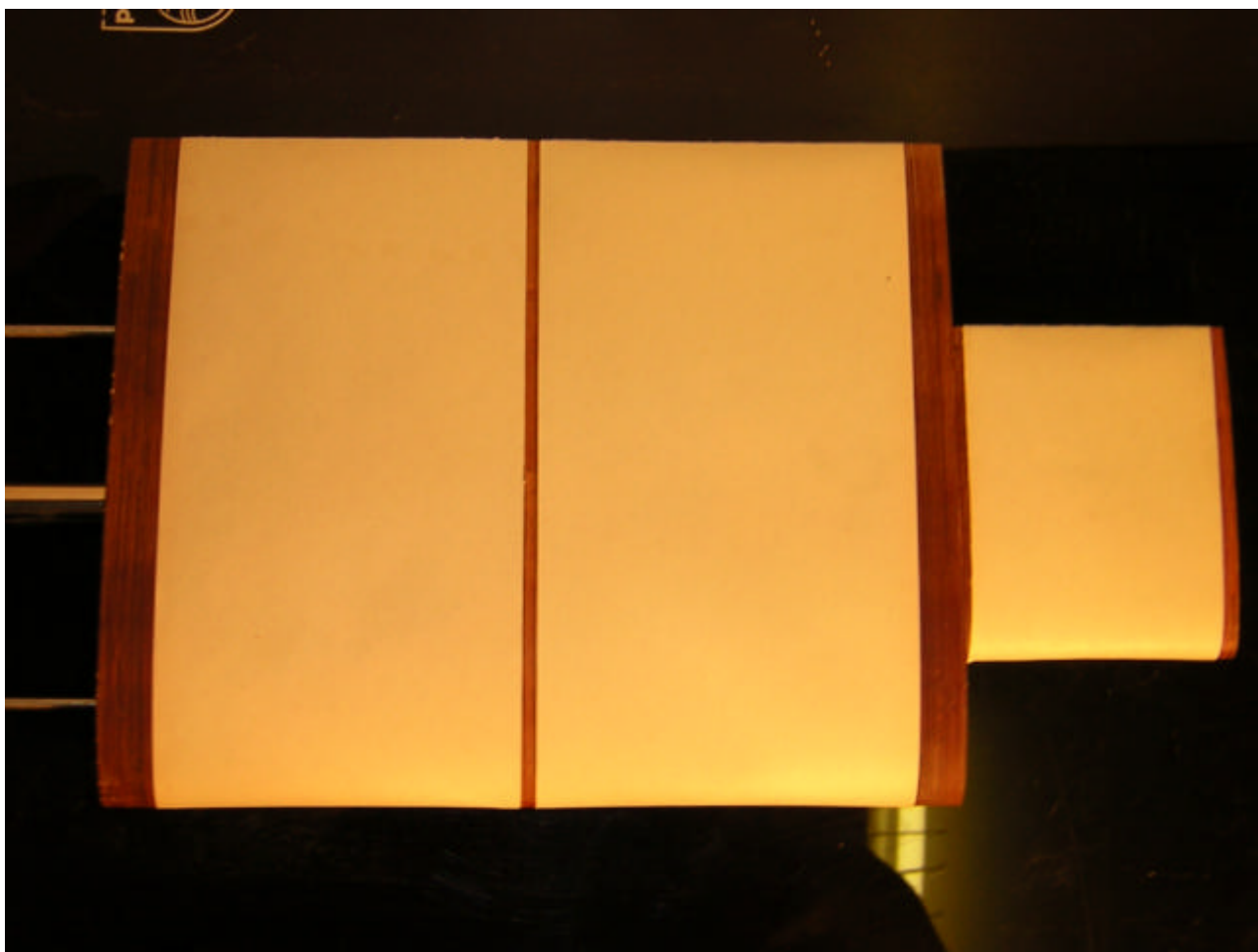
Figure 8.30 – Photo of the telescope wing model with pressure orifices

The wing model was fixed at the turntable, located at the supporting vertical plate made from organic glass. This allows changing the angle of attack of the wing (figure 8.31). To reduce the disturbances the leading edge of the supporting vertical plate was sharpened and shaped as a wedge. The flat inner surface of the plate serves as a screen, so the experiment can be performed with the half-model of the wing. This allowed to increase the size of the model and place inside if it 102 polyethylene tubes connecting the pressure orifices with pressure sensors (figure 8.32). The general view of the model installed in the test section of the wind-tunnel is shown at figures 8.33 and 8.34.

16 Honeywell^{TM} Sursence$^{®}$ pressure sensors, purchased with financing of the present project, were mounted at one board (figure 8.35). These sensors are connected with the common bus to the data acquisition board. PC with data acquisition board together with pressure sensors assembly makes automated pressure measurement system. Developed software scans the pressure sensors, processes the gathered data and displays the data at the computer screen. This

automated pressure measurement system sufficiently decreases the time required for the experiment and increases the reliability of the data by averaging a large number of observations for each pressure orifice.
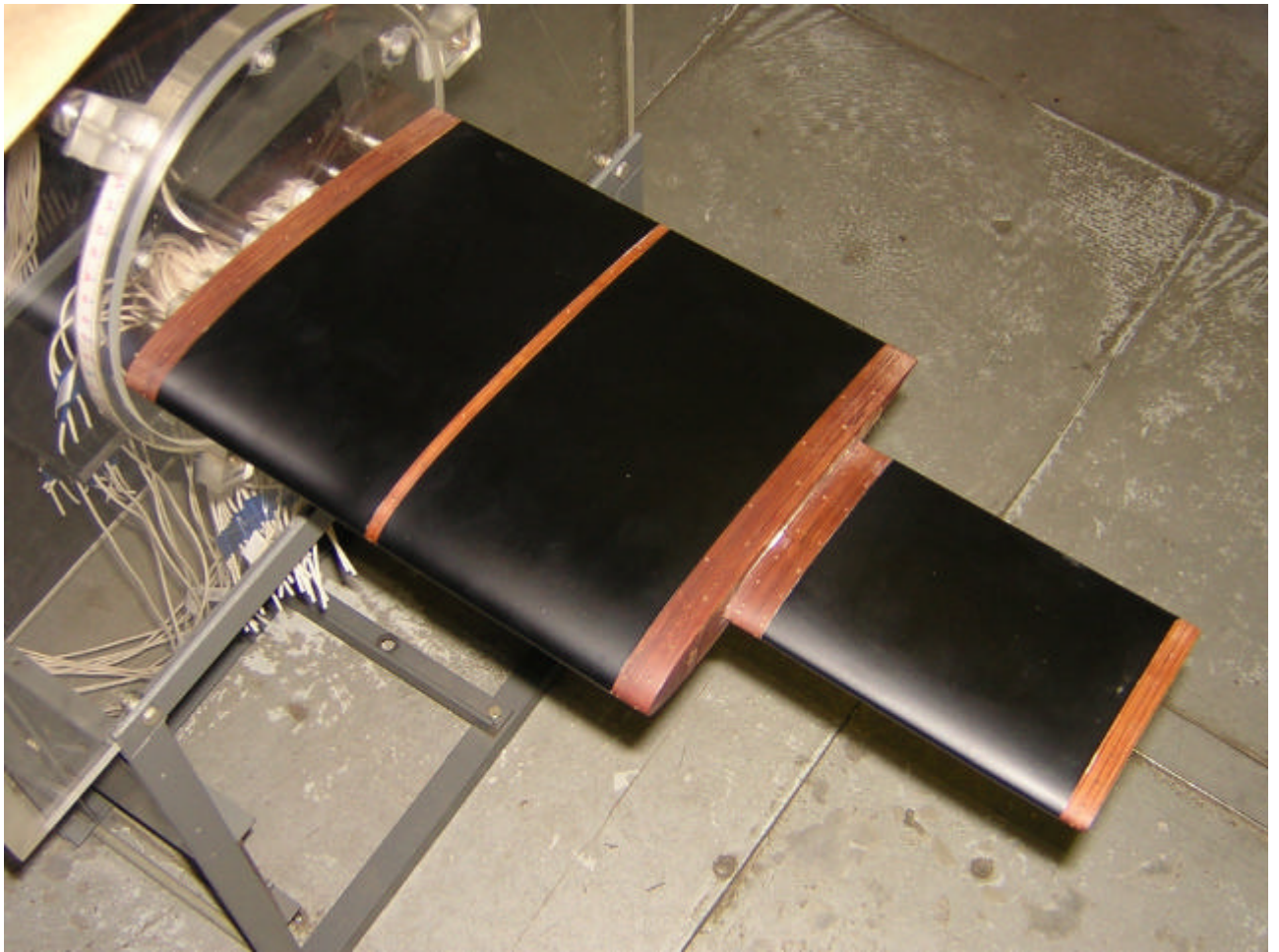
Figure 8.31 – General view of the model, turntable and supporting vertical plate
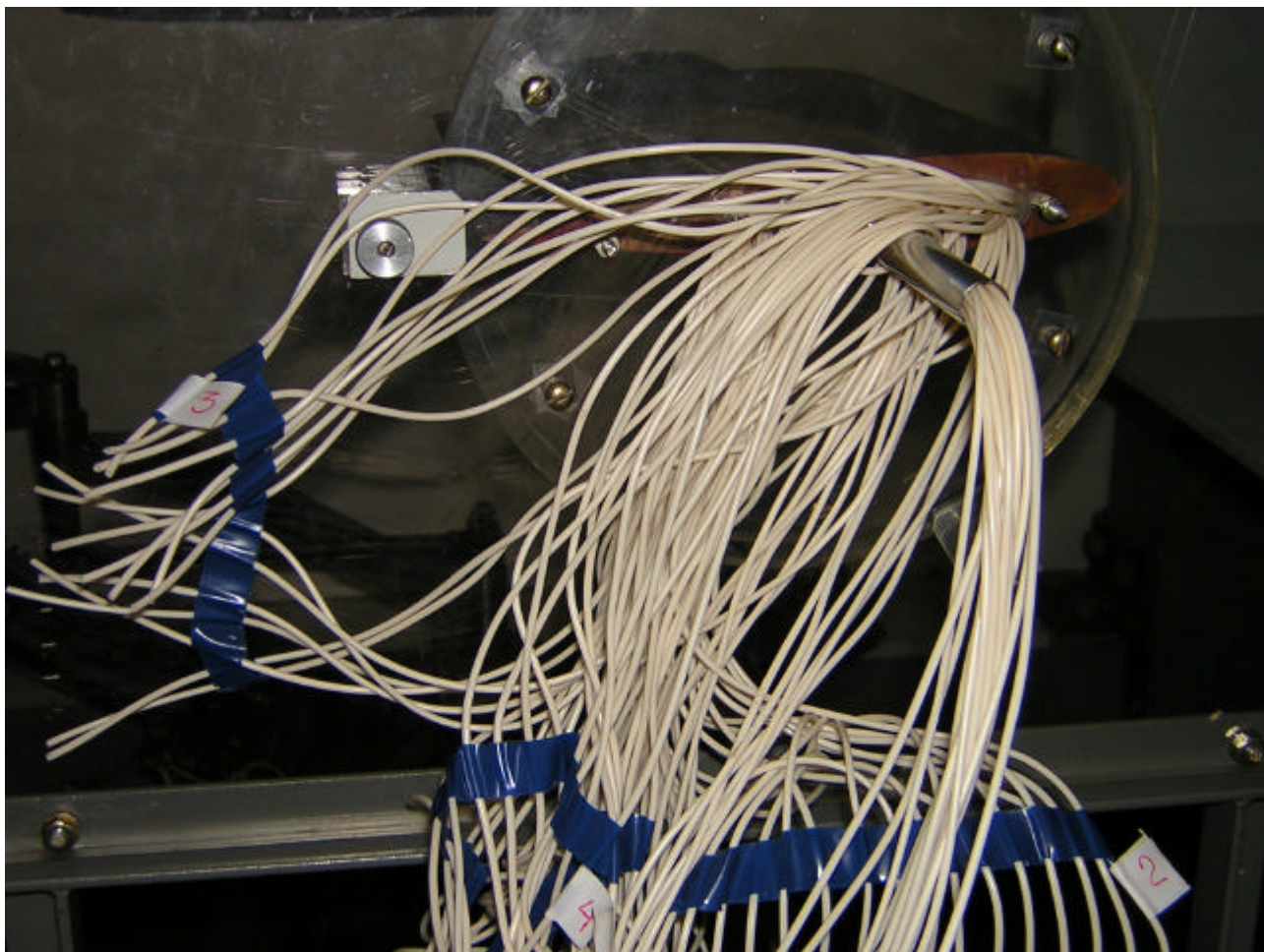
Figure 8.32 – General view of the tubes, connecting pressure orifices with pressure sensors
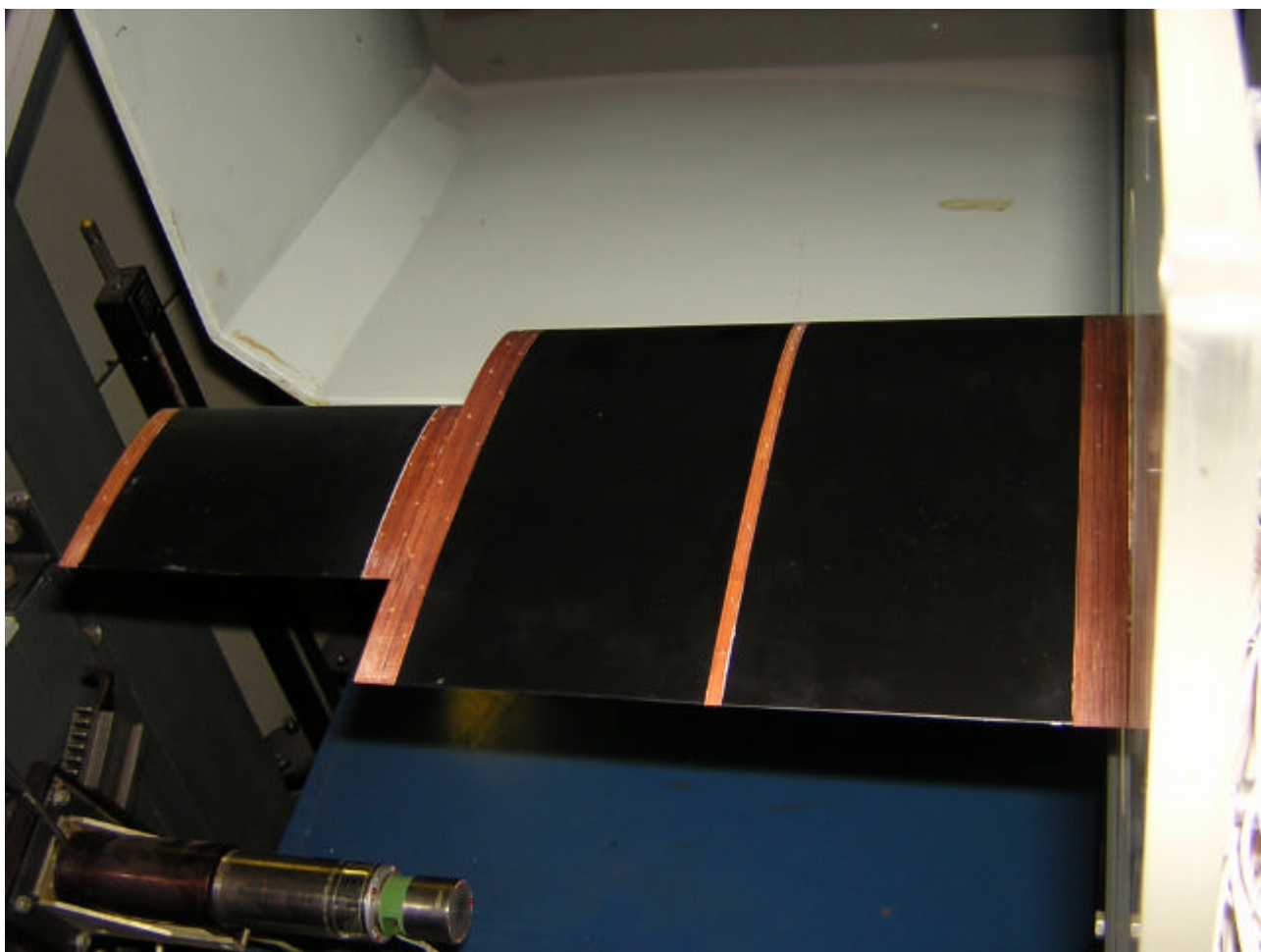
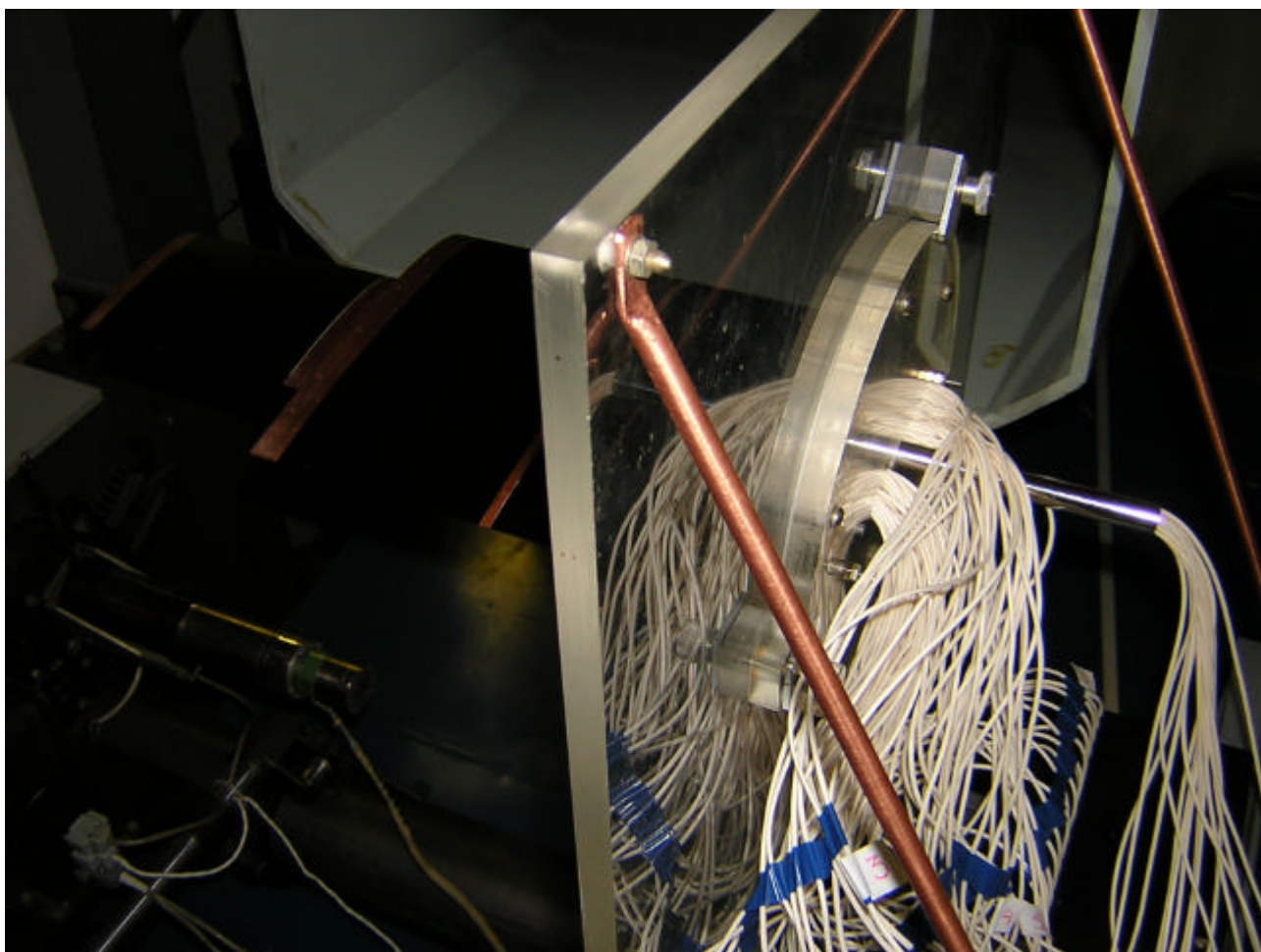Figure 8.33 – Location of the model in the test section of the wind-tunnel

Figure 8.34 – Location of the model in the test section of the wind-tunnel, turntable with limb and tubes are visible in the right part
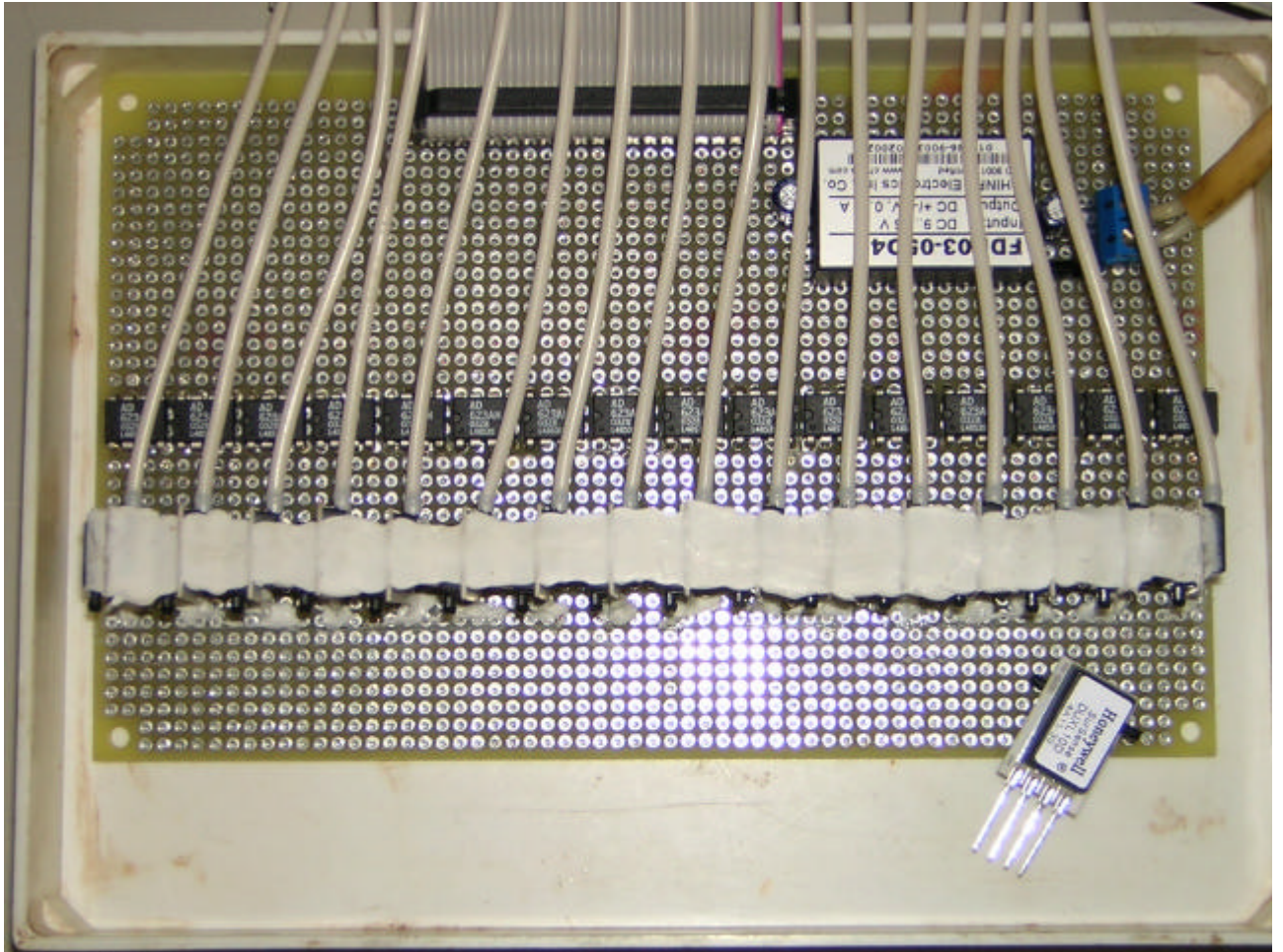
Figure 8.35 – Assembly of 16 pressure sensor. Single pressure sensor is at the front

8.4 Experimental results of pressure distribution study

Experiments were performed with the airspeed 37 m/s. Chord plots of pressure coefficient for all 7 sections for angles of attack α=5° and α=10° are shown at figures 8.36 and 8.37. Comparison of these experimental data with the results of numerical simulations shown at figures 7.31 – 7.36 reveals a good qualitative agreement. Both simulation and experiment show the distinct features of pressure distribution in section 4 and 7 of the model.

Pressure distributions were integrated to calculate section lift coefficients. These were used to calculate spanwise load distribution. Figure 8.38 presents comparison of experimental spanwise load distribution for α=5° with calculated load distributions shown before at figure 7.30. Experimental results displayed with circles. A specific "kink" at the spanwise load distribution at the joint between two parts of the wing is captured in both experimental and computational study.

A good agreement was found between the results of computational and experimental research of the telescope wing aerodynamics. This can be considered as successful cross-validation of the computational methods and software (including specially developed in SSAU) and experimental techniques and methodology.
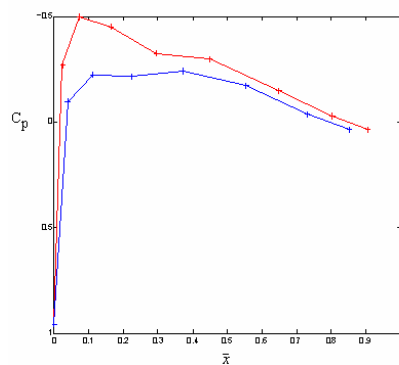
The revealed flow features at the joint between two parts of the wing can be a subject of further research aimed at flow control in this area in order to increase aerodynamic performance of the telescope wing.
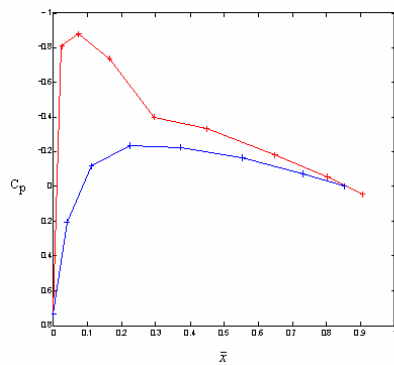
Section 1
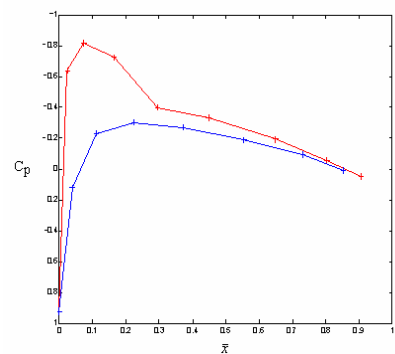
Section 2
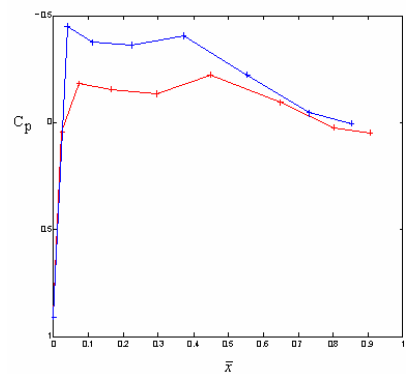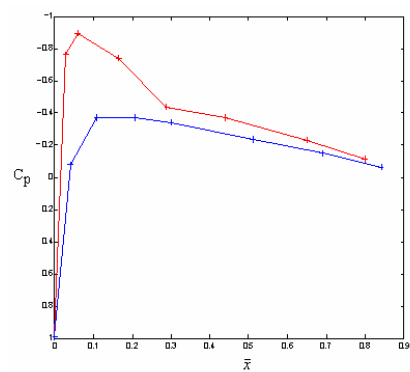
Section 3
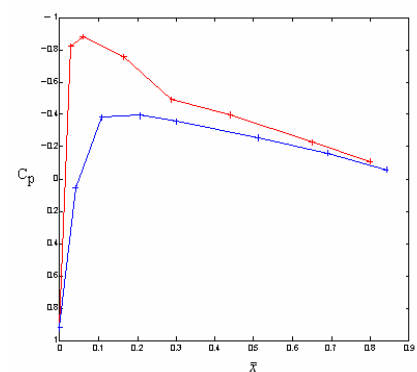
Section 4
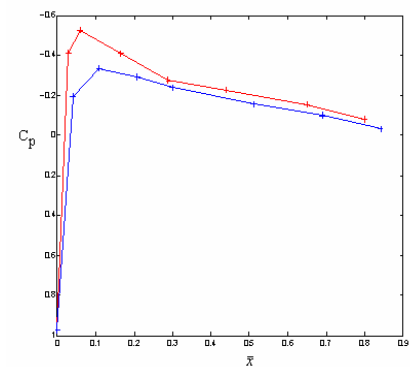
Section 5
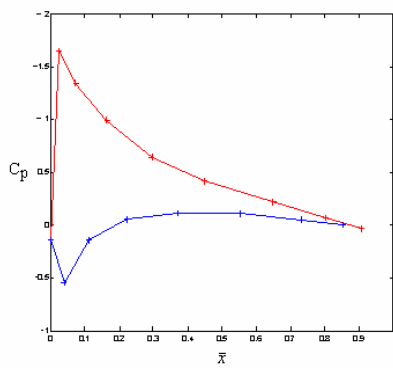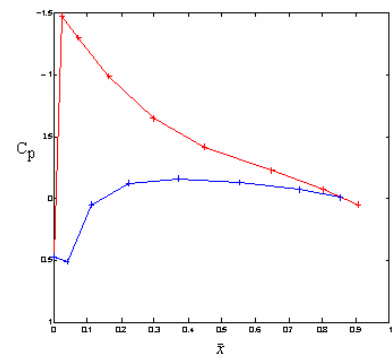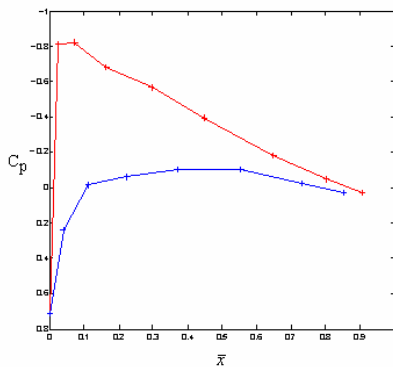

Section 6

Section 7

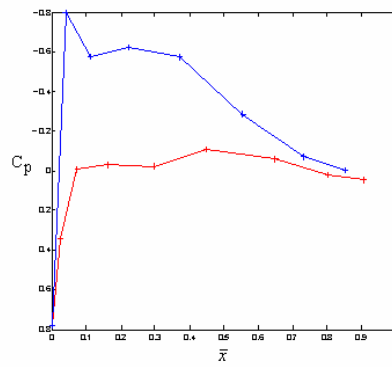Figure 8.36 – Chord plots of pressure coefficient, $a = 5°$

Section 1
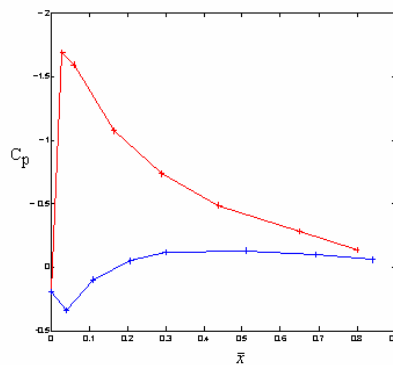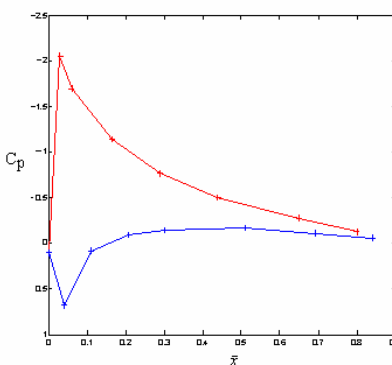
Section 2

Section 3
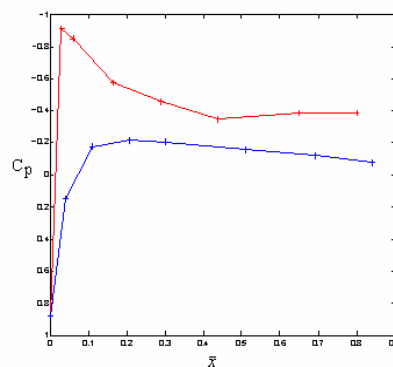
Section 4

Section 5

Section 6

Section 7

Figure 8.37 – Chord plots of pressure coefficient, $a = 10°$

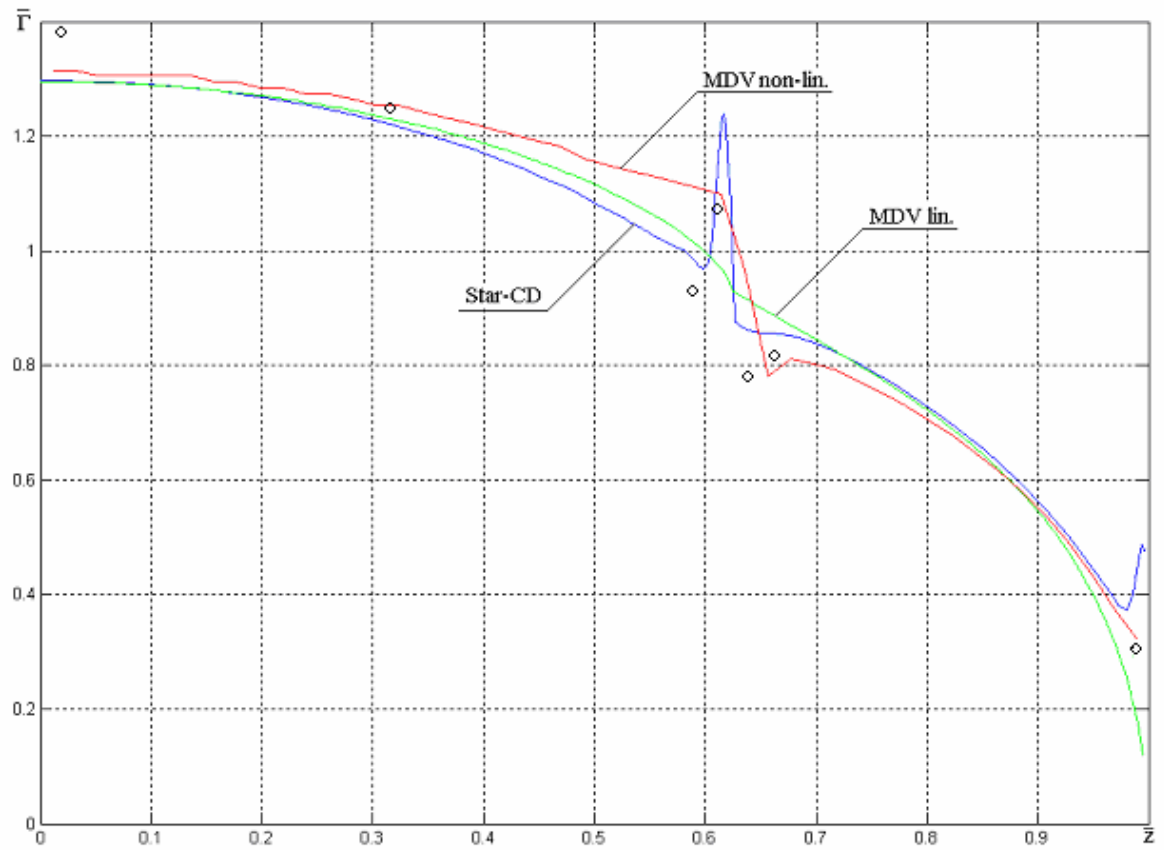Figure 8.38 – Comparison of experimental ($\boldsymbol{a} = \boldsymbol{5}^\circ$)
and calculated spanwise load distributions for the telescope wing

9 Research of telescope wing weight and aerodynamic efficiency

9.1 Preliminary analysis

For the tasks of the present work a following algorithm was proposed:

1. Create two solid bodies - fixed and mobile parts of a wing (figure 9.1).

2. Assume that these "solids" can have nonuniform density distribution.

3. Join these solids in different ways - Gevers' version (#1) [7] and so on (figure 9.2).

4. Optimize the density distribution within these solid.

5. Calculate LCF and new dimensionless criteria of weight efficiency.

Figure 9.1 – Fixed and mobile parts of a telescope wing
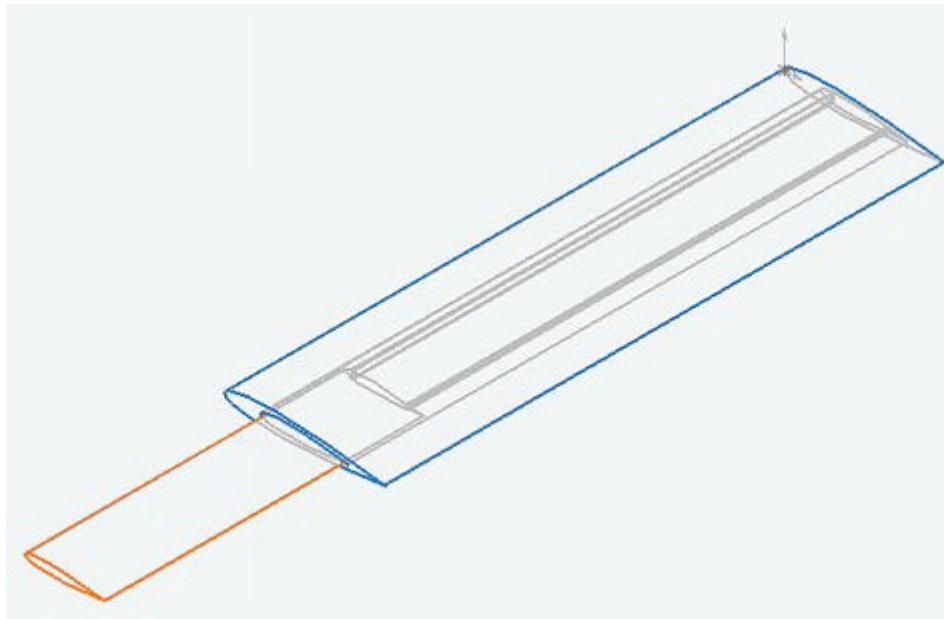
For optimization of density distribution in item 5 of the algorithm for LCF calculation an iterative procedure is used, which operates as following:

1. Some initial density distribution r_{oi}, usually uniform, is assigned for the whole structure.

2. Stresses within all elements are calculated and for each element the equivalent stress s_{oi}^{eqv} is defined.

3. New element densities r_{1i} are calculated as:

$$r_{1i} = \frac{s_{oi}^{eqv}}{[\bar{s}]}, \qquad (9.1)$$

where $[\bar{s}]$ is the allow stress at unit density.

The procedure is repeated until stabilization of density distribution.

At each iteration after step 2 the value of LCF is calculated in order to monitor its change during the optimization procedure.
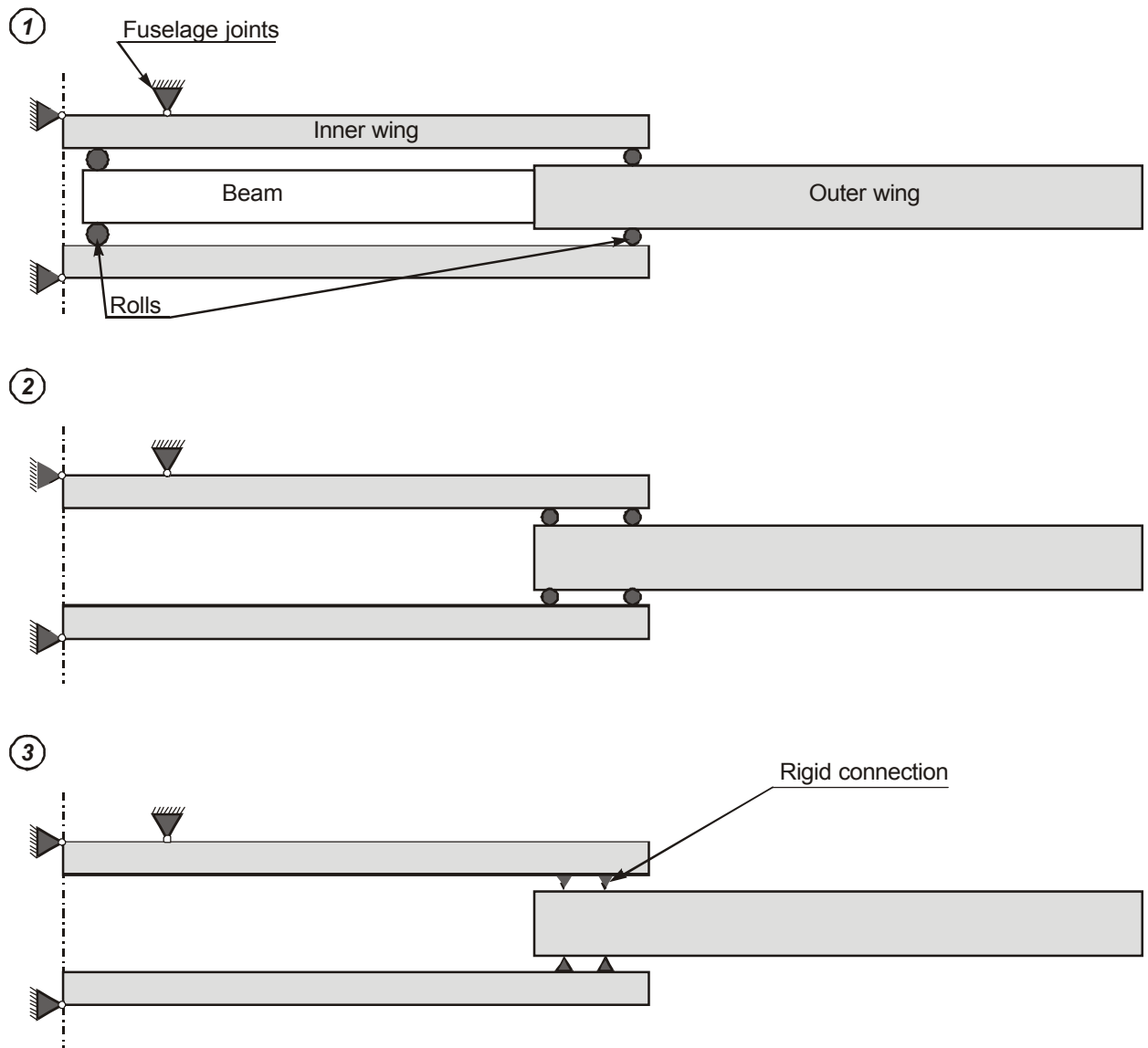

Figure 9.2 – Schemes of wing parts joints

FEM model shown at figure 9.3 was developed for weight efficiency analysis of telescope wing.

Geometry of model #1 of the telescope wing is shown at figure 9.4.

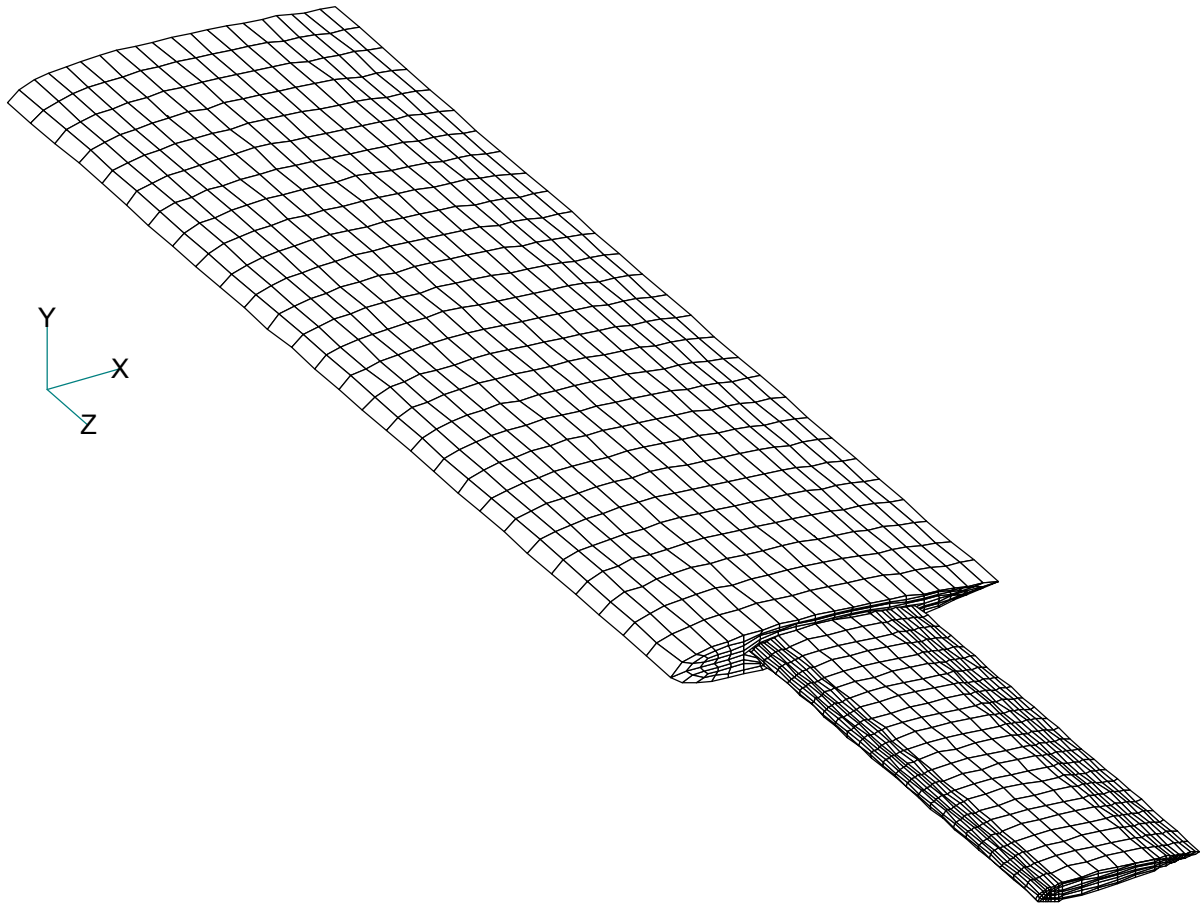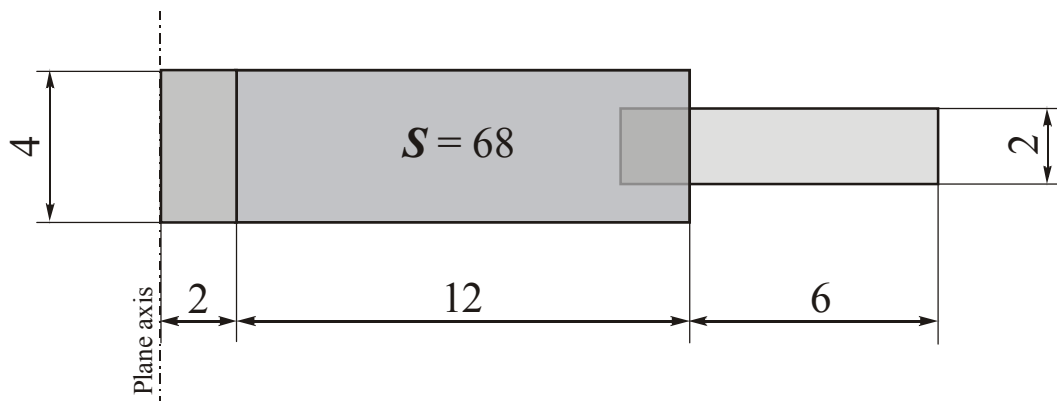Figure 9.3 – Telescope wing FEM model

Figure 9.4 – Geometry of model #1 of the telescope wing

To estimate weight and aerodynamic efficiency of telescope wing the same analysis was carried out for equivalent conventional trapezoidal wing with the same area, span, taper ratio $l = 0.5$ and dimensionless airfoil thickness $\bar{t} = 12\%$. Geometry of this wing and its FEM model is show at figures 9.6 and 9.5.
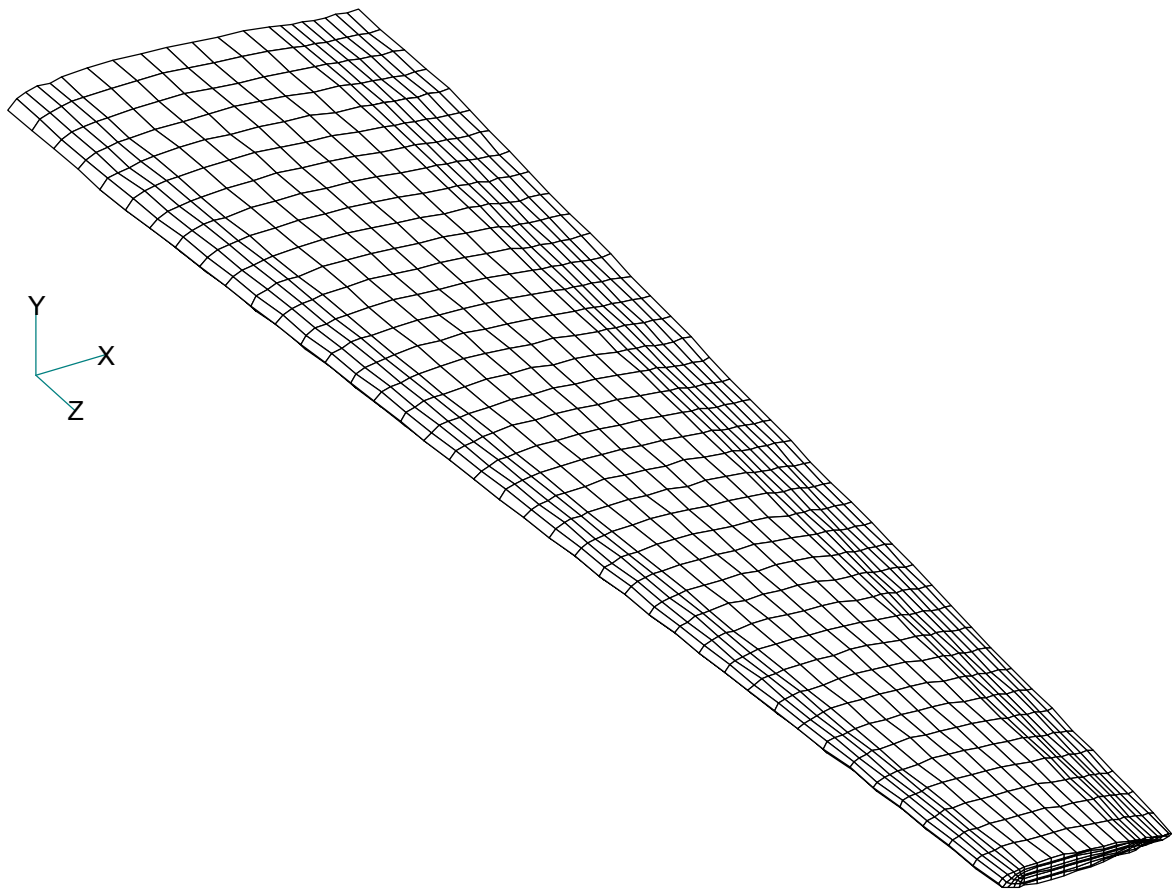
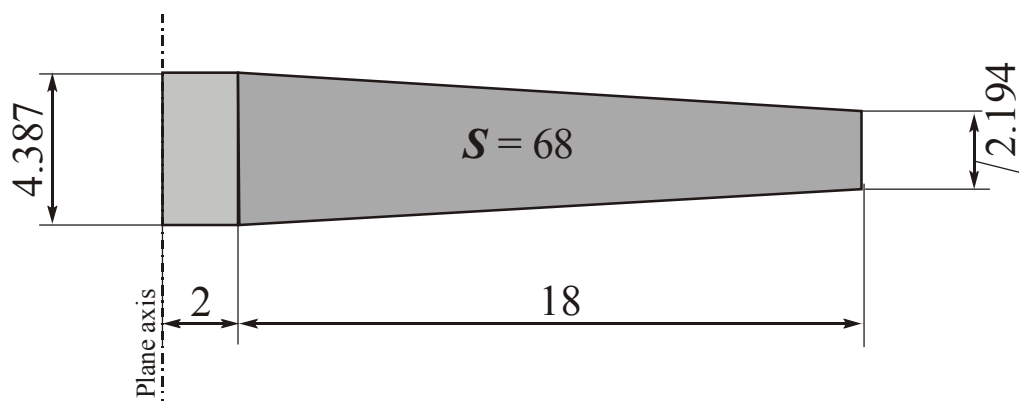Figure 9.5 – Equivalent trapezoidal wing FEM model

Figure 9.6 – Geometry of the equivalent trapezoidal wing

For preliminary weight calculations uniform load distribution was used. The following results were obtained:

1. Comparative analysis of three different designs of the joint between fixed and movable (extendable) parts of the telescope wing have shown that among them

the most preferred is design #2, presented at figure 9.2. It has 15% better weight performance than design #1 (Gevers) [7].

2. For the uniform wing load distribution the calculations of the dimensionless coefficient of the load-carrying factor yield the following results:

for the telescope wing shown at figure 9.4 $C_K = 31{,}1$;

for conventional equivalent trapezoidal wing with the same aspect ratio and area, and with taper ratio $l = 0.5$, as shown at figure 9.6 $C_K = 30{,}86$.

Thus an interesting result was obtained. Telescope wing can has nearly the same weight as conventional trapezoidal wing with equivalent geometry. Such unexpected result can be explained by the following reasons:

First, the design #2 of the joint, which is shown at figure 9.2, does not cause sufficient increase of mass.

Second, for the assumed uniform wing load distribution the movable (extendable) part of the telescope wing is subjected to less net load than the corresponding part of conventional wing.

That is why in the following calculations with the account for spanwise load distribution the design #2 was used for the joint (figure 9.2).

9.2 Weight and aerodynamic analysis of telescope wings with the account for spanwise load distribution

Three pairs of wings were considered (figure 9.7). An equivalent trapezoidal
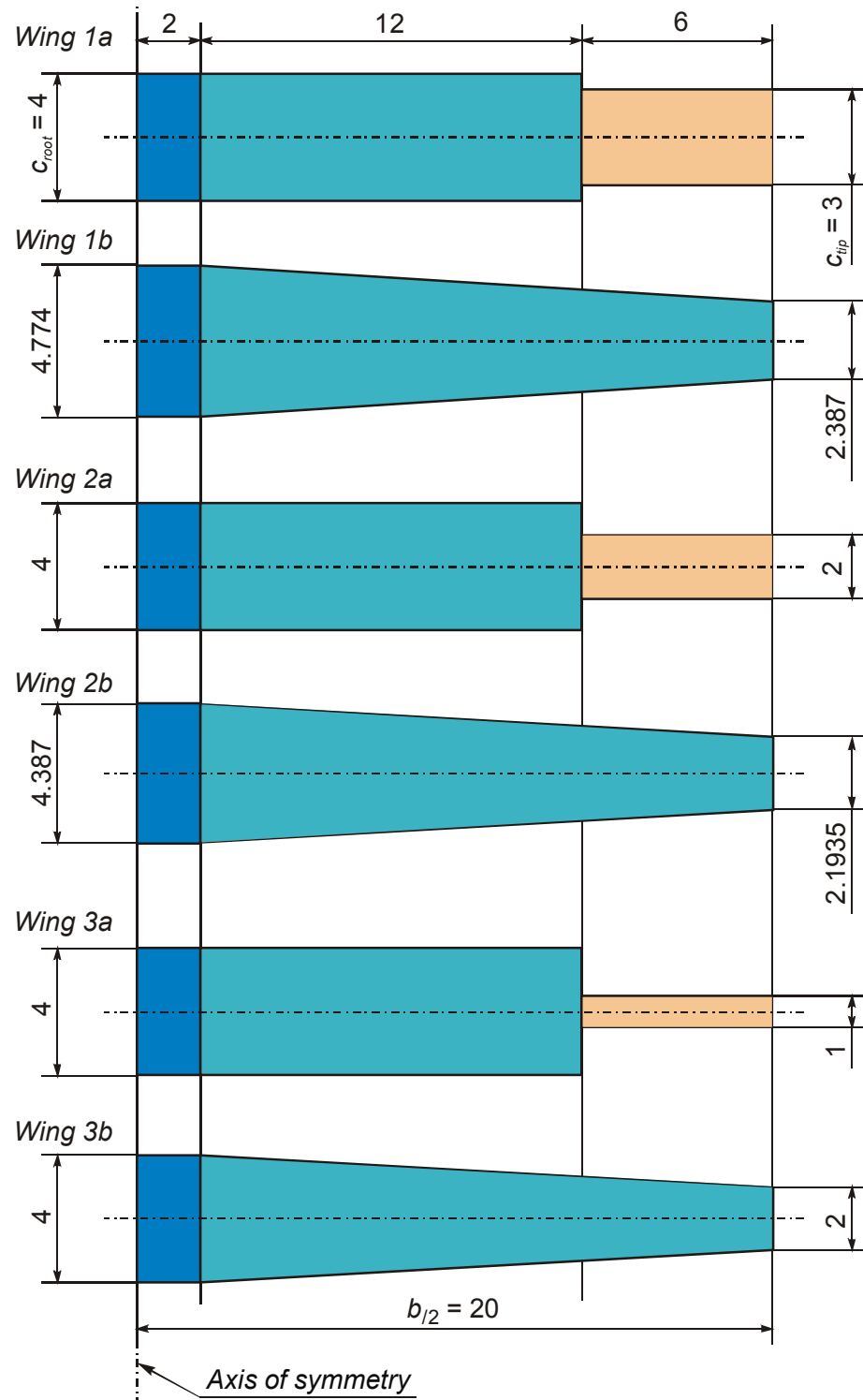

Figure 9.7 – Geometric characteristics of considered wings

wing with the same area, span and taper ratio $l = 0.5$ corresponds to each telescope wing. Airfoils with dimensionless thickness $\bar{t} = 12\%$ were used for all calculations.

Table 9.1 presents the aerodynamic performance of these wings, showing their high aerodynamic efficiency.

Table 9.1 – The aerodynamic performance of considered wings (see section 7)

Wing	$\bar{c}_t$	A	C_{La}	K	C_{Do}	L/D_{max}
1a	0.75	9.818	4.9197	0.0354	0.00636	33.290
1b	0.75	10.058	4.9362	0.0323	0.00643	34.692
2a	0.50	10.800	5.0183	0.0301	0.00639	36.051
2b	0.50	10.941	5.0238	0.0297	0.00653	35.895
3a	0.25	12.000	4.9096	0.0311	0.00638	35.461
3b	0.25	12.000	5.1146	0.0272	0.00663	37.257

Figure 9.20 explains the value of $\bar{c}_t$.

For weight analysis, which is discussed further, spanwise load distributions shown at figures 9.8 - 9.11 were used.
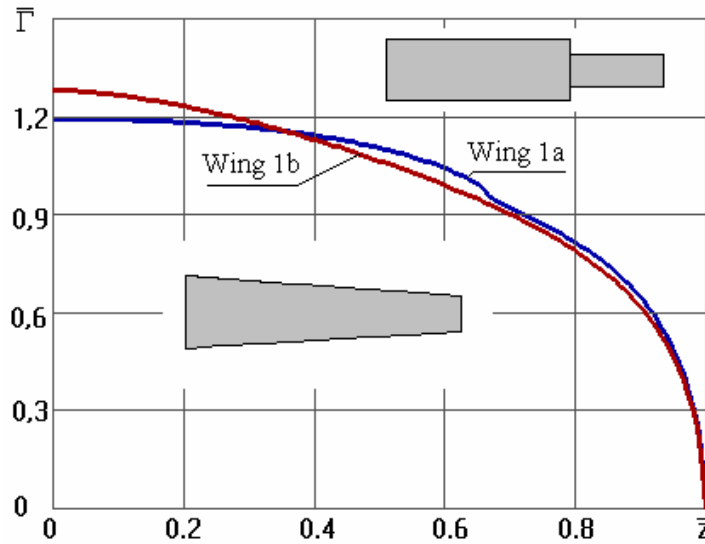

Figure 9.8 – Wings 1a, 1b dimensionless velocity circulation
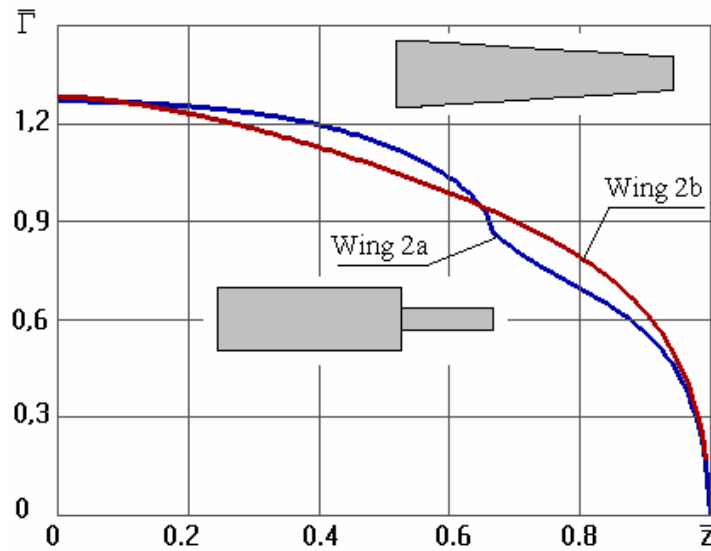
Figure 9.9 – Wings 2a, 2b dimensionless velocity circulation
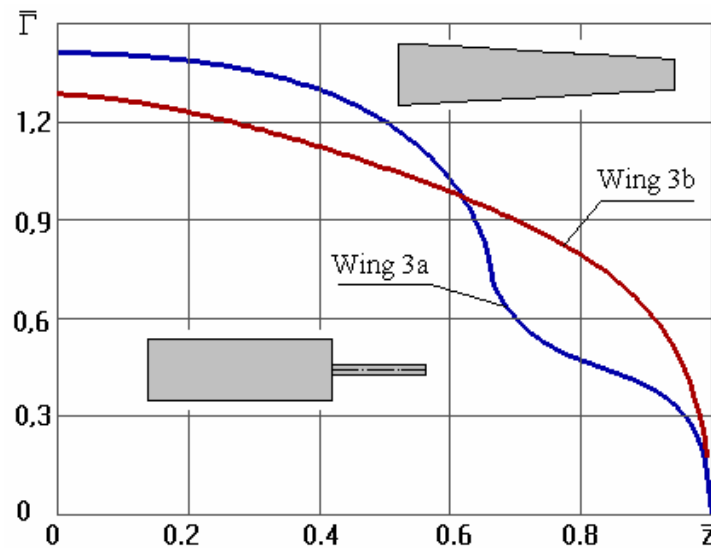
Figure 9.10 – Wings 3a, 3b dimensionless velocity circulation
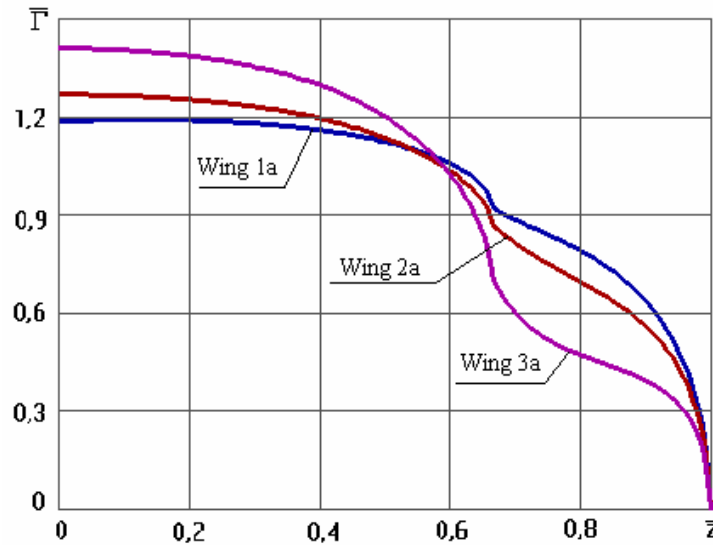
Figure 9.11 – Wings 1a – 3a dimensionless velocity circulation

FEM models of the wings 2a and 2b with loads are shown at figures 9.12 and 9.13.

Figures 9.14 and 9.15 illustrate the proposed load-carrying scheme and load transfer in the joint of telescope wing.

Results of weight analysis for all of the six wings are presented in table 9.2. Columns depict the change of C_K during the process of material distribution optimization.
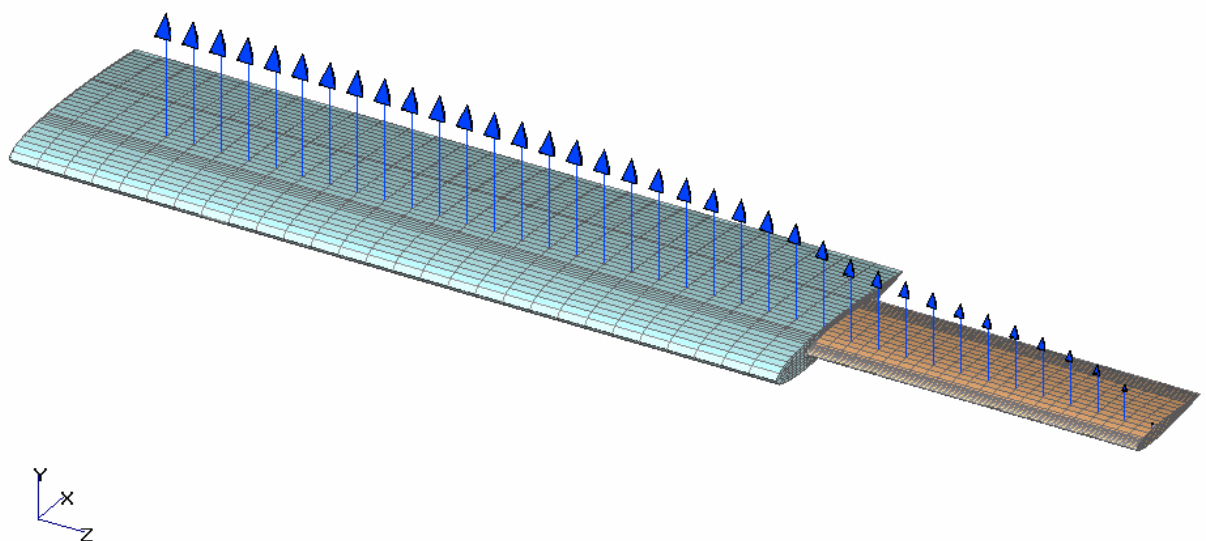
Figure 9.12 – Loads via dimensionless velocity circulation for a telescope wing
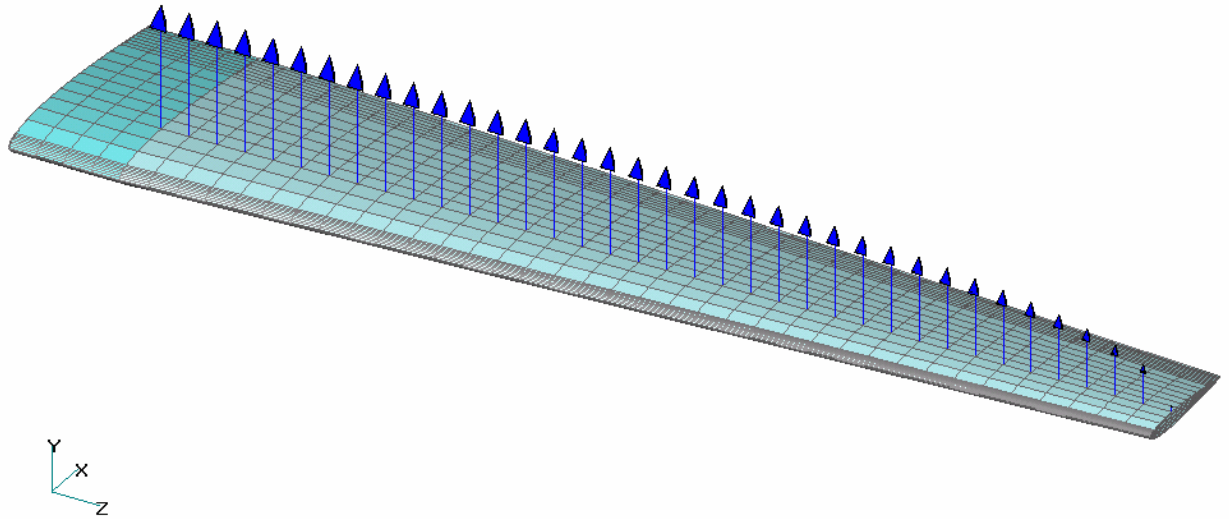
Figure 9.13 – Loads via dimensionless velocity circulation for equivalent trapezoidal wing

Calculations of C_K for wings 3a and 3b gave the values 23.39 for telescope wing and 28.98 for equivalent trapezoidal wing. This yields that telescope wing can theoretically have even less weight than aerodynamically similar trapezoidal wing. Prima facie, this result seems paradoxical and requires explanation.
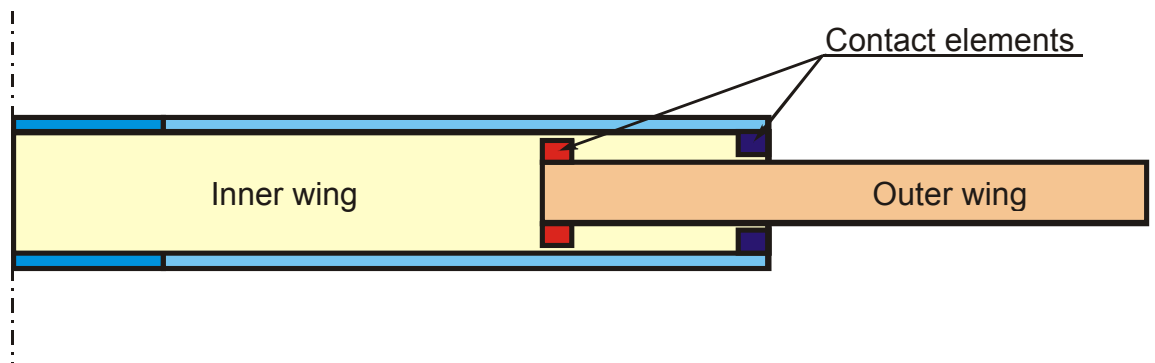
Figure 9.14 – Scheme of contact elements displacements
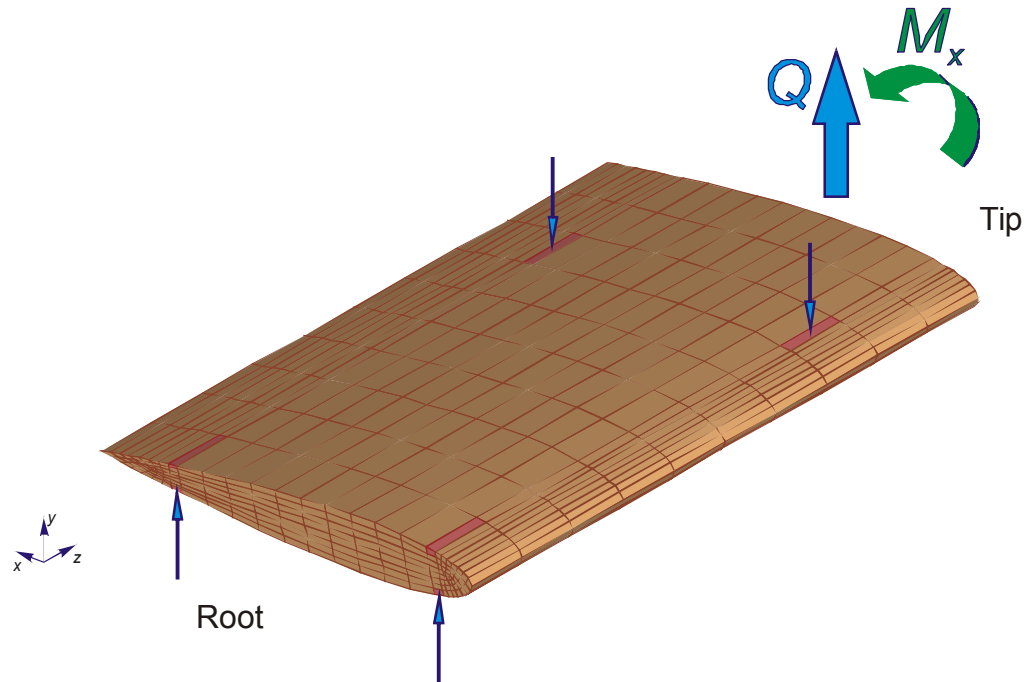
Figure 9.15 – Contact elements loading

The weight of high-aspect-ratio wing is mostly influenced by the magnitude of bending moment and airfoil thikness of the wing. Figure 9.16 shows the distribution of bending moment M_x for wings 3a and 3b. It can be seen that the telescope wing has considerably smaller bending moment along its whole span. The weight of unit length of the high-aspect-ratio wing can be considered proportional to M_x/t_{max} in the given cross-section. Thus it can be taken as the first estimation that the weights of the considered wings is determined by two controversial factors M_x and t_{max}. Distributions of M_x/t_{max} for wings 3a and 3b are shown at figure 9.17. This plot explains why the telescope wing can be lighter than trapezoidal.

Table 9.2 – Calculation of C_K criteria for wings

Name	Wing 1a	Wing 1b	Wing 2a	Wing 2b	Wing 3a	Wing 3b
C_{K1}	31,9970	31,5810	33,5743	35,7660	32,8615	40,9904
C_{K2}	29,4924	27,3511	30,2403	30,9658	28,8096	35,4783
C_{K3}	28,3572	25,4112	28,5571	28,7560	26,8196	32,9297
C_{K4}	27,6988	24,2965	27,5169	27,4818	25,6503	31,4570
C_{K5}	27,2615	23,6102	26,8121	26,6946	24,9175	30,5437
C_{K6}	**26,9466**	23,1572	26,3070	26,1767	24,4245	29,9438
C_{K7}	-	22,8375	25,9323	25,8114	24,0761	29,5208
C_{K8}	-	22,6049	**25,6476**	25,5439	23,8219	29,2110
C_{K9}	-	**22,4331**	-	**25,3466**	23,6343	**28,9811**
C_{K10}	-	-	-	-	23,4933	-
C_{K11}	-	-	-	-	**23,3864**	-
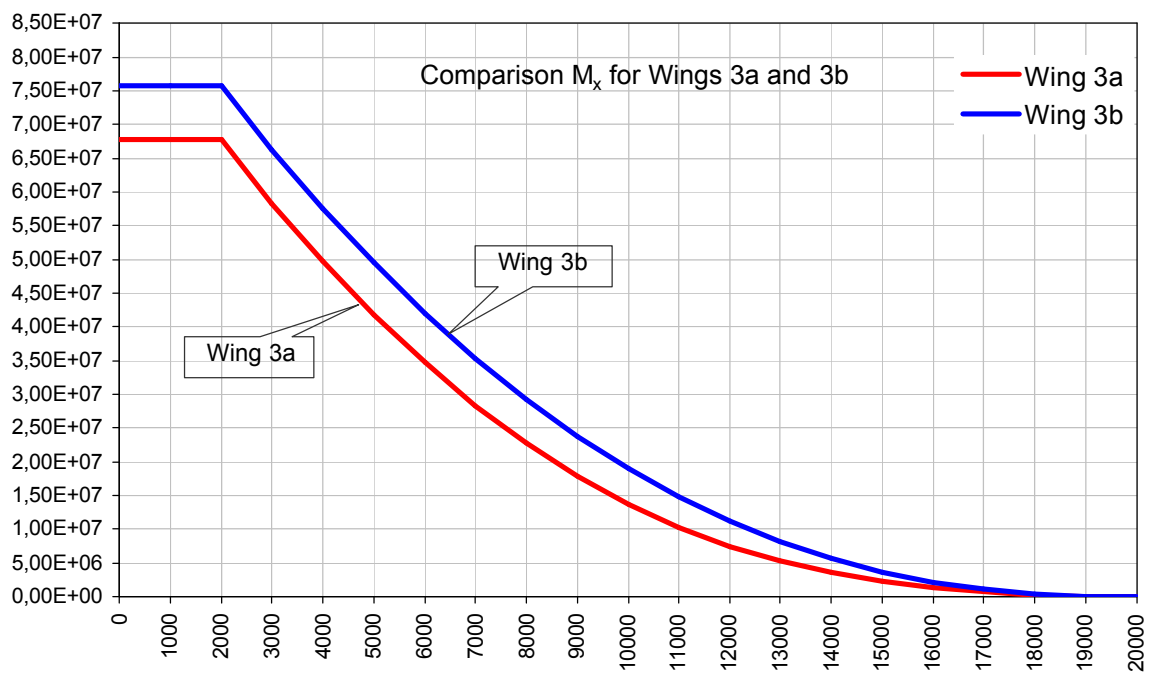
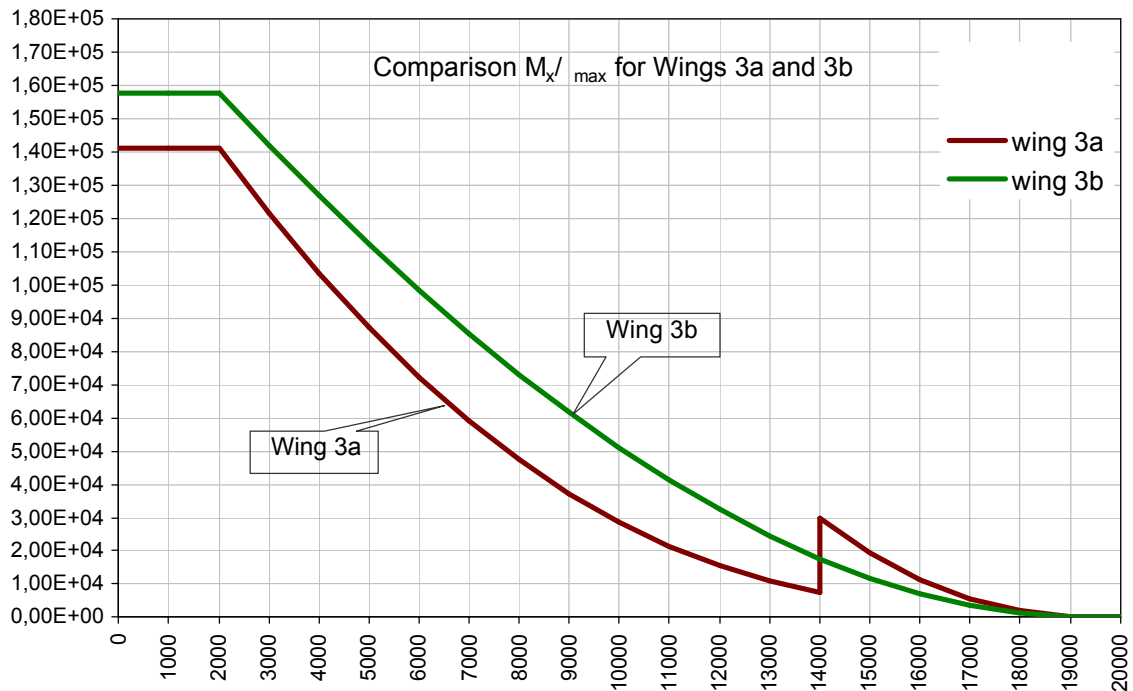Figure 9.16 – Comparison M_x for wings 3a and 3b

Figure 9.17 – Comparison M_x/t_{max} for wings 3a and 3b

According to the results of our research for the telescope wing the joint itself doesn't yield sufficient increase of C_K. We were trying to intentionally worsen and place contact pairs in the area of t_{max} of the main part of the wing. This leads to greater load on the tip rib. Sufficient increase of C_K by 2.3% was obtained only for the wing 1a. It can be assumed that the presence of the joint causes only some increase in constructional coefficient j (full mass coefficient).

9.3 Comparison weight and aerodynamic efficiency of the telescope and eqvivalent trapezoidal wings

Research results for weight and maximum lift-to-drag ratio L/D_{max} of telescope and equivalent trapezoidal wings are plotted at figures 9.18, 9.19.

Figure 9.20 presents all the necessary geometrical explanations.

From figures 9.18 and 9.19 it follows that the considered telescope and equivalent trapezoidal wings have nearly the same weight and aerodynamic efficiency. (Dimensionless coefficient C_K determines the wing weight with an accuracy to constant multiplier. See section 4.4, (4.17, 4.18, 4.19).)

For some geometrical parameters the telescope wing theoretically can have less weight then the equivalent trapezoidal wing.
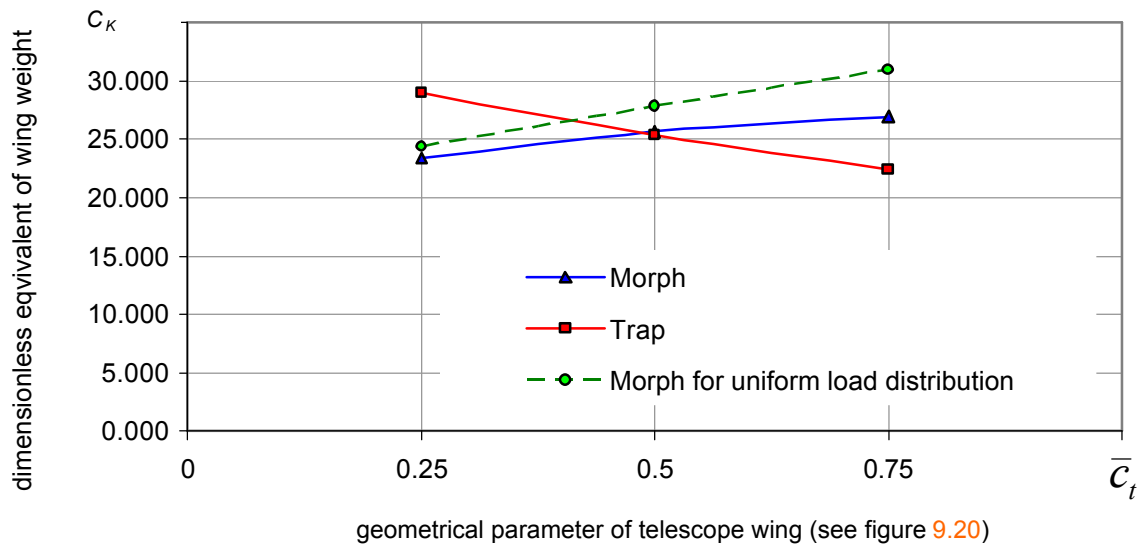
Figure 9.18 – Comparison C_K for wings after iterations
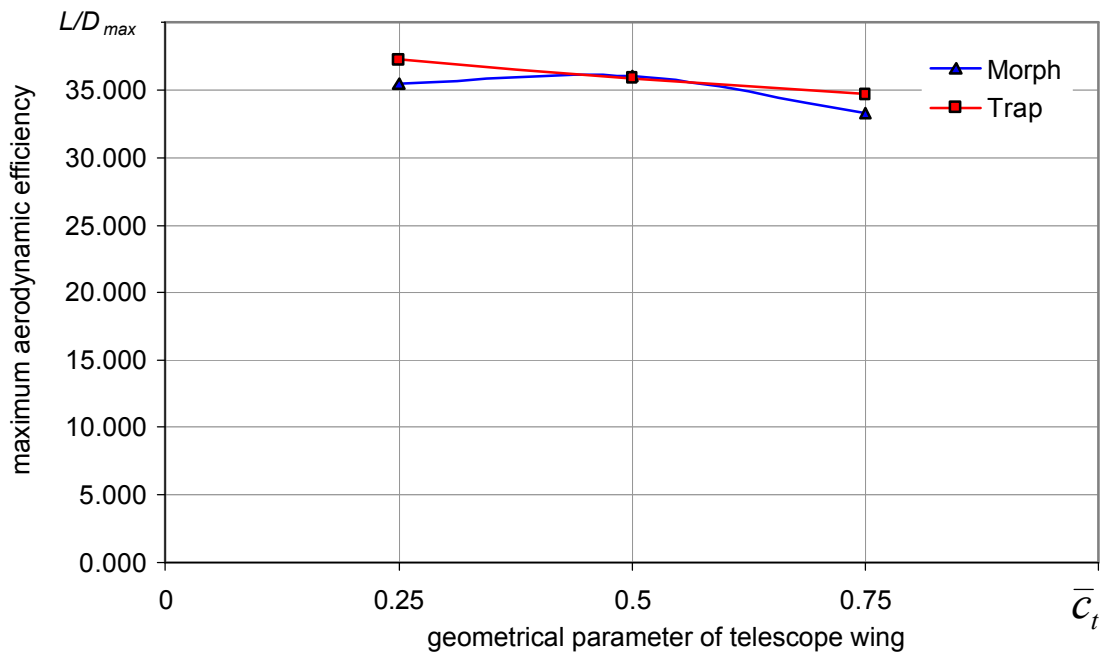
Figure 9.19 – Comparison maximum aerodinamic efficiency for wings

Addition. Sign "○" on figure 9.18 presents a load-carrying factor coefficient calculated for uniform load distribution. This results shows the simplified load application gives ability to adequate comparison of various configurations of wings.
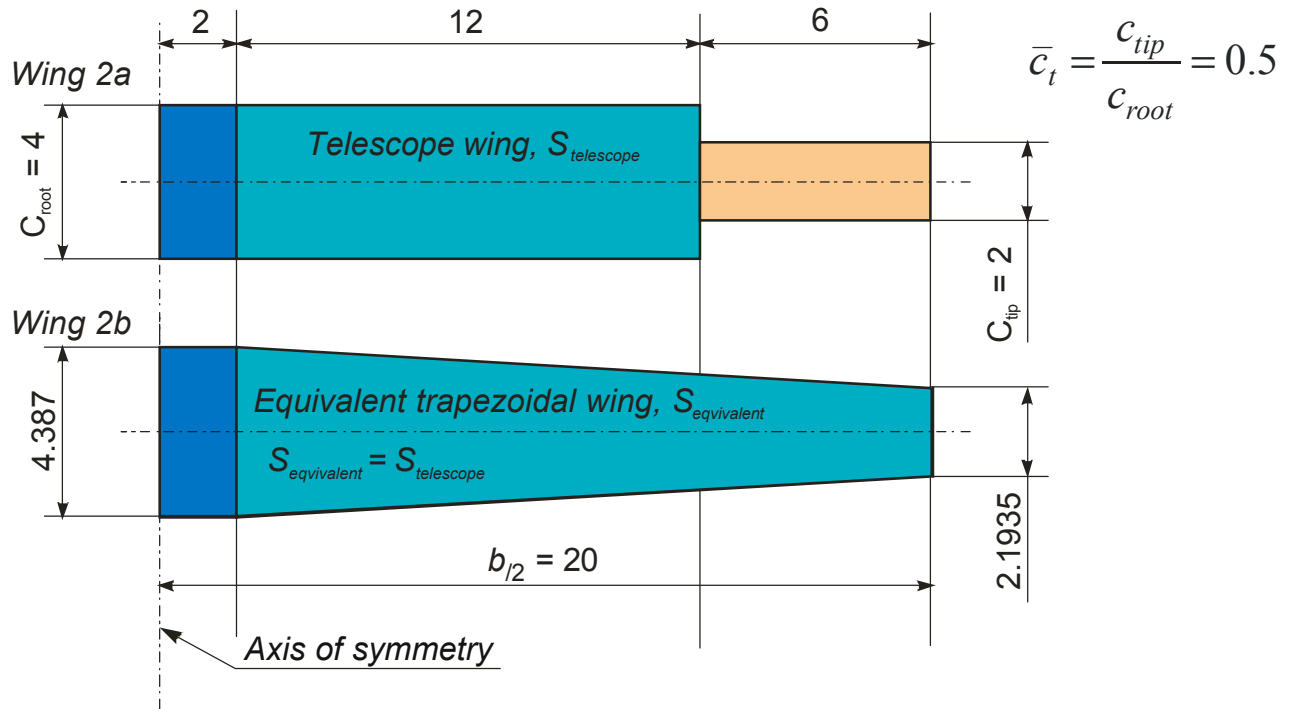
Figure 9.20 – Explanation for choise of geometric characteristics equvalent trapezoidal wing

$$\overline{c}_t = \frac{c_{tip}}{c_{root}}$$ - dimensionless chord of rectangular outer wing part

(referenced to the tip chord of the main part of the wing);

10 Results and conclusions

1. Accuracy analysis for some known wing weight formulas was performed, showing that they give too wide spreading of the results (tens of percents) and are not able to account for some features of morphing wing.

2. New method was proposed in order to increase accuracy of weight design and provide adequate comparison of different engineering solutions. In principal new in this method are use 3D-models with optimization of variable density of elements for calculation of load-carrying factor for theoretically optimal structures, and introduction of dimensionless load-carrying factor coefficient, showing the weight perfection of load-carrying structure. This criteria allows objective comparison of different structure, thus creating knowledge- and database of different engineering solutions. New weight formulas developed basing on this criteria, which allow to calculate absolute wing mass and wing mass fracture. The proposed approach do not impose any limitations for external shapes and boundary conditions of wing structures.

3. For telescope wings a wide range of aerodynamic research was performed. Spanwise load distribution was calculated with three different computational methods. It was shown that discrete vortex method provides reasonably accurate results. This method was used for calculation of spanwise load distribution for telescope and trapezoidal wings.

4. Three test models for wind-tunnel testing were designed and built in order to verify computational methods used for telescope wing aerodynamic calculations. Two models for load tests and one, with pressure orifices, for study of pressure distribution in the joint area of the telescope wing. Wind-tunnel testing verified the possibility of obtaining high aerodynamic efficiency of telescope wings and revealed some special features in the flow pattern in the joint area.

5. The rational type of the telescope wing joint was determined as a result of weight analysis. The research of telescope wings have shown that they can have nearly the same weight efficiency and aerodynamic performance as equivalent trapezoidal wings of the same span and area.

6. Preliminary results of telescope wing optimisation have shown that high weight efficiency and aerodynamic performance are obtained with small relative (referency) chord of the movable part of the wing, about 0.25. Such variant of the

telescope wing can be considered as perspective for liner aircraft and other applications.

7. Comparison of the results of weight estimations for telescope wings, obtained with two different approaches – with uniform load distribution and with spanwise load distribution calculated with discrete vortex method – has shown that the first approach can be used for comparing weight efficiency of different designs. But for weight design the second approach should be used, because the difference can make up to 10-15%.

8. Calculations of full mass coefficient for maneuvarable aircraft wing with large area of movable parts, and for flap and slat of liner aircraft resulted in a wide spreading of values, which points to the necessity of additional research of this coefficient, concerning mainly the account for multiple load cases.

9. Comparison of numerical simulations of flow past the model telescope wing with the experimental results from pressure orifices model have shown a good agreement. Thus a mutual verification of computational and experimental methodology was performed. The technology used for creation of pressure orifices model and pressure distribution measurement with Honeywell^{TM} Sursence$^{®}$ DUXL10D pressure sensors with automated data processing has proved to be highly reliable and accurate and can be used further for quick research of the same problems.

10. The present research have required coordinative work of the specialists in different fields – computational modelling and optimization of the structures, computational and experimental aerodynamics. For the purpose of this research necessary licensed software and experimental equipment was purchased, and some additional software was developed. The important result of this project is the creation of the team which is capable for solving wide range of problems dealing with morphing wings and similar research.

11 Future work recommended

1. Development of the proposed method for weight analysis in order to account for multiple load cases.

2. Further multi-disciplinary research of morphing wing for the purposes of optimization of their parameters and search of their efficient applications.

12 Plan of publishing

Preparation of the following papers is proposed:
1. Application of 3D modelling to weight estimations of aircraft structures.
2. Features of telescope wing aerodynamics.
3. Estimation of weight and aerodynamic performance of telescope wings.

13 References

1.   Badyagin A. A. et al. Airplane design (in Russian), 1972. 516 p.

2.   Belotserkovskii S. M. Study of the unsteady aerodynamics of lifting surfaces using the computer //Annu. Rev. Fluid Mech., vol. 9, Palo Alto, Calif., 1977. pp. 469-494.

3.   Bolohvitinov V. F. Ways of aircraft evolution (in Russian), 1962. 130 p.

4.   Eger S. M. et al. Airplane design (in Russian), 1983. 616 p.

5.   Fomin N. A. Airplane design (in Russian), 1961.

6.   Frolov V. A. Lift distribution for wing-body configurations in subsonic flows //Proceedings of XXVI Seminar at the development of scientific legacy and ideas of K. E. Tziolkovsky (Kaluga, 17th-20th of September, 1991). Section «Aviation and aeronautics», Problems of aviation and aeronautics. – Moscow: Russian Academy of Sciences, 1992. – pp.26-31. (in Russian).

7. Gevers D. Multi-purpose aircraft. US Patent ## 5,645,250; 5,850,990; 6,098,927; http://www.geversaircraft.com

8.   Kalinin A. I. Integral and distributed aerodynamic properties of clear wing at low subsonic speeds // Proceeding of TsAGI, vol. 1503, Ì .: TsAGI, 1973. 354 p. (in Russian).

9.   Kefely A. I. On theoretical weights of constructions (in Russian). Proceedings of Leningrad Institute of Railway Transport, 1927. Vol. 96. pp. 247-266.

10. Komarov A. A. Fundamentals of load-carrying structures design, Samara,1965. 82 p. (in Russian).

11. Komarov V. A. On efficient distribution of material in a structure. - News of AS USSR. Mechanics. 1965, #5, p. 85-87. (in Russian).

12. Komarov V.A. The Weight Analysis of Aircraft Structure: Theoretical Base. - "Poliot", 2000, #1, pp.31-39. (in Russian).

13. Komarov V.A., Design of Airframe Structures. – In book: Actual Problems of Aviation Science and Technic. M.: Mashinostroenie, 1984. pp. 114-129.

14. Komarov V.A., Rational Design of Airframe Structures //PhD Thesis, Samara (Kuibyshev), 1975. 328 p. (in Russian).

15. Komarov V.A., Weisshaar T.A. New Approach to Improving the Aircraft Structural Design Process. AIAA, Journal of Aircraft, March – April 2002, Volume 39, Number 2, pp. 227-233.

16. Kozlov D. M. et al. Airframe structure modelling for weight analysis on early stages of design. TVF Journal. Ì . 1999. #4-5. pp.31-37. (in Russian).

17. Raymer D.P. Aircraft Design: A Conceptual Approach. AIAA Education Series. 1992. 745p.

18. Shainin V. M., Kozlovskiy V. I. Weight design and efficiency of passenger airplanes, 1984. 552p. (in Russian).

19. Shanly F. R. Weight-Strength Analysis of Aircraft Structures, 1952.

20. Torenbeek E. Subsonic airplane design, 1983. 648 p.

21. Weisshaar T.A. Aero-morphing Aircraft Concepts. Contract F33615-98-D3210. Purdue University. West Lafayette, Indiana 47907-1282. 31 January 2002

22. Weisshaar T.A. Aeroelastic tailoring for energy efficient morphing aircraft – finding the right stuff. ICASE. NASA/ LaRC. 25 October 2001

23. Wåisshaar T. A., Komarov V. A. Human factor in design of aircraft structures. - "Poliot", 1998, ¹ 1, p.17-23. (in Russian).